MAPPING THE OCEAN SOUND SPEED AT THE ALOHA CABLED OBSERVATORY USING RELIABLE ACOUSTIC PATH TOMOGRAPHY

A THESIS SUBMITTED TO THE GRADUATE DIVISION OF THE UNIVERSITY OF HAWAI‘I AT MANOA IN PARTIAL FULFILLMENT OF THE REQUIREMENTS FOR THE DEGREE OF

MASTER OF SCIENCE
IN
OCEAN AND RESOURCES ENGINEERING

May 2019

By
Sitthichat Sukpholtham

Thesis committee:
Bruce Howe: Chairperson
Eva Nosal
John Allen

Acknowledgements

Vincent Varamo laid much of the foundation and ground work for this work in his master's thesis (2015-2017) and has continued to contribute to the data analysis. Grant Blackinton provided expert advice on the acoustics and participated in all the cruises. Matt Dzieciuch, Scripps Institution of Oceanography, kindly made code available (Scarlett and ray tracing), as well as advice. James Foster provided guidance on the use of the global navigation satellite system and provided related data. Jim Jolly and Dave Harris assisted in setting up the electronics. The assistance of many students who participated on the cruises is appreciated, including Martin Barbier, James DeMolina, Bradley Beeksma, Shijie Huang, Kei Manabe, Cameron Morrow, Nicholas Ulm, Jessica Lotts, and Terry Moreau. The Ocean Technology Group including Sonia Brugger, Jeff Koch, Justin Smith, Justin Smith, Elizabeth Ricci, and Trevor Young; Scott Ferguson leading OTG, provided much needed support for operating the ships positioning system. The captains and crew of the R/V Kilo Moana provided excellent support on all the cruises.

The ALOHA Cabled Observatory (ACO) with its infrastructure, data management, and hydrophones, made the project possible. Having precisely timestamped data available in real time was invaluable for real time analysis to guide the ship-base transmissions. Jim Potemra, Fernando Santiago-Mandujano, Kellen Rosburg, Blue Eisen, Jim Jolly, Brian Chee, Kellie Terada, and Karynne Morgan all provided assistance. The ACO observatory is supported by grants from the National Science Foundation, Ocean Technology and Interdisciplinary Coordination, NSF OCE- OCE-1738054 and OCE-1539244.

Committee members, Bruce Howe, Eva Nosal, and John Allen all helped along the way and made suggestions on how to improve the work and thesis. I would like to thank Dr. Howe for all the advice throughout the years and the opportunity to work on this project.

The support of the Office of Naval Research (ONR) is gratefully acknowledged, through grant N00014-15-1-2091, Acoustics at Station ALOHA: RAP Tomography.

Abstract

We have investigated the feasibility of Reliable Acoustic Path (RAP) tomography using a mobile ship platform (*R/V Kilo Moana*) and the existing acoustic infrastructure at the ALOHA Cabled Observatory (ACO). Travel times of acoustic signals traveling along direct paths between the shipboard acoustic source and the bottom-mounted hydrophones were measured. Perturbations of the travel times relative to predicted travel times were obtained, based on the CTD cast closest in time to the experiment date. Stochastic linear inversion was employed to solve for sound speed perturbation fields using the travel time perturbation measurements. This provides a spatially-dependent sound speed field (a proxy of temperature) over a 60-km-diameter "teacup" volume of the ocean. This project is a continuation of previous RAP work which laid the foundation for the work described herein. The preliminary results from three RAP cruises since June 2017 showed non-physical range-dependence and ship-dependence of the travel time perturbations. Improvements to the ray tracing and corrections to data processing were made to solve these issues. This resulted in a reasonable range of travel time perturbation variability which yielded realistic sound speed spatial variability from the inversion process. The sensitivity of the travel time perturbation to the third empirical mode of the vertical sound speed perturbation structure was found to be higher than expected. The vertically-averaged sound speed was used to represent the model parameters as it had the overall highest resolution and corresponding low estimated error. These results demonstrate the practicality and utility of the RAP tomography at the ACO and general applicability for other observatories and seafloor geodesy.

Table of Contents

Page

List of Tables

List of Figures

1. Introduction

Ocean acoustic tomography is one among many ocean observing techniques which allows scientists to study ocean properties on large spatial scales. Proposed by Munk and Wunsch in 1979 (Munk & Wunsch, 1979), this technique has been proven for its practicality in a number of experiments over more than four decades. It is predicated on the nature of sound propagation in the ocean and the sensitivity of the propagation to changes in the ocean sound speed field (closely related to temperature). The most tempting advantage of ocean acoustic tomography is that it produces spatial averages over large distances which cannot be achieved by conventional, in situ point measurement. In the long run, ocean acoustic tomography is envisioned to be autonomously operated on a regular basis with near-zero human supervision and be practiced worldwide using cabled sources, and fixed and mobile receivers. This technique will increase the amount of data, in a N^2 fashion, where N is the number of instruments, which will be assimilated with other data to help improve numerical modeling of the ocean circulations (Munk, Worcester & Wunsch, 1982).

The Reliable Acoustic Path (RAP) Tomography project leverages the existing infrastructure of the deep ocean observatory ALOHA Cabled Observatory (ACO). The ACO is located about 100 km north of Oahu, Hawaii at Station ALOHA (22 45'N, 158 W) at a depth of 4728 m. It is one of a few deep ocean observatory systems in the world that uses a retired transoceanic cable system to provide power and communications to a node of sensors on the seafloor; It is the deepest such node on the planet. The ACO's mission is to measure ocean parameters to allow scientific research to be done on a continuous basis, enabling real-time un-aliased data collection with precise timing. At the ACO, there are basic oceanographic instruments such as ADCP, CTD, pressure sensor, camera, etc., plugged into the node and streaming data back to the shore via the communication cable. Included in this setup are two hydrophones, one is installed in the Hydrophone Experimental Module (HEM) which samples at a rate of 96 kHz and another hydrophone *icListen HF* from Ocean Sonics, Inc. which samples at a rate of 32 kHz (**Chapter 5**). The initial deployment of the observatory was in June 2011, with several subsequent deployment and maintenance cruises which retrieve failed instruments and deploy new sensor packages. The icListen hydrophone has been in operation since its installation in June 2018.

The UH research vessel R/V *Kilo Moana* (*KM*) is the main vessel that has been used by many groups of scientists at UH. It is also the vessel which is used by the HOT (Hawaii Ocean Timeseries) project which has been running since continuously since 1988. HOT researchers use the *KM* to study the physical, chemical, and biological oceanography components of the central subtropical gyre of the North Pacific by making consistent quasi-monthly ocean measurements at the HOT site. **Figure 1** shows the center point of Station ALOHA (22º 45' N 158º W), which includes a 10-km radius circle where HOT activities are centered within it. This location is the same as that the ACO is located. On the vessel, there is a 4x4 sub-bottom echosounder transducer array located in a coffer dam on the bottom of the starboard hull of the ship. The transducers in the array are manufactured by Massa, model TR-1075A, with a peak response at a frequency of 4 kHz. A single transducer can be driven by a maximum input power of 600 W at 30 percent duty cycle or 200 W of power at 100 percent duty cycle (**Appendix F**). For the current setup, only one transducer is being used (transducer number 5 in **Figure 2),** transmitting a 22.5-ms linear-frequency-modulated (LFM) sweep signal every 30 s at 367 W (199.5 dB re 1 µPa @ 1 m).

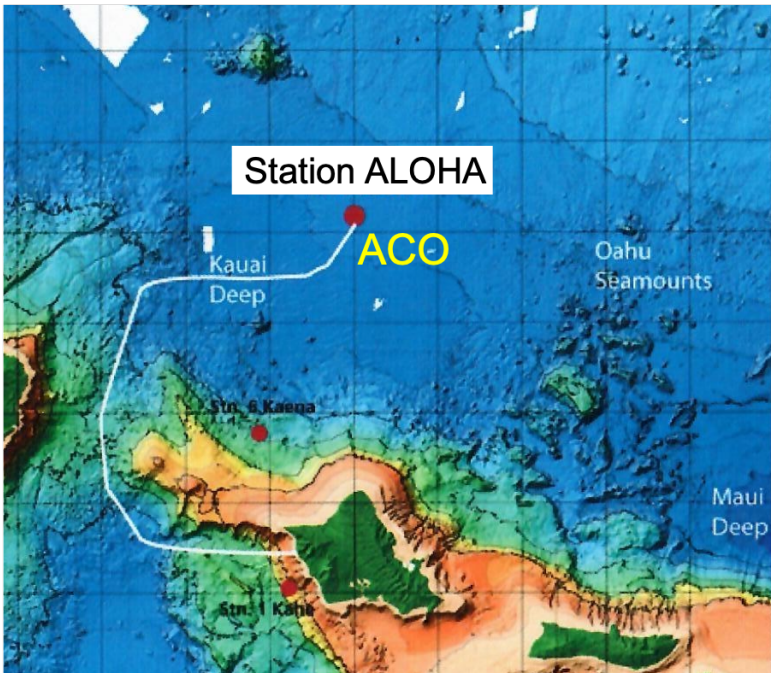

Figure 1. Map of an area showing Station ALOHA 100 km north of Oahu. ACO is at the same location as is the quasi-monthly HOT sampling.

Figure 2. Housing and the interior view of the 4x4 (135 by 135 cm) transducer array located on the hull of the R/V Kilo Moana. The numbering is given by the ship survey report. The cable bundle (red box) is used as a reference for transducers in the bath.

With the onboard transducers, the bottom-mounted hydrophones, and other associated infrastructures on the vessel and at the ACO, transmission and reception of acoustic signals are actualized. This allows us to perform reliable acoustic path tomography. The goals of this experiment were to send coded acoustic signals when the vessel is traversing around the ACO up to a certain range, measure precise travel times of those signals, and infer sound speed perturbation fields of the ocean from the travel time perturbation measurements. The setup of this experiment can be viewed as an extension of an inverted echosounder combined with the precise positioning and timing of seafloor geodesy (Burgmann & Chadwell, 2014). An inverted echosounder is a bottom mounted instrument which pings an acoustic signal and records the returning surface reflected signal to determine the round-trip acoustic travel time. In this case, the same vertical ray path, but only one way, and extend this out to a near horizontal ray path when reaching the maximum allowable range (vertical: horizontal = 1:5). The maximum theoretical range was determined by the sound speed profile of the ocean surrounding the ACO using Ray Theory. The largest launch angle with respect to the vertical from the transducer that allows a direct path was used to establish the desired radius of about 30 km. The volume of the ocean which was probed by the acoustic signals is similar to a “teacup” shape as shown in

Figure 3. The absolute travel times were then compared with those estimated from a reference state of the ocean to calculate travel time perturbations. By applying stochastic linear inversion to the travel time perturbation measurements, an averaged ocean sound speed perturbation field was obtained. This enables the monitoring of changes in ocean temperature within the volume acoustically.

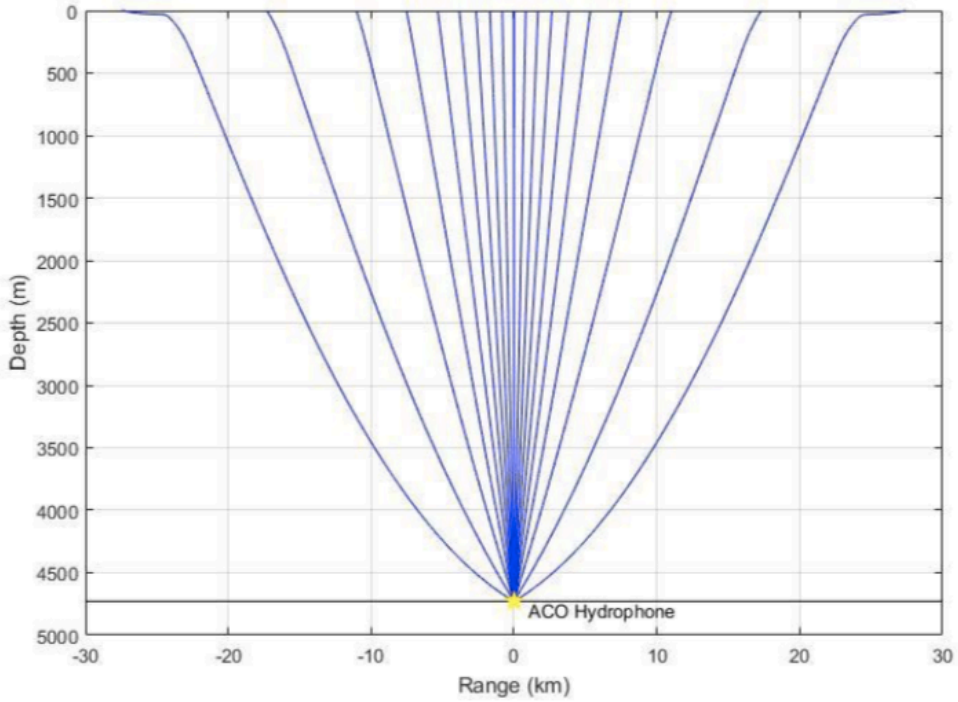

Figure 3. A RAP "teacup" volume. The volume is enclosed by reliable acoustic ray paths (no interaction with interfaces) for all different ranges extending to ~ 30 km away from the ACO. Each pathway is an eigen ray corresponding to a different surface distance. The ray paths were calculated based on August 2015 HOT CTD cast data (22º 45' N, 158º W, Station ALOHA).

The major objectives we set to accomplish in this project were to resolve problems regarding the acoustic travel time measurements realized by the existing ocean acoustic tomography system, estimate new positions of the bottom-mounted hydrophones, and create a sound speed perturbation field of the ocean surrounding the ACO. Resolving the ocean acoustic tomography system problems will allow us to obtain reliable measurements of acoustic travel times which is the foundation of ocean tomography work. Estimating new hydrophone positions provides other hydrophone users a better representation of their positions on the seafloor for future applications that require precise acoustic travel times. Finally, mapping the ocean sound speed perturbation

field allows for indirect measurement of the changes in seawater temperature. Provided that the tomographic measurements are taken on a regular basis, ocean events can be seen and traced through time. Upon completion of this project, we can take opportunities when the vessel travels to station ALOHA monthly to perform HOT tasks, to make tomographic measurements and process the data from the ACO hydrophones. By this means, we will obtain average ocean temperature information which will complement the conventional temperature measurement by CTD casts. Furthermore, this project will be a case study of using mobile platforms and seafloor-mounted hydrophones at ocean observatories to perform RAP tomography for other ocean observatories distributed around the world and more to come in the future.

This project is a continuation of the previous RAP work which was documented in Vincent Varamo's Master's thesis (Varamo, 2017). The previous work laid the groundwork for the RAP tomography experiment setup which was used in three subsequent RAP cruises since June 2017. The first cruise took place 6-12 June 2017; the second cruise took place from 18-23 June 2018; and the latest cruise took place from 26-31 October 2018.

Chapter 2 provides background information about ocean acoustic tomography and discusses details of the experiment configuration. **Chapter 3** describes the established RAP project ocean tomographic system including the acoustic transmission system, shipboard GNSS positioning systems, ACO hydrophones, and the experimental setup. **Chapter 4** presents the preliminary results from the cruises prior to the October 2018 cruise and identifies issues which are addressed in the subsequent chapters. **Chapter 5** describes the characteristics of the HEM and icListen hydrophones, and a method to handle hydrophone timing issues**. Chapter 6** presents the results of GNSS positioning system analysis to ensure the reliability of the acoustic transmission locations. **Chapter 7** looks at the travel time measurements from the October 2018 cruise. An analysis of travel time perturbations was conducted to investigate for the root causes of the identified issues. The improvements to the ray tracing method and data processing are presented. **Chapter 8** introduces the linear inversion theory for the sound speed perturbation. The performance of the computational model is discussed for different simulated scenarios. **Chapter 9** continues, using the inversion procedure with the actual travel time perturbation data to obtain maps of sound speed perturbation with interpretation. Concluding remarks are provided in **Chapter 9**. The flow follows roughly a chronological approach to the problems that arose and the solutions thereof.

2. Background

Acoustic propagation in the ocean can be explained by ray theory introduced by Isaac Newton in the seventeenth centaury. The acoustic energy radiates from a source along certain trajectories called rays. From and omnidirectional source, rays propagate in all possible directions along ray paths until they reach a receiver. The ray paths which connect the source and the receiver are called eigen ray paths. The eigen ray paths can be a direct path connecting the source and the receiver, or indirect paths in which the rays bounce at medium interfaces (i.e., sea surface and ocean bottom) before reaching the receiver. Energy loss is inevitable while a sound wave propagates across space and interacts with interfaces. Acoustic signals traveling along different ray paths experience different levels of attenuation, phases shift, and time delay. Reliable acoustic path (RAP) is a mode of acoustic transmissions in which a ray propagates along the direct path. Thus, the ray will spend least time to reach the receiver with minimum energy loss, resulting in the earliest and the strongest acoustic reception at the receiver. This will yield the most accurate travel time measurement among all possible paths. The equations of "motion" for a ray propagating through an ocean can be written in Cartesian coordinates as (Dushaw and Colosi 1998)

$$\frac{d\theta}{dr} = \frac{1}{c}\frac{\partial c}{\partial r}\tan(\theta) - \frac{1}{c}\frac{\partial c}{\partial z} \quad \textbf{(1)}$$

$$\frac{dz}{dr} = \tan(\theta) \quad \textbf{(2)}$$

$$\frac{dt}{dr} = \frac{\sec(\theta)}{c} \quad \textbf{(3)}$$

where θ is the angle of the ray with respect to the horizontal, z is the vertical distance from sea level (positive upward), r is the horizontal distance, c is sound speed, and t is travel time along the ray. In a range-independent case (sound speed is a function of depth only), **Equation 1** can be re-written in a simplified form

$$\frac{\cos(\theta)}{c(z)} = \frac{\cos(\theta_1)}{c(z_1)} = \text{constant} = a \quad \textbf{(4)}$$

where θ_1 is the ray launch angle at the source and c_1 is the sound speed at the source depth z_1. The ratio of cosine of the ray angle to the corresponding sound speed is a constant called the "ray parameter" denoted by a. This is the familiar Snell's law used extensively in optics (Medwin, 2005).

Sound speed in the ocean is known to be a function of temperature, salinity and depth (pressure). A simplified formula to demonstrate the relationships of these variables and sound speed is given by Medwin (2005)

$$c = 1449.2 + 4.6T + 0.055T^2 + 0.00029T^3 + (1.34 - 0.01T)(S - 35) + 0.016z \qquad \textbf{(5)}$$

This formula is accurate to 0.1 m/s and applicable to only 1000-m depth where the sound speed is mainly dependent on temperature. It gives a general idea of the sensitivity of the sound speed to ocean variables. A more accurate sound speed equation is the Thermodynamic Equation Of State-2010 (TEOS-10) for seawater (McDougall and Barker, 2011) which was used in this study. With the knowledge of the ray geometry and sound speed, the acoustic travel time along a ray path can be determined by **Equation 6**

$$t_i^{\pm} = \int_{\Gamma_i^{\pm}} \frac{ds}{\left(c(\underline{x}, t) \pm u(\underline{x}, t)\right)} \qquad \textbf{(6)}$$

for transmissions in the positive (+) and negative (-) horizontal directions; Γ_i is the i^{th} ray path, ds is differential arc length along the ray, and u is current velocity along the ray. The travel time is integrated along the trajectory of the i^{th} ray. To simplify the problem, the sound speed c can be viewed as a summation of a reference value c_o and a perturbation field c' in which $c' << c_o$ (normally, $c_o \cong 1500$ m/s; $c' \cong 15$ m/s),

$$c(\underline{x}, t) = c_o(\underline{x}, t) + c'(\underline{x}, t) \qquad \textbf{(7)}$$

Here, travel time perturbations relative to a reference ocean state are of more interest. By substituting **Equation 7** into **Equation 6**, and linearizing, the travel time perturbation t' can be written as

$$t_i(c)^{\pm} - t_i{}^{\pm}(c_o) = t_i{}'^{\pm} = \int_{\Gamma_i{}^{\pm}} \frac{ds}{(c_o(\underline{x},t) + c'(\underline{x},t) \pm u(\underline{x},t))} - \int_{\Gamma_i{}^{\pm}} \frac{ds}{(c_o(\underline{x},t) \pm u(\underline{x},t))} \quad \textbf{(8a)}$$

$$t_i{}'^{+} = -\int_{\Gamma_i{}^{+}} \frac{c'(\underline{x},t) + u(\underline{x},t)}{{c_o}^2(\underline{x},t)}\, ds \quad \textbf{(8b)}$$

$$t_i{}'^{-} = -\int_{\Gamma_i{}^{-}} \frac{c'(\underline{x},t) - u(\underline{x},t)}{{c_o}^2(\underline{x},t)}\, ds \quad \textbf{(8c)}$$

The sum and difference of reciprocal travel time perturbations are given by

$$s_i = \frac{1}{2}(t_i{}'^{+} + t_i{}'^{-}) = \int_{\Gamma_i} ds \frac{c'(\underline{x},t)}{{c_o}^2(\underline{x},t)} \quad \textbf{(9)}$$

$$d_i = \frac{1}{2}(t_i{}'^{+} - t_i{}'^{-}) = -\int_{\Gamma_i} ds \frac{u(\underline{x},t)}{{c_o}^2(\underline{x},t)} \quad \textbf{(10)}$$

The sum and difference can be used to calculate *c'* and *u*. However, they require reciprocal transmissions between the two transceivers. In general, sound speed perturbations c' (m/s) are at least an order of magnitude greater than the ocean current speeds *u* (cm/s) (Worcester, Cornuelle and Spindel, 1991). Thus, ignoring water velocity here, the travel time perturbation for one-way transmission, **Equation 9** becomes

$$t'_i = -\int_{\Gamma_i} \frac{c'(\underline{x},t)}{{c_o}^2(\underline{x},t)}\, ds \quad \textbf{(11)}$$

Then, we can obtain the sound speed perturbation from one-way transmissions (Medwin and Spindle, 2005). This expression is "linearized" about the reference sound speed (between equations 8a and 8b,c). Ocean acoustic tomography is based on measuring the travel time of acoustic transmissions in the actual ocean state and comparing that to a known travel time in a reference ocean state to infer the difference, the ocean variability. With the travel time

perturbation measurement, inverse theory is applied to solve for the sound speed perturbation field, and in turn the oceanographic properties (here, the temperature is the most important factor as the salinity effect is relatively small).

A key advantage of tomographic measurements is that they are spatially integrating along ray paths. They have a potential of forming horizontal and vertical averages over large ranges, typically on a scale of hundreds of kilometers. The path integrals inherently suppress small-scale features such as internal waves which contaminate conventional point measurements. Moreover, tomographic techniques allow for repeated and rapid measurements to observe the ocean (at the speed of sound) (Munk, Worcester, and Wunsch, 1995). A number of experiments have demonstrated the feasibility of long-term constant tomographic measurements on scales up to an ocean basin (e.g., Dushaw et al., 2009).

A bound on the expected travel time signals for the RAP geometry at ALOHA can be obtained from inverted echosounder measurements presented by Chiswell (1994). The experiment had five inverted echosounders deployed in an array centered at the Station ALOHA to measure round-trip acoustic travel time changes over several years. Four inverted echosounders in the array were located 50 km away from the center unit which was at the Station ALOHA . A peak-to-peak round-trip travel time was measured to be 5 ms, or approximately 1.8 ms rms one-way. According to this finding, the expected depth-averaged sound speed perturbation is 1 m/s, or a (very approximate) 5 m/s change in the main thermocline. In addition, the finding also found phase shifts among the travel time signals of these distributed inverted echosounders suggesting eddy propagation (Chiswell, 1994). In this study, to detect these small temporal and spatial changes, we need to achieve travel time accuracy of a tenth of millisecond.

3. Ocean Acoustic Tomography System

In this chapter, we discuss the ocean acoustic tomographic system implemented in this project which consists of an acoustic transmission system, ship positioning systems, and the bottom-mounted hydrophone receiving systems. The acoustic transmission and receiving systems have been established and proved to have sufficient accuracy for our purpose (Varamo, 2017). **Figure 4** shows the schematic diagram of the ship-based experiment setup.

Acoustic Transmission System

An audio interface device, Focusrite Scarlett 6i6 (**Appendix F**), served as a central module and samples at 44.1 kHz. One input channel of the Scarlett was connected to a 1 PPS (pulse per second) source for timing purposes (provided by the ship GNSS positioning system). An onboard computer was connected to the Scarlett via a USB port. This computer was used to generate the digital transmission signals sent to the Scarlett. The digital signal was converted to analog and sent from the Scarlett to a power amplifier (Proel HPX2800, **Appendix H**). The signal was then amplified to the desired level (199.5 dB) and relayed to the transmission transducer through a cable. Just after the power amplifier and in-line, a voltage/current measurement box was inserted to directly measure the voltage and current of the amplified signal. This was to verify the power level and the shape of the signal after passing through the amplifier, and to measure the exact time when the signal was being sent to the transducer; both voltage and current readings were recorded by the Scarlett. Once the signal reached the transducer, the transmission transducer converted electrical energy into acoustic energy and transmitted it into the ocean. An adjacent reference transducer was used as a receiver to pick up the transmitted signal and sent it back to the Scarlett. This was to verify if the waveform matched the generated one and to measure the transmission time delay from when the signal left the voltage/current measurement box until it was transmitted out to the ocean (electronics and cable delay, for example). All of the inputs of the Scarlett were available for real-time monitoring with an oscilloscope.

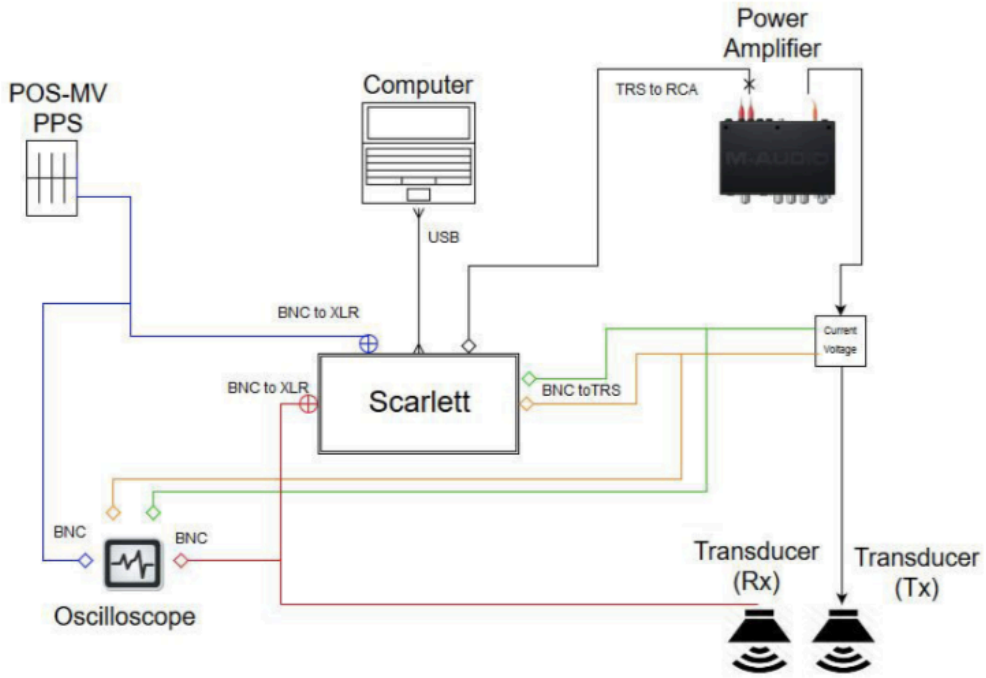

Figure 4. Schematic diagram of the acoustic transmission system.

The computer communicated with the Scarlett through Matlab and C codes and recorded the four Scarlett channels (reference transducer, PPS, voltage, current). A Matlab script scheduled a transmission every 30 seconds to leave some time for a set of sound waves travelling along different paths to reach at the receiver end. This helped prevent interference among multi-path arrivals in the audio recorded by the hydrophones. The Scarlett received the voltage and current signals from the V/I measurement box and also the feedback signal from the reference transducer corresponding to each transmission. To avoid overloading the computer's memory and to keep the Scarlett output file size manageable, the transmission was divided into 15-minute cycles. At the end of each transmission cycle, the computer produced an output file containing voltage, current, PPS, and reference transducer signals. In between transmission cycles, the computer required 2-3 minutes to finish writing the output file, leaving a 2-3-minute gap without transmissions every 15 minutes.

Some modifications to the acoustic transmission system were made on the October 2018 cruise. Firstly, the first transmission of each cycle was timed to be made at integer minutes. Thus, the transmissions were started on the minute at 0 s or 30 s after, according to the computer's clock. Secondly, per ONR guidance, the acoustic power was raised to 199.5 dB to increase SNR (Signal-to-Noise Ratio) of the acoustic receptions. Lastly, the reference transducer was

disconnected because the transmission system delay was already determined to be 0.304 ms and the transmitted signal was already verified (Varamo, 2017).

All events and measurements were logged with respect to UTC (Coordinated Universal Time). As the transmission computer's clock is always drifting, each transmission which was timed to occur at a computer's integer second did not necessarily correspond to a UTC integer second. To obtain exact times of transmissions in UTC, the 1 PPS signal provide by the ship's GNSS system (POS MV) was used as the reference of integer seconds with respect to UTC. By finding a time offset between a nearest rising edge of a pulse and the voltage signal of the transmitted signal (from the power amplifier output voltage), the exact transmission time with respect to UTC could be obtained by adding that time offset to the timestamp given by the computer (**Figure 5**). To avoid ambiguity of determining which second a transmission belonged to, the time offset between the computer time and UTC must not exceed 0.5 second. This was achieved by setting the computer to synchronize its clock with an NTP (Network Time Protocol) server at the end of each transmission cycle.

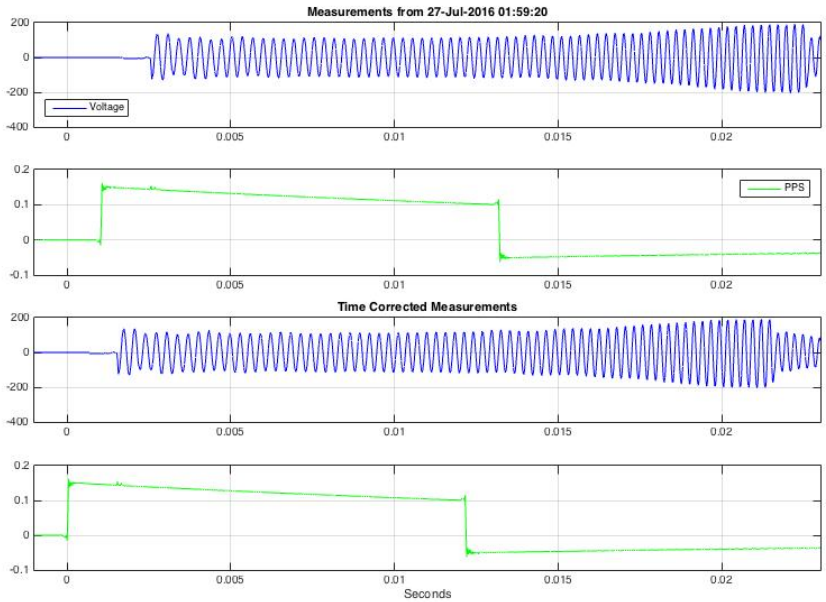

Figure 5. Transmission time determination. The upper two figures show the original transmitted waveform and a rectangular pulse of the PPS. In this particular case, the two signals are shifted by the time offset of 0.0015 sec to align the rising edge of the pulse with the nearest integer second.

On the last three cruises, the signal used in the experiments was a linear frequency modulated (LFM) signal with 4,134.375 Hz center frequency, 1,378.125 Hz bandwidth, and 22.5 ms duration (**Appendix A**). This signal duration was selected to minimize Doppler shift effects and to maximize signal processing gain (PG) obtained from *pulse compression*. With these parameters, sufficient timing accuracy for the propose of this study could be achieved. For the detailed acoustic calculation, see **Appendix B.**

Hydrophone System

On the reception end, two hydrophones, HEM and icListen, at the ACO received the acoustic signals. Thanks to the infrastructure at the ACO, audio files of the two hydrophones are stored in a server machine and accessible via the Internet. The timing precision of hydrophones' files are at the sub-microsecond level, which was sufficient for our purpose. The initial estimated positions of the two hydrophones were given by ROV survey during ACO service cruises. There are differences and discrepancies in the physical and electrical characteristics of the two hydrophones. Moreover, some caveats regarding hydrophones' timing were discovered which needed to be handled (integer second timing offsets). A detailed discussion of the hydrophones and associated acoustic data is provided in **Chapter 5**.

GNSS Positioning System

Critical supporting information needed for tomography is the acoustic source position at the exact time of transmission. On the R/V *Kilo Moana*, a shipboard Position and Orientation System for Marine Vessels (POS MV) operates to provide the vessel's position and attitude in real-time. The POS MV uses GNSS data received by two GNSS antennas and two GNSS receivers, and information from an inertial measurement unit (IMU) to calculate ship position, heading, and attitudes. It can be configured to report positions and orientations of any arbitrary point on the vessel at a specific time interval. The reporting rate of the POS MV was initially set to 1 Hz, which was increased to 10 Hz for the October 2018 cruise. In this project, the transducer positions at the time of transmissions were obtained from the POS-MV binary output. The ship position data is addressed in **Chapter 4**.

4. Preliminary Results

In January 2017, R/V *Kilo Moana* embarked on a 4-day HOT cruise to Station ALOHA. Even though the ship paths followed during the cruise were not ideal for tomography purposes, this was the first opportunity for an at-sea test to prove the practicality of the tomography system, signal processing methods, and also inversion procedures. On this cruise, the nominal sound level was 195 dB and several types of signals - continuous wave (CW), linear-frequency modulated (LFM), and M-sequence (pseudorandom binary sequence) - were tested. **Figure 6** shows locations where acoustic transmissions were made.

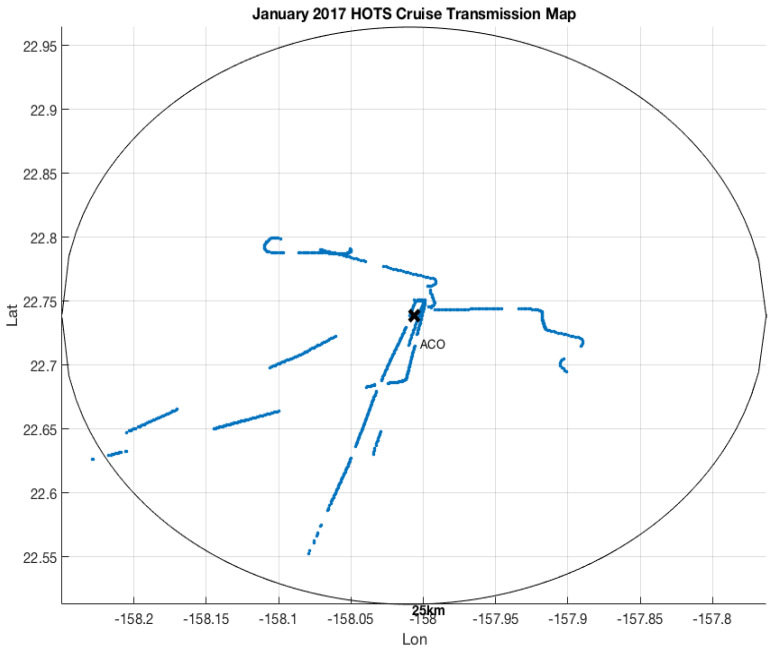

Figure 6. The transmission map for the January 2017 cruise. The blue dots represent the transmission locations and the circle defines the 25-km range from the ACO.

The result from this cruise revealed irregularities of the travel time perturbation patterns. The patterns suggested that the travel time perturbations not only depended on the surface range from the HEM hydrophone, but also had larger magnitudes than expected. Besides, the travel time perturbations also varied with vessel movement. The transducer position data from the POS MV also had some bad sections in which the altitude data errors deviated from a sensible range and needed to be removed from the analysis. Using this preliminary travel time perturbation data, a

stochastic linear inversion produced sound speed perturbations which were non-physically large. Besides, based on the obtained inverse solution, the reconstructed travel time perturbations measurements were greatly different from the actual measurements, which means that this inverse solution was inconsistent (Varamo, 2017).

On the subsequent cruises in June 2017, June 2018, and October 2018, the ship paths were designed to provide us with sufficient data to resolve issues regarding unusual travel time perturbation patterns and to solve for the sound speed perturbation field around the ACO, as well as hydrophone position offsets. The basic idea of the ship paths was to sample the ocean volume as well as possible and extend the coverage to the maximum RAP range of around 25 km. The paths included circles of several radii (25 km,15 km, 10 km, 5 km) and various geometries, - including radial lines, squares, grid search, and spins – that were taken to give additional information for investigating what factors caused the unusual travel time perturbation patterns. **Figure 7** shows summarizes the ship paths.

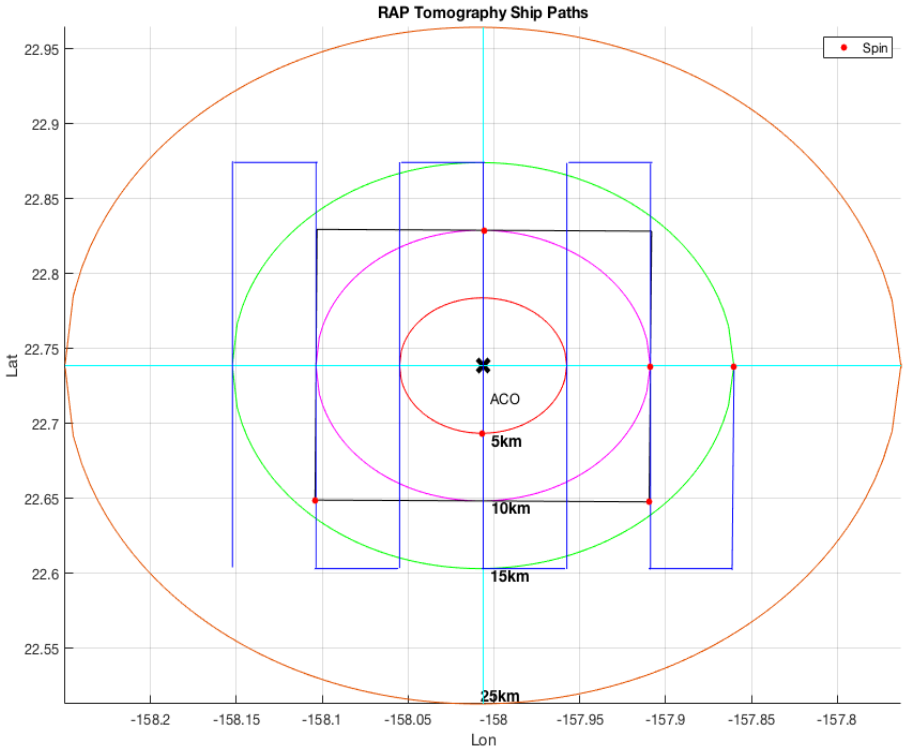

Figure 7. Ship paths taken in the RAP tomography project (red dots are locations of spins).

The results from June 2017 and June 2018 cruises brought up an issue regrading apparent ship-heading dependence of the acoustic travel time. **Figure 8** shows an example of a westward radial

path on the June 2018 cruise. The ship began the course at the eastern end of the east-west transect. When the ship turned 180 degrees to align its heading to the west, the travel time perturbation dropped by 10 ms within a short period of time. The travel time perturbation slightly varied while the ship was moving towards the ACO from the east and started to increase when the ship crossed the ACO from the eastern side to the western side. From this observation, every time the ship was heading "outward" from the ACO, the travel time perturbation grew larger with range. The opposite applied when the ship was heading "toward" the ACO. In addition, the travel time perturbation changed abruptly when the ship turned which also raised a question about the ship angular acceleration effect on the ship position data.

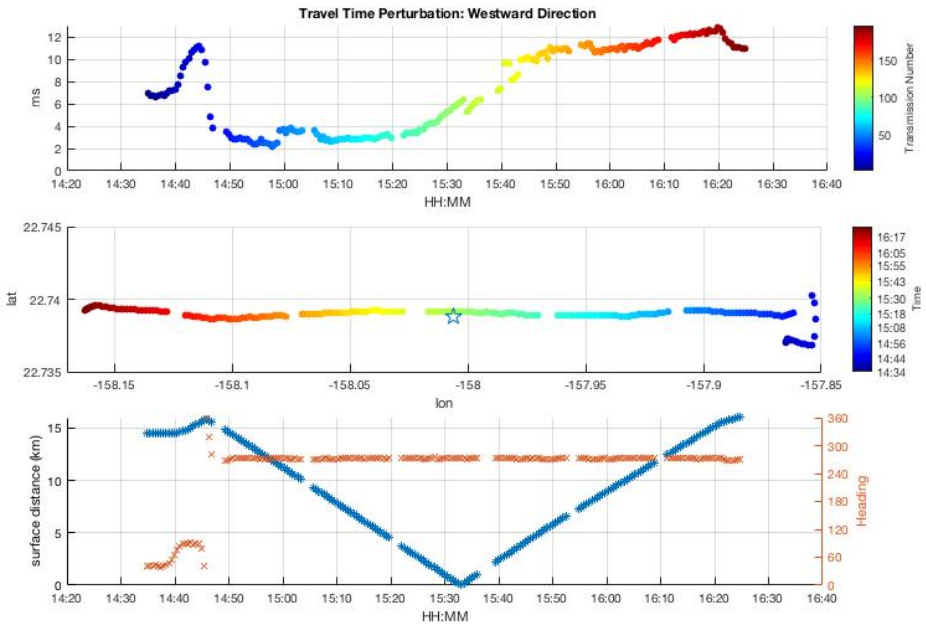

Figure 8. Travel time perturbations of a westward radial transect on the June 2018 cruise. The upper plot shows travel time perturbations versus time. The middle plot shows coordinates of transmissions with the start marker representing the ACO. The color scale represents time of transmissions. The lower plot shows surface distance of the vessel from the ACO and the ship heading versus time.

Another finding revealed that the travel time perturbation also increased with range. **Figure 9** shows a summary plot of the travel time perturbations from the June 2017 cruise.

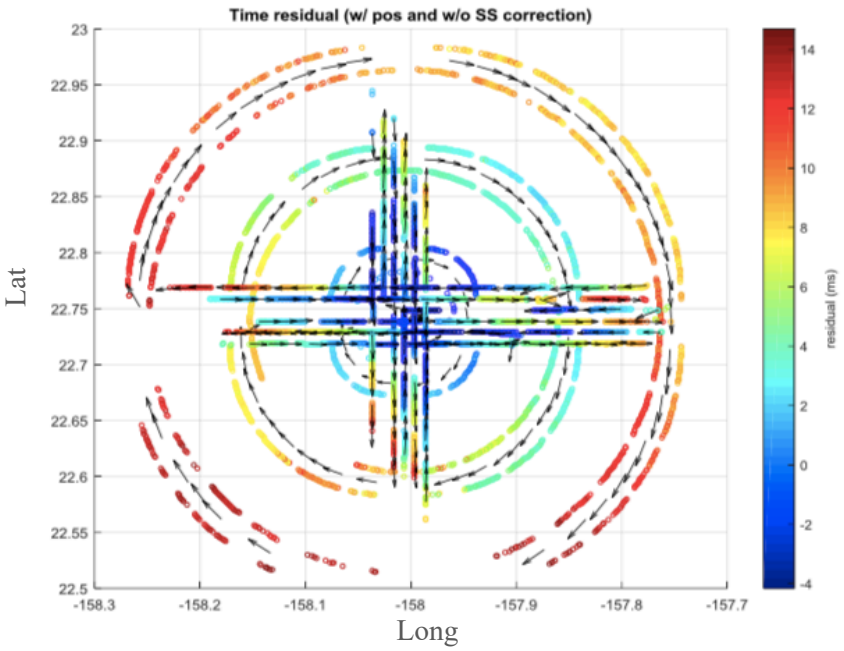

Figure 9. A summary plot of the travel time perturbations of the June 2017 cruise. The color represents travel time perturbation magnitudes. The arrows indicate the heading of the ship along the paths. Paths are slightly offset so as to distinguish between overlapping ones.

On the October 2018 cruise, square and grid-search paths were introduced to combine the range dependence and the ship heading dependence together. When the ship traveled along these paths, its heading and range always changed from one point to another. The results showed that the ship heading did not have to be pointing radially outward or toward the hydrophones to affect the travel time perturbation. The effect of ship-heading dependence could be best exemplified by abrupt changes of the travel time perturbation at the corners and turns of these paths. At each corner the ships turned 90 degrees which changed its heading from pointing obliquely outward from the ACO to pointing obliquely toward the ACO. This caused the travel time perturbation to abruptly drop by 6 ms. This case was similar to the radial path case discussed above. When the ship moved along the straight lines, the gradual change of the travel time perturbation can be attributed to the range and heading dependences. All of this resulted in a skewed saw-toothed pattern of the travel time perturbation. **Figure 10** and **11**show the travel time perturbation and ship path plots for the square and grid-search paths.

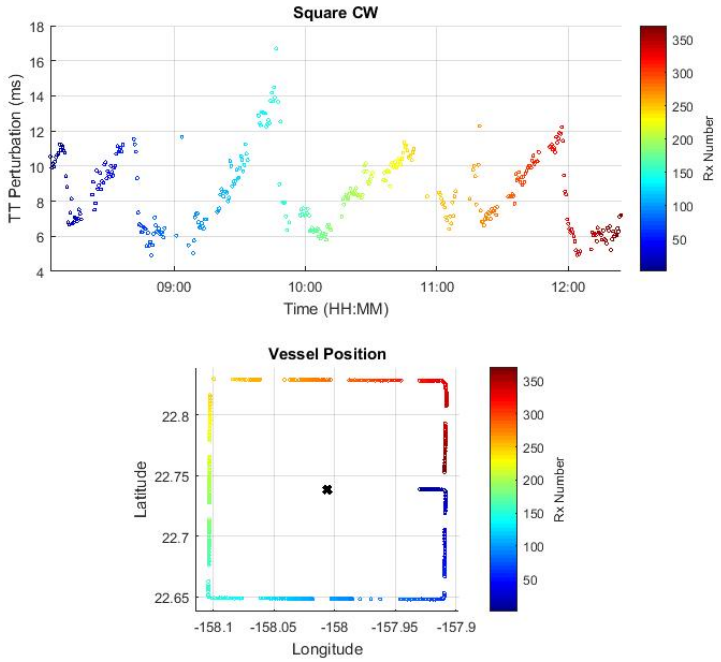

Figure 10. Travel time perturbation plot of a clockwise square path. The upper plot shows travel time perturbations versus time. The lower plot shows transmission coordinates. The color represents transmission order in the course

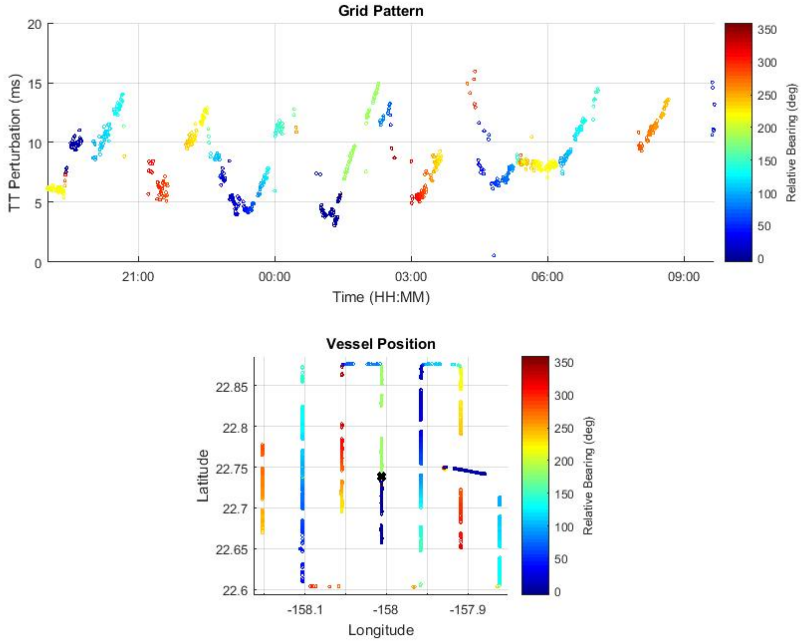

Figure 11. Travel time perturbation plot of a grid search path. The upper plot shows travel time perturbations versus time. The lower plot shows transmission coordinates. The color represents heading of the ship.

Errors in the POS MV position data could be responsible for these unusual patterns of the travel time perturbation. A simple signal validation was done by comparing the ship altitude data from the POS MV with the water level change (due to the tide) recorded by PacIOOS. This comparison was done on position data collected when the ship was at-dock in Honolulu prior to the cruises and when it was out at sea. Though the overall trends of the ship altitude data agreed well with the recorded tides at the several cm level, there were some periods in which the ship altitude went off from the nominal trends. This raised another concern about the reliability of the ship position data provided by the POS MV and called for a detailed study to assure the functionality of the POS MV.

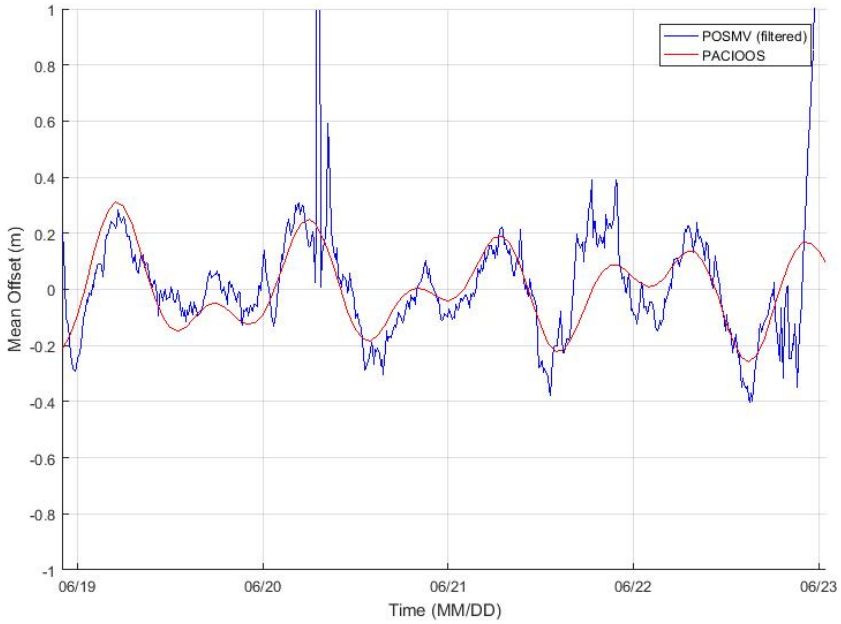

Figure 12. Comparison of mean offsets between the recorded water level change (red) and the POS MV altitude data (blue), while at dock in June 2018.

In June 2018, the icListen was installed at the ACO. It gives us an opportunity to verify and compare the data collected by the HEM hydrophone. After the installation, the icListen clock was synchronized with the Grand Master Clock at the on-shore station. In the meantime, the ship was holding its position above the ACO and sending out the 3.5 kHz pings. Ideally, acoustic reception times of both hydrophones should have been very close together (around 1.2 ms delay due to hydrophone height difference). However, there appeared to be a 1-second offset between the icListen's reception times and the HEM hydrophone's reception times. This offset became larger in October 2018. The offsets were believed to be exact integer seconds and would be

temporarily handled by adjusting the audio file timestamps with corresponding time offsets (See **Chapter 5**).

In the subsequent analysis on the October 2018 cruise data, the main goal was to resolve the heading and range dependences, and the ship position reliability issues. Additional GNSS positioning system “Trimble RTX” and another GNSS position data format produced by the POS MV “NMEA GGA” were introduced as independent datasets to compare with the original POS MV binary output data which had been used previously.

5. Hydrophones at the ALOHA Cabled Observatory

Upon the completion of the initial ACO deployment in 2011, the ALOHA Cabled Observatory has provided seafloor-mounted scientific instruments with the necessary infrastructure to make real-time measurements of water properties and transfer data to allow for continuous scientific research. In this chapter, we will discuss the physical configurations and electrical characteristics of these two hydrophones, as well as the timing issue mentioned previously.

Hydrophone Setup and Timing Method

Included in this setup is the Hydrophone Experiment Module (HEM) which includes a hydrophone from Optimum Applied System, Inc. (model E-2PD) sampled at 96 kHz. On a subsequent deployment cruise in June 2018, another hydrophone - icListen HF from Ocean Sonics., Inc. - was deployed. The icListen has operated since then with a sample rate of 32 kHz.

The HEM hydrophone is mounted to the HEM pressure case endcap on the Junction Box's (JB). This case is placed vertically on the Junction Box's frame under a fiberglass grid protection. At the ACO, the HEM hydrophone is on the side of the Junction Box which is directed to the east. The height from the seafloor to the HEM hydrophone is 0.85 m (**Figure 13**). The icListen hydrophone is mounted on the top of the metal frame of Basic Sensor Package 3 (BPS) which is 2.60-m high (**Figure 14**). The base of the BSP3 includes synthetic foam and a fiberglass grid. The estimated horizontal distance separation on the seafloor between the two hydrophones is 46 m. The seafloor configuration/locations have continuously been refined using ship-based survey data during each ROV dive through time. The instrument position estimates are accurate enough for most purposes, but when attempting to perform RAP tomography we need position accuracy of ~10 cm or better.

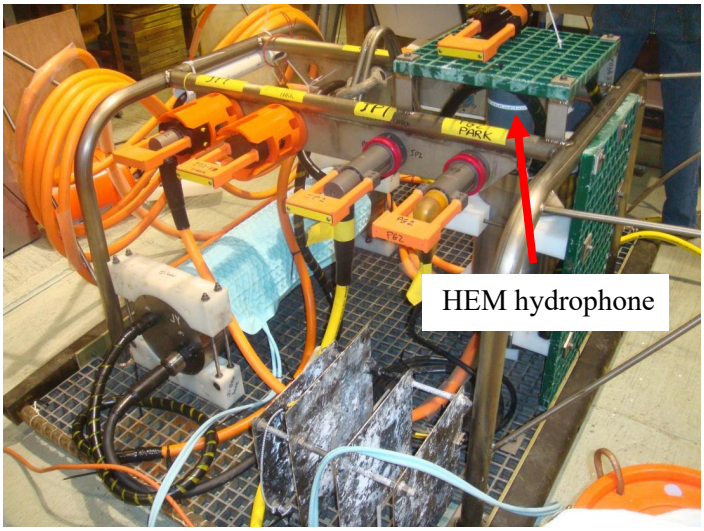

Figure 13. The Junction Box and the HEM module. The HEM pressure case is on the top right and is mounted vertically under a green protective fiberglass grid.

Figure 14. Basic Sensor Package 3 (BSP3) before deployment. The icListen hydrophone is vertically mounted at the top of the metal frame, with a flow-noise reducing "sock" over it. The height from the ground to the mounting is 2.60 m.

At the observatory, the HEM PC104 computer acquires the hydrophone data with a 24-bit data acquisition system. The PC104 software time-stamps the incoming data by adding timing headers every 4096 samples before the data is transferred and stored at the Makaha cable station. The HEM produces audio files with a nominal duration of 5 minutes. Timestamps of samples between two timing headers are obtained by linearly interpolating. A down-sampled version of the original audio sampled at 96 kHz is made available by digitally filtering the at 12 kHz and resampling at 24 kHz. The 24 kHz audio files are used in this project. The timing headers of the 24-kHz files are down-sampled accordingly as well. When comparing the 96-kHz and the 24-kHz files, there is a time lag of about 0.05 ms between the two (the phase lag from the filter), which was compensated when generating timestamps for the 24-kHz files in the subsequent analysis (Varamo, 2017).

The icListen hydrophone is also configured to generate audio files every 5 minutes. However, instead of having timing headers inserted within a file, each file name already carries the timing information with it. In this case, the timestamps of each sample are extrapolated from the start time of the file using knowledge of the sample rate. Starting times of the files are constrained to start on integer seconds.

The two hydrophones receive the time of day information from a GPS-synchronized NTP (network time protocol) server which distributes the GPS timing signals to all devices. The Tekron slave clock in the observatory J-BOX also provides the hydrophones with the 1 pulse per second (PPS) signal which is synchronized to GPS time using IEEE-1588v2 Precise Time Protocol (PTP) as served by a Tekron Grand Master Clock at the Makaha Cable Station. The HEM PC104 generates timing headers for the HEM audio files; it is constantly using NTP time to assign the correct time-of-day to the incoming PPS. On the other hand, the icListen only acquires the time-of-day information once when a synchronization command is sent to it. Afterward, the icListen increments every second using the 1 PPS signal.

Hydrophone Electrical Characteristics

Raw HEM audio files are stored in digital count units whose magnitudes were modified by several filters and the sensitivity of the hydrophone itself. The filters applied to the original 96-kHz HEM audio consists of an analog pre-amplifier, a high pass filter (to remove signals less than 0.01 Hz), a pre-whitening filter, an analog to digital converter that includes an 24-kHz anti-aliasing filter. The resultant hydrophone response has a flat band between 10 Hz and 10 kHz and

a roll-off at the high-frequency end. The pre-whitening filter causes the attenuation band between 0.03 Hz to 3 Hz to suppress micro-seismic signals (**Figures 15 (a)**).

The icListen had been calibrated by Ocean Network Canada and Ocean Sonics, Inc. to find the hydrophone response of two frequency ranges (0.5 – 1,000 Hz, and 10 kHz to 200 kHz). **Figure 15 (b)** shows the resultant response which assimilates data from a few calibrations. Unfortunately, we do not know the response from 1,000 Hz to 10,000 Hz where our signal of interest lies (3,500 to 5,000 Hz). The icListen response in the missing range is assumed to be linear. Therefore, the missing data is filled by linear interpolation between 1,000 Hz and 10,000 Hz (**Figure 15 (b)**). Above all, the icListen hydrophone's response is sufficiently flat over the whole bandwidth.

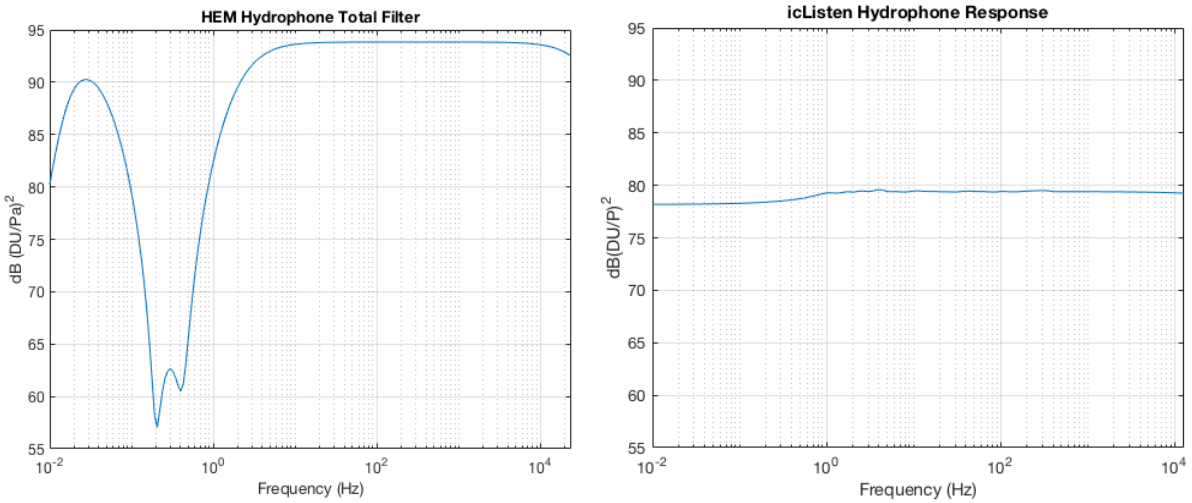

(a) (b)

Figure 15. (a) The total HEM hydrophone response in dB $(DU/Pa)^2$. (b) The total icListen hydrophone response in dB $(DU/Pa)^2$. The icListen's response is relatively flat compared to the HEM hydrophone response.

Figure 16 and **17** show the original acoustic signals of the HEM and icListen hydrophones in the digital count unit from the same time frame and the corresponding corrected signals in pressure units of Pascals. In the case of raw signals, the HEM hydrophone's audio contained larger amplitudes of LFM pings than the icListen. When the signals in the digital count unit were converted to the pressure unit, the shape of the HEM hydrophone's signal changed drastically while that of the icListen remained fairly unchanged. This substantial difference was attributed to the larger range of the HEM hydrophone response magnitude combined with greatly amplified energy below 1 Hz.

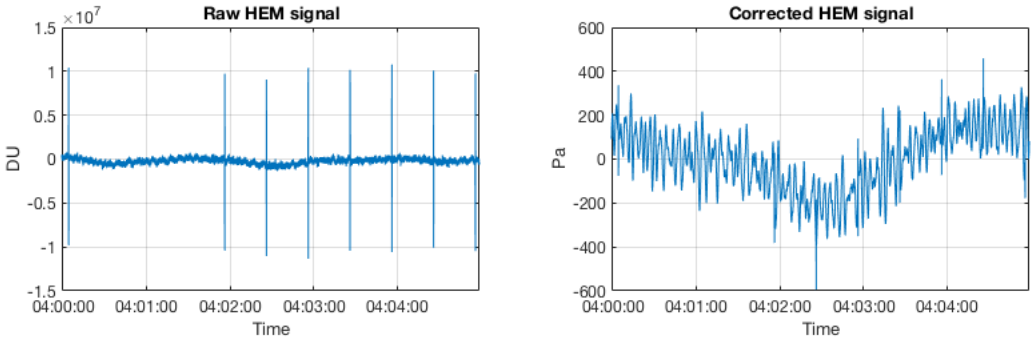

Figure 16. The HEM hydrophone raw (left) and corrected (right) acoustic signals.

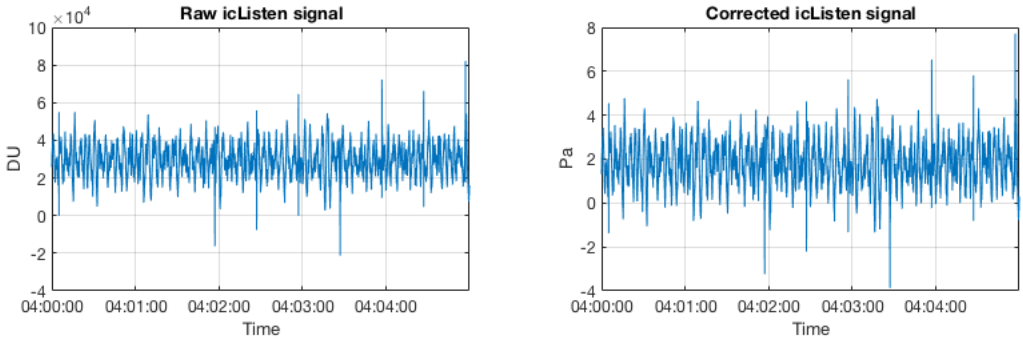

Figure 17. The icListen hydrophone raw (left) and corrected (right) acoustic signals.

Figure 18 and **19** show LFM signal reception samples and corresponding power spectral densities of the two hydrophones when the ship was overhead the ACO and the corresponding envelopes of the complex demodulates (in blue). The complex envelopes are the signals enclosing cross-correlation functions between the acoustic signals and the ideal LFM pulse (**Figure 67**). Prior to replica cross correlation of the data in digital units, the data were digitally filtered to pass energy between 2000 Hz and 6000 Hz. The red circles determine the picked arrivals where maximum cross-correlation values are located. In the case of the HEM hydrophone, the complex envelopes contained two distinct peaks which were approximately one millisecond apart. The second peak would represent the bottom-bounced arrival of the LFM signal while the first peak represents the direct arrival. In contrast, the icListen's complex envelope had only one distinct peak, which implied that the LFM signal reception did not contain the bottom-bounced arrival. This observation might be explained by acoustic absorption of the syntactic foam attached to the icListen's frame.

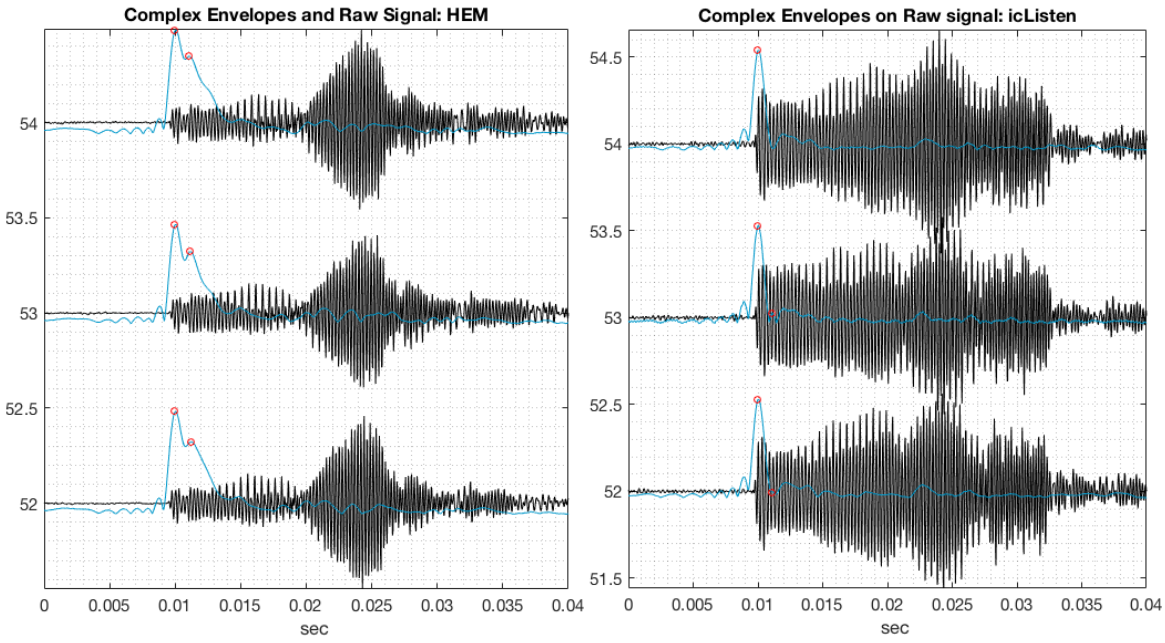

Figure 18. Acoustic receptions and envelopes of the cross-correlations when the ship was overhead the ACO. The HEM hydrophone (left) and the icListen hydrophone (right). Red dots and circles locate local maxima determining picked arrival times. Ordinate units are arbitrary.

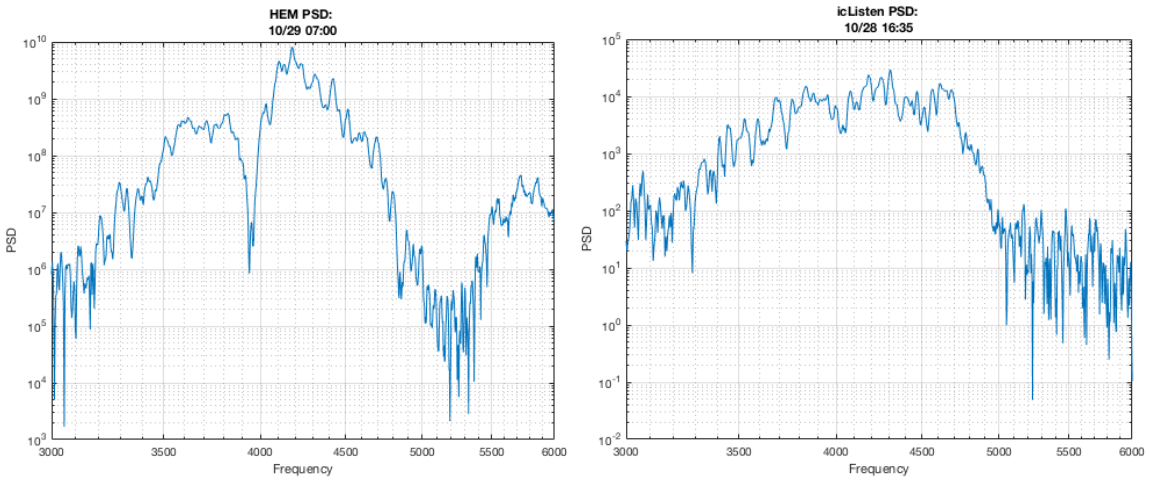

Figure 19. Power spectral densities of the HEM and the icListen when the ship was overhead the hydrophones. The y-axis is in dB (Power/Hz).

Hydrophone Timing Issue

After the icListen hydrophone was installed on 22 June 2018, it had its clock synchronized with the UTC time at 3:21 on the same day. **Figure 20** shows the result of the time synchronization. A ping was sent every 30 seconds from the ship which stayed stationary overhead the hydrophones. Although the icListen clock was already synchronized, there was still a time difference between the HEM hydrophone and the icListen. Before the synchronization, the icListen clock was lagging the HEM hydrophone clock around 15 seconds. After the sync, the time difference went down to 1 second in which the icListen was still lagging. This time difference cannot be attributed to a travel time difference due to horizontal distance separation between the two hydrophones.

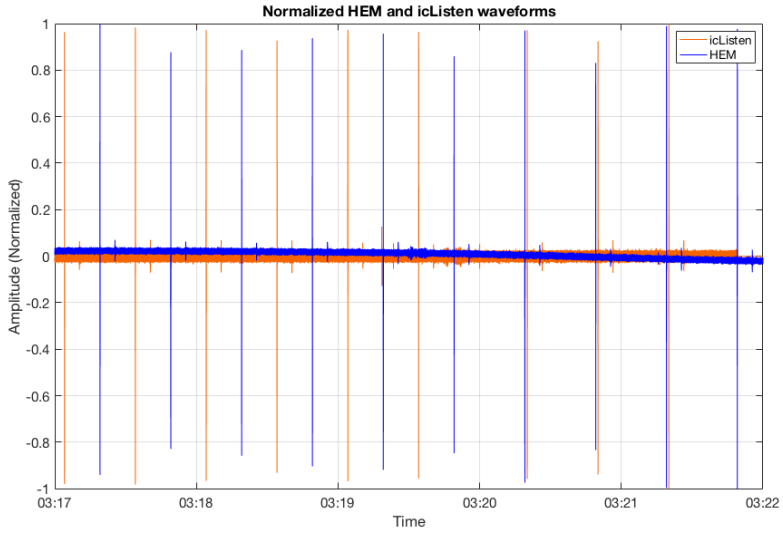

Figure 20 (a). Time offset between the HEM hydrophone (blue) and the icListen hydrophone (orange) in June 2018 normalized by the maximum values. The left half is before the synchronization. The right half is after the synchronization. The signals are 2000-6000-Hz band-pass filtered

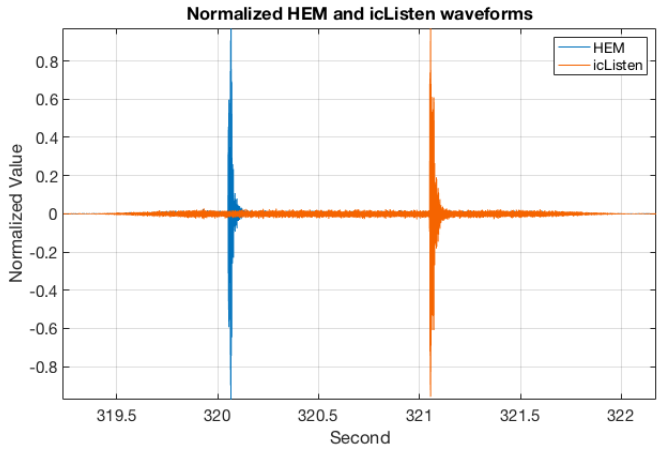

Figure 20 (b). A pair of HEM and icListen pings from the latter half in **Figure 21 (a**). The icListen hydrophone's ping (orange) is 1 second behind the HEM hydrophone's ping (blue). The signals are normalized by their maximum values.

On another cruise in October 2018, the same experiment was conducted. The synchronization of the icListen took place when the ship was about 10 km away from the hydrophone. The same issue regarding the time difference between the two hydrophones reoccurred (**Figure 21**). The icListen synced its clock with the UTC time once again. Before the synchronization, the icListen time was ahead of the HEM hydrophone time around 14 seconds. After the synchronization, the time difference went down to 6 second in which the icListen was still ahead.

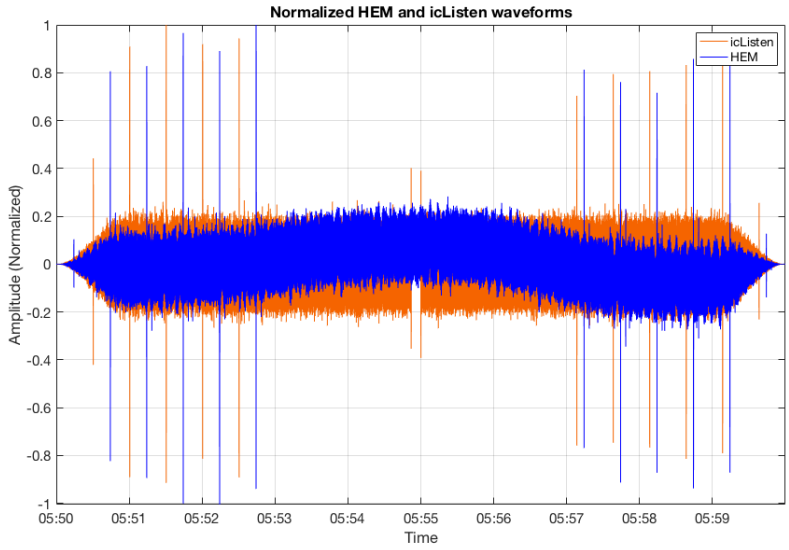

Figure 21. (a) Time offset between the HEM hydrophone (blue) and the icListen hydrophone (orange) in October 2018. The icListen becomes 6 seconds ahead of the HEM hydrophone after the synchronization was executed. The signals are 2000-6000-Hz band-pass filtered.

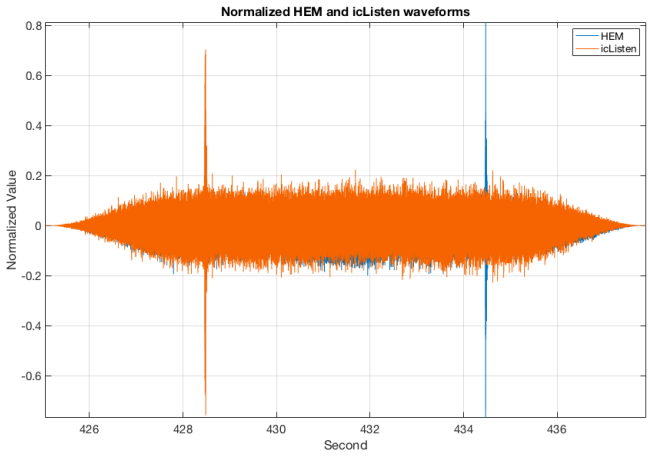

Figure 21. (b) A pair of HEM and icListen pings from the latter half in Figure 22 (a). The icListen hydrophone's ping (orange) is 6-second ahead of the HEM hydrophone's ping (blue). The signals are normalized by their maximum values.

In the subsequent analysis, we found that the HEM hydrophone data had four time jumps taking place during the experiment in October 2018. In the beginning of the cruise on October 27, the HEM hydrophone time was 4 seconds ahead of the UTC. Later, at around 1:00 UTC on 28 October, the HEM hydrophone time jumped 1 second away from the UTC time, resulting in a total of 5 seconds ahead of the UTC. The other two time jumps took place on 29 October and 30 October at 1:00 for both days. Each time jump shifted the HEM hydrophone time 1 second ahead from its original time. In contrast, the icListen time was consistent throughout the cruise with only one time jump occurring when its clock was synced with UTC. Before syncing, the icListen time was 7 seconds behind UTC. The time offset became 1 second ahead of UTC after the synchronization. These numbers were identified by calculating the estimated travel times of the acoustic signals to use them as time marks for signal arrival searching. The estimated arrival times of the signals in UTC can be computed by adding the estimated travel times to the transmission times. Then, we used those estimated arrival times as initial time marks to search for the corresponding signal arrivals in the HEM audio files. If there was no signal arrival found within +/- 1 second from the estimated arrival times, we kept extending the search time window out by another 1 second on both plus and minus sides, until the LFM signal receptions are found. The time jumps are believed to be integer seconds without any second fractions. Thus, in the analysis of the October 2018 dataset, these time offsets were used to adjust the timestamps of the HEM and the icListen audio files to reflect their absolute time with respect to UTC.

Subsequently, it was discovered that the Tekron slave had stopped serving NTP time and the PC104 had reverted to using its internal (drifting) clock to provide the time-of-day second. Once discovered (in November 2018), the PC104 was redirected to use the shore-side Tekron Grandmaster NTP server, and that resolved the problem. The issue of hydrophone time drift is of great concern in terms of reliability of the time-keeping mechanism at the observatory. However, in this study, we could obtain sufficient information about the acoustic travel time by compensating the audio's timestamps for the integer second time offsets. Hence, we could perform data analysis based on the adjusted timestamps.

6. GNSS positioning system comparison analysis

In this chapter, we compared ship position datasets provided by two Global Navigation Satellite System (GNSS) positioning systems, POS MV OceanMaster™ and Trimble RTX. The R/V *Kilo Moana* is equipped with an Applanix Position and Orientation System for Marine Vessels (POS MV) OceanMaster which provides the users with accurate real-time navigational data such as Geographic position, heading, and attitude. The system consists of two Global Navigation Satellite System (GNSS) receivers, two GNSS antennas, an Inertial Measurement Unit (IMU), and a POS Computer System (PCS). The processing method employed by the POS MV is called aided inertial navigation. In this process, a Kalman filter is used to blend the GNSS data with angular rate and acceleration data to produce the best estimate of position and velocity at a given time. Furthermore, the POS MV uses GNSS correction services of Marinestar™ (G2+) from the Fugro company to gain better accuracy of the position data. These services use a collection of satellites and 45 ground-based reference stations to compute errors associated with satellite tracks and clocks of a geographic position at a specific location and to correct the position data based on these errors. With these correction services and the aided inertial navigation, the POS MV can produce horizontal and vertical position data with accuracies of 10 cm and 15 cm at 95% confidence level, according to the system documentation. Also, the POS MV can provide data timestamps accurate to the microsecond level. To determine real-time positions of any specific location on the vessel, the POS MV requires the users to specify lever arms measured from a reference point (the granite block) on the ship to those locations. The POS MV can produce real-time position data of two “Sensors” simultaneously. We designated Sensor 1 to the reference point and Sensor 2 to the transmission transducer.

We can configure the PCS to output data in different types of data formats. A binary output format was set to contain Sensor 1 and Sensor 2 navigational data and corresponding performance metrics. This option is a default setting used by the POS MV. Another alternative is configuring the POS MV to generate data using the National Marine Electronics Association (NMEA) 0183 format. On the October 2018 cruise, we set the PCS to output Sensor1 and Sensor 2 position data in the binary format and the primary GNSS antenna position data in the GGA NMEA sentence format.

The other positioning system is "Trimble RTX." The RTX system has a separate GNSS receiver from the POS MV but shares the same GNSS antennas. Besides, it also employs an independent

GNSS position correction service which claims to provide horizontal and vertical accuracies of 2.5 cm and 5 cm respectively. This system is administered by James Foster from HIGP. The GNSS data recorded by the RTX is streamed via the internet to an operating computer at UH where it is logged and displayed online. The sample rate of the RTX is set to 1 Hz. It provides the geographic position of the GNSS antenna to which the RTX receiver is being connected with performance metrics.

Next, we discuss the R/V *Kilo Moana* coordinate system. **Figure 22** shows a ship plan containing the POS/MV coordinate systems. The coordinate system that we used has a granite block as the reference point. The most recent survey was done when the ship was at dry-dock during maintenance, in May 2017. Every lever arm of every shipboard device is measured with respect to the granite block. The primary GNSS antenna is assigned to the port-side antenna, and the secondary antenna is the starboard-antenna. The transmission transducer is located in the starboard hull of the ship. The POS MV binary output consists of position data of Sensor 1 and Sensor 2, which in this case are the granite block and the transmission transducer, respectively. The GGA NMEA sentence output and the RTX output report the geographic position of the primary antenna. **Table 1** summarizes the GNSS system configurations used in the October 2018 cruise.

GNSS Receiver	**Format**	**Sample rate (Hz)**	**Target**	**Data**
POS MV	Binary Output	10	Granite Block Transducer	Geographic positions, Ship dynamics and orientations, associated errors
	GGA NMEA sentence	1	Antenna	Geographic position, associated errors
RTX	RTX	1	Antenna	Geographic position, associated errors

Table 1. The parameters of the GNSS systems used on the October 2018 cruise

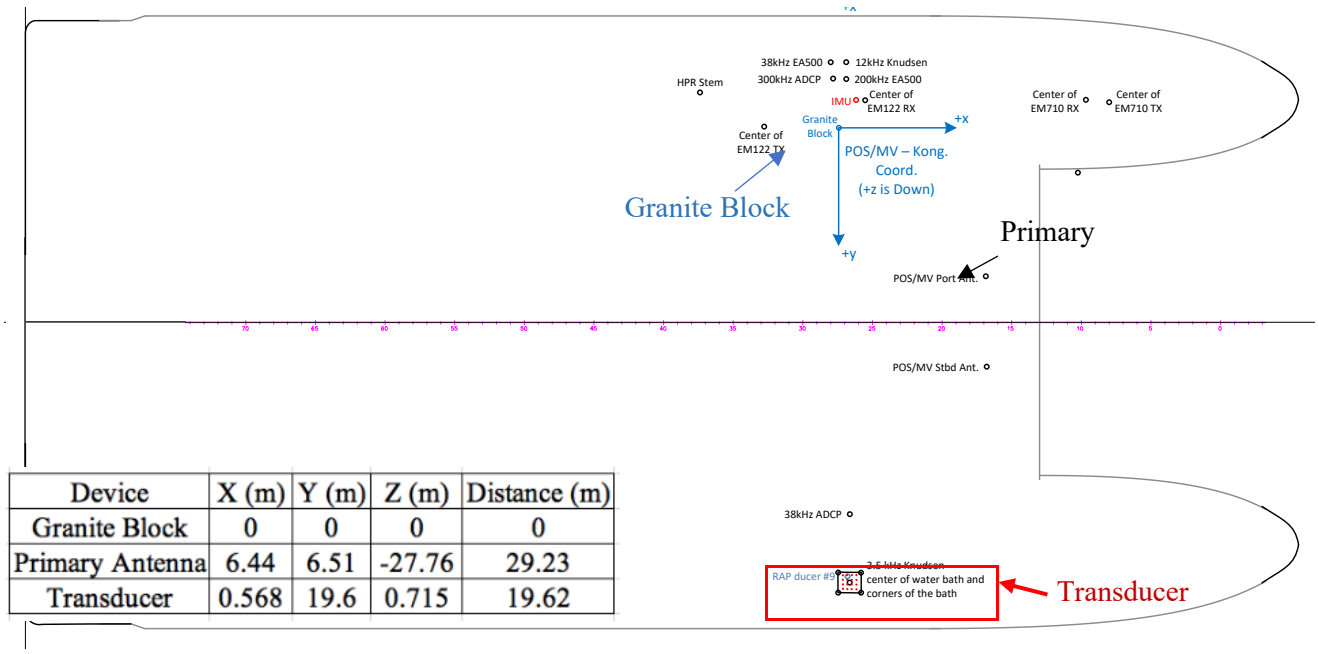

Device	X (m)	Y (m)	Z (m)	Distance (m)
Granite Block	0	0	0	0
Primary Antenna	6.44	6.51	-27.76	29.23
Transducer	0.568	19.6	0.715	19.62

Figure 22. The R/V Kilo Moana plan showing reference coordinate systems and shipboard devices. The current POS/MV coordinate system is in blue with the origin at the granite block. The transducer array is situated on inside the starboard hull. The table lists coordinates of the devices of interest.

In this analysis, to be able to make a one-to-one comparison, we had to consider two major differences among these datasets. Firstly, they did not sample at the exact same times. Considering the ship can be moving nominally at 10 knots or 5 m/s, sample time differences of 10 ms can cause position errors of tens of centimeters level; indicating we need to synchronize time series to this level or better. Secondly, they represented different shipboard devices (transducer and antenna). To handle the first issue, interpolation which accounts for ship movement and sample time differences among data points needed to be done. The timestamps of the POS MV binary output were used as the reference for this comparison. The data points of the RTX and the POS MV GGA NMEA output had to be interpolated from their timestamps to the nearest POS MV binary output's timestamps. This process used the longitudinal velocity of the ship and also angular rates from the POS MV binary output to compute for additional displacements of the antenna which occur within the time gaps. For the second issue, the POS MV binary output Sensor 1 and Sensor 2 had to be mapped to the GNSS primary antenna using coordinate transformation. To proceed the first step, the definitions of relevant coordinate systems needed to be established.

The reference ellipsoid is the coordinate system which GNSS satellites use as a reference. This reference ellipsoid is constructed to best approximate the oblate spherical shape of the earth. A geographic position is a point in 3 dimensions represented by latitude, longitude, and altitude. In geography and cartography fields, a 2-dimensional Cartesian coordinate system is widely used to give locations on the surface of the earth (or the ellipsoid). The Universal Transverse Mercator (UTM) coordinate system uses conformal projection to represent a point on a spheroid surface onto a planar surface. It divides the Earth surface into 60 zones, each has 6 degrees of longitude in width. To determine the location of a point in the UTM coordinate, we need to specify a zone number that the point belongs to, and the northing and easting coordinates. In this system, the x-axis corresponds to the easting coordinate and the y-axis correspond to the northing coordinate.

A locally-level ship frame is fixed to the ship reference point (the granite block). According to the POS MV reference system, the x axis corresponds to the ship longitudinal axis and is positive toward the bow. The y-axis corresponds to the ship transverse axis and is positive to the starboard. The z-axis is positive downward and perpendicular to the x-y plane (Applanix. 2016. POS MV V5 User Interface and Control Document). With all this in-place, we could calculate the antenna positions from the three datasets in the ship locally-level ship frame. For detailed calculation process, see **Appendix D**.

The analysis had two test conditions, when the ship was operating at-sea and when the ship was at-dock after the cruise. In the at-sea test, the differences between the antenna positions of the POS MV GGA and the RTX had medians close to zero with RMS values smaller than 10 cm in all three directions. The fluctuation ranges (4 standard deviations) of the horizontal positions and the vertical position were within 15.0 and 30.0 cm respectively (**Figure 23**). The antenna position from the POS MV sensor 1 (granite block) also agreed well with both the RTX and the POS MV GGA. However, the antenna position from the POS MV sensor 2 (transducer) had larger median differences than sensor 1, with the largest difference in the bow-stern direction (**Figures 24 and 25**). The fluctuation ranges (52.0 cm) appeared to be higher than the previous case due to inaccuracies from time-interpolation and transforming both sensors to the antenna.

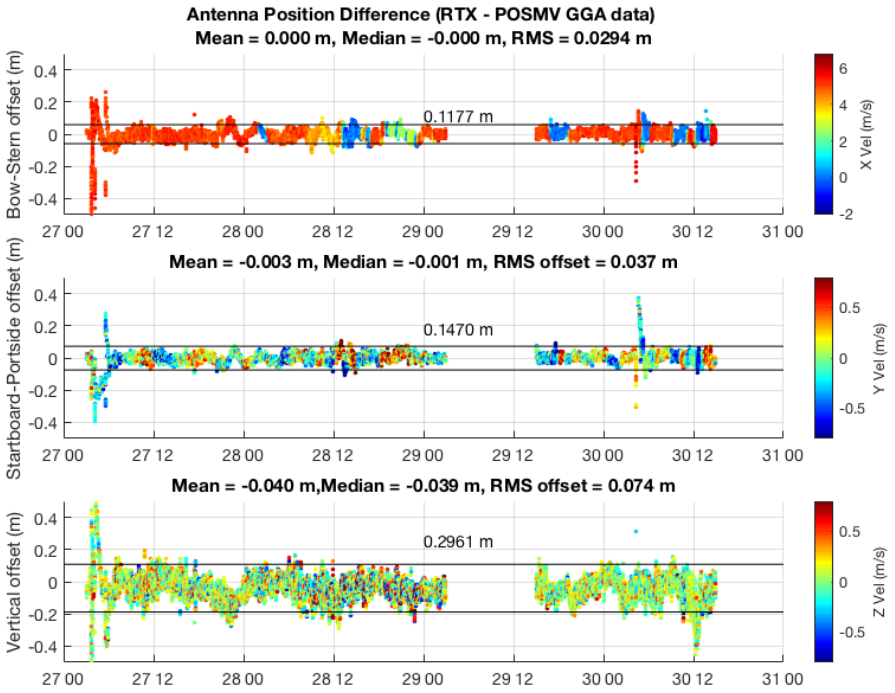

Figure 23. The position differences between the RTX antenna position and the POS MV GGA antenna position during the October 2018 cruise.

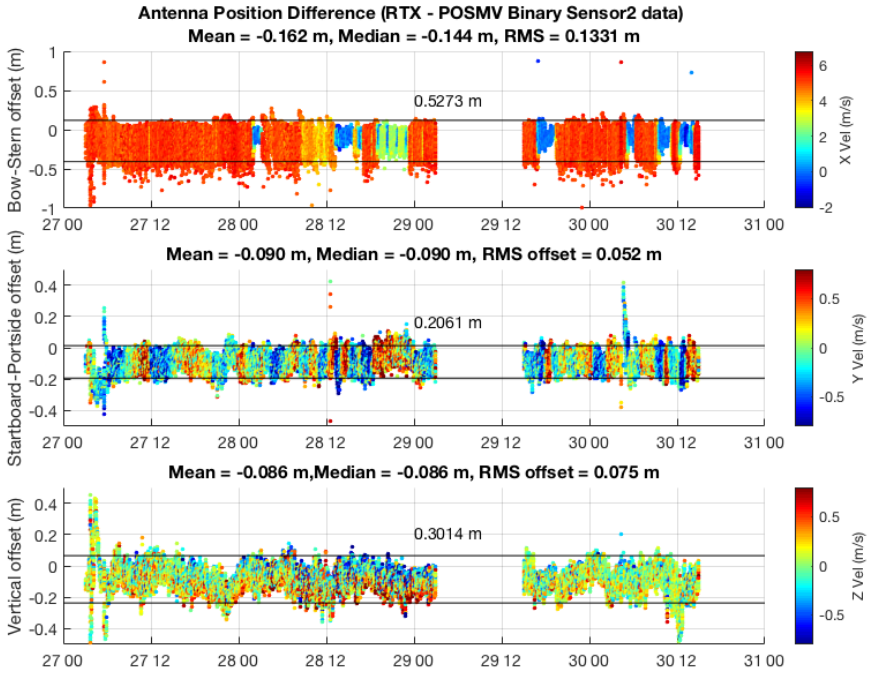

Figure 24. The position differences between the RTX antenna position and the antenna position based on the POS MV Binary transducer position during the October 2018 cruise.

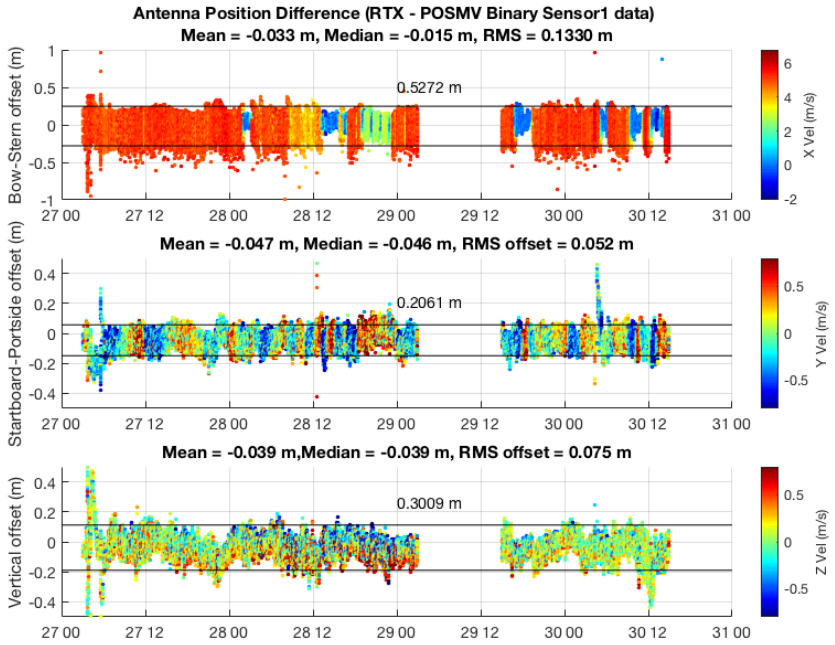

Figure 25. The position differences between the RTX antenna position and the antenna position based on the POS MV Binary granite position during the October 2018 cruise.

In the at-dock test, the same inference could be made in a similar fashion as the at-sea test. The differences among the antenna positions of different datasets and the variations were smaller than the at-sea case as the ship had little motion during the test. **Table 2** and **3** show a summary of median differences and RMS of the comparisons of the two cases.

Median	RTX vs GGA (cm)	RTX vs POSMV Binary (cm)		POSMV GGA vs POSMV Binary (cm)		Transducer from Granite Block (Binary) (m)
		Granite block (Sensor 1)	Transducer (Sensor 2)	Granite block (Sensor 1)	Transducer (Sensor 2)	
x	0/1.0	-3.3/1.9	-16.2/11.8	3.7/-3.6	-9.2/-12.8	0.697/0.705
y	-0.3/1.6	-4.7/-1.3	-9.0/-5.6	-4.4/-1.5	-8.8/-7.2	19.64/19.64
z	-4.0/-1.3	-3.9/-1.1	-8.6/-5.8	0.3/-0.2	-4.4/-4.5	0.762/0.762
absolute distance						19.670/19.670

Table 2. A summary of the test result reporting the medians of position differences between the GNSS datasets. The red color represents the at-sea data and the green color represents the at-dock data.

RMS	RTX vs GGA (cm)	RTX vs POSMV Binary (cm)		POSMV GGA vs POSMV Binary (cm)		Tranducer from Granite Block (Binary) (cm)
		Granite block (Sensor 1)	Transducer (Sensor 2)	Granite block (Sensor 1)	Transducer (Sensor 2)	
x	2.9/1.7	13.3/4.1	13.3/4.1	5.8/3.7	5.8/3.7	1.5/0
y	3.7/2.4	5.2/4	5.2/4	4.1/3.3	4.1/3.3	0/0
z	7.4/4.8	7.5/5.2	7.5/5.2	5.8/2.1	5.8/2.1	0.2/0
absolute distance						

Table 3. A summary of the test result reporting the RMS errors of position differences between the GNSS datasets. The red color represents the at-sea data and the green color represents the at-dock data.

Considering all cases, the POS MV sensor 2 or the transducer position data had the accuracy of the mean position within 9-16 cm, compared to the RTX and the POS MV GGA datasets. The RMS was in a range between 5 to 13 cm. These distance errors would correspond to sub-millisecond travel time errors at the limiting range (25 km), which were adequate given other comparable sources of errors. This analysis convinces us that the POS MV binary output data can be used with confidence in the subsequent analysis.

7. October 2018 Cruise

During 26-30 October 2018, the R/V *Kilo Moana* sailed again for the RAP project. At that time, we had two hydrophones operating at the ACO, the HEM hydrophone and the icListen hydrophone. **Figure 26** shows a summary map of the ship paths taken on this cruise. **Table 4** presents parameters of the experimental setup used on this cruise.

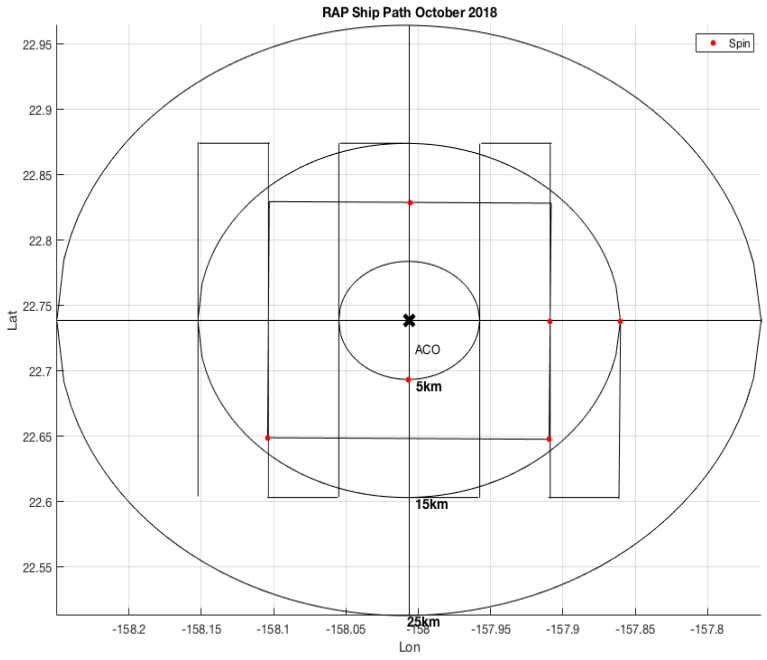

Figure 26. Ship paths taken on the October 2018 cruise. Red dots are "spin" locations.

Parameter	Description
Coded Signal	Linear-Frequency Modulated Signal
Sound level	199.5 dB
POSMV	Sample Rate 10 Hz
	Sensor 1 was granite block
	Sensor 2 was transducer no. 5

Table 4. Experiment parameters on October 2018 cruise

Preliminary Result

Acoustic signals received by the two hydrophones were cross-correlated with the ideal LFM replica to detect the LFM ping arrivals. The SNR threshold of signal detection was set to 9 (for the definition of SNR, refer to **Appendix B**). The signal receptions whose SNRs were lower than this threshold were discarded. The total number of detectable signal receptions of the HEM hydrophone was 5,167 (69 % of all transmissions), while for the icListen hydrophone the total number was 6,556 (88 %). The reason for the difference was not clear. The icListen audio appeared to be cleaner than the HEM. One interesting observation was when the ship moved in the clockwise direction (the transducer was on the outer side of the ship relative to the ACO), the HEM hydrophone could barely receive the acoustic signals. Further spectral analysis revealed that the spectral shapes of the received signals were dependent on the ship heading. These demonstrated a possibility of directionality of the acoustic reception which could be attributed to the interaction between the transmitted acoustic signal and the ship hull.

The travel time perturbations of all transmissions and receptions were computed using the same algorithms and processes as the previous cruises (**Appendix B** and **C**). **Figure 27** shows summary maps of the travel time perturbations from the two hydrophones on this cruise. Another way of data visualization to better emphasize the ship heading factor is to plot the travel time perturbations in a polar coordinate system (**Figure 28**). The angle of the plot represents the ship heading with respect to the ACO; it was defined by an angle between a radial line connecting the ACO and the ship and the ship heading. This relative heading can be expressed in this formula

$$Relative\ Heading = Heading - Azimuth \quad \textbf{(12)}$$

where azimuth is the angle of the ship with respect to the ACO. 0 azimuth is the north and the azimuth increases in the clockwise direction.

In short, the angle between 90 and 270 degrees represented the ship heading pointing inward to the ACO and between 270 and 360 degrees with the ship bow directly pointing away from the ACO.

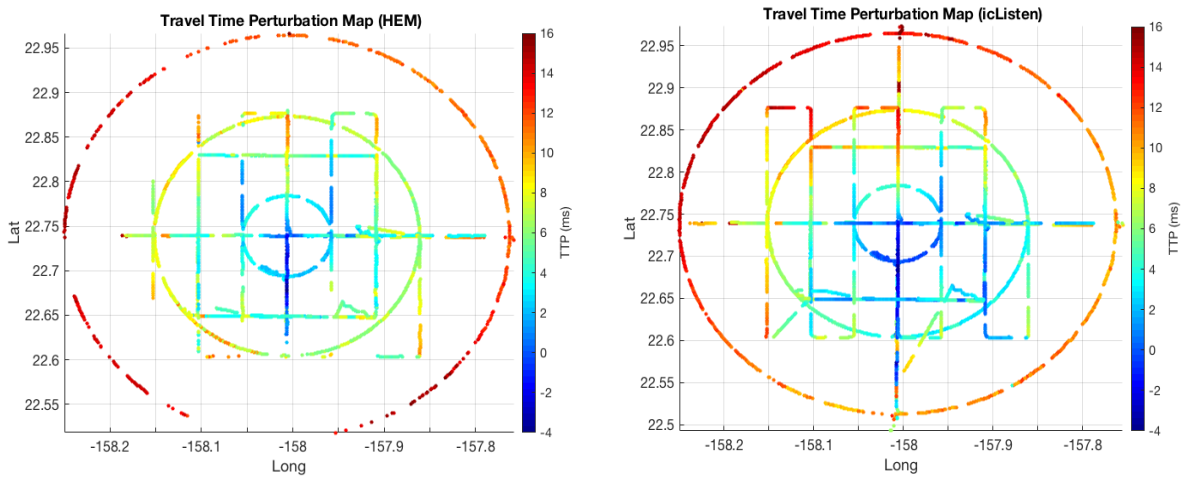

Figure 27. The maps of travel time perturbations. Left, the HEM hydrophone data. Right, the icListen hydrophone. Each point on the map represents a location of transmission, and the color represent the corresponding travel time perturbation.

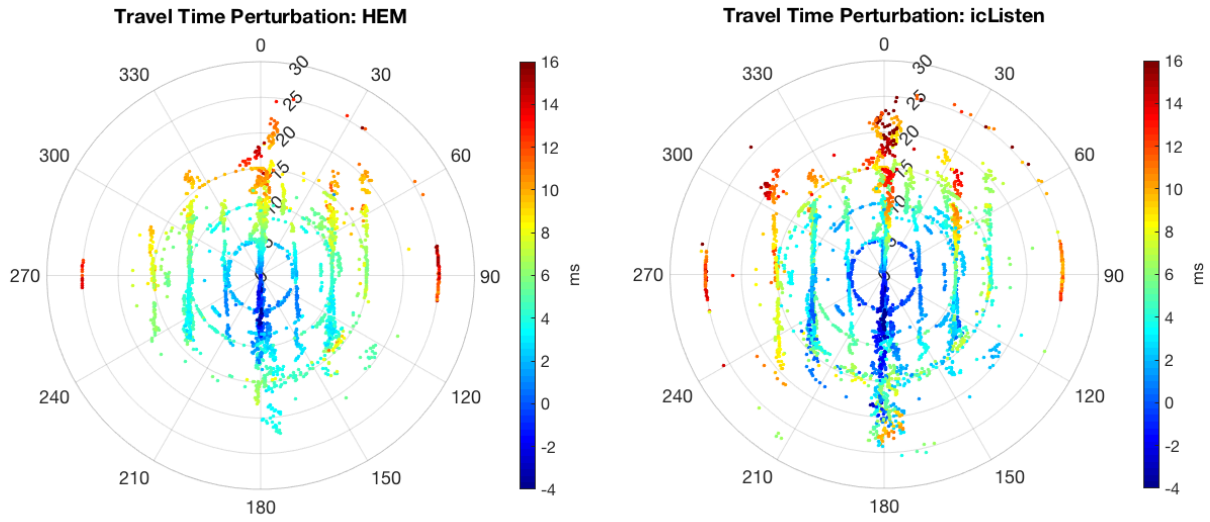

Figure 28. The travel time perturbation plot in the polar coordinates. Left, the HEM hydrophone data. Each point on the map represents a range and a relative heading of a transmission, and the color represent the corresponding travel time perturbation.

These plots showed an azimuthally unsymmetrical color pattern indicating that the travel time perturbation was heavily dependent on the relative ship heading. The travel time perturbation of when the ship was moving outward from the ACO was larger than when the ship was moving toward the ACO. However, a contradiction arose from the spin results. During the spin courses,

the ship held its position but consistently changed its heading. This test separated the ship-heading effect from the range and ship velocity effects. Interestingly, the travel time perturbations of the spin course were fairly constant at all headings (**Figure 29**).

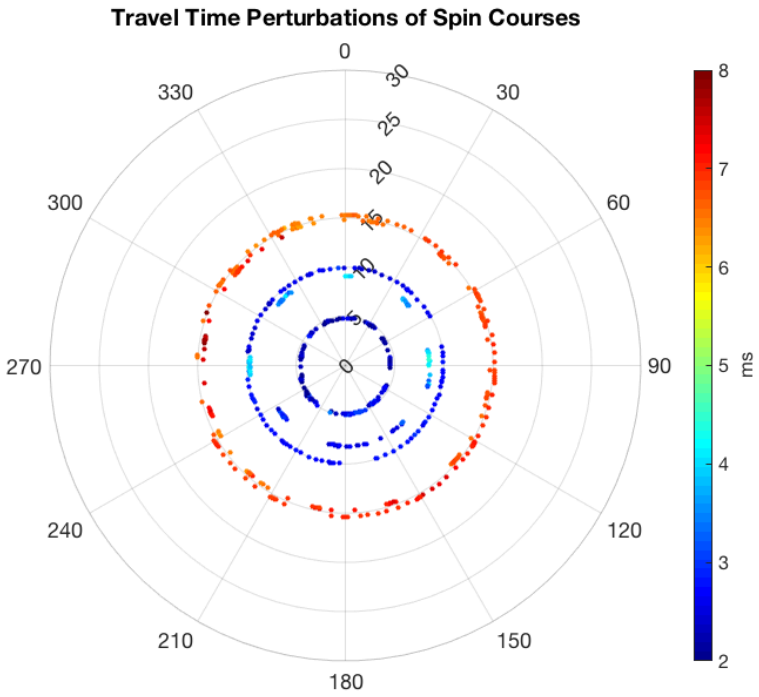

Figure 29. The travel time perturbation plot in the polar coordinates from the HEM hydrophone. Here, only data from the spins are displayed. The scatter at the same ranges has consistent color. This dataset does not exhibit the heading dependence of the travel time perturbation.

With these two observations, the travel time perturbation could be better represented as a function of the relative velocity rather than the relative heading. To quantify which factors contributed most to the travel time perturbation was to fit the travel time perturbation data to a linear model which included all possible combinations of the factors by using Lasso regression.

Lasso Regression analysis is called penalized linear regression which shrinks unimportant terms in the model. The penalty term λ ranges from 0 to 1. The larger the penalty term is, the greater the variables are penalized for contributing to "misfit" of the model. This technique allows us to choose a subset of variables which best represent the dataset and leave out irrelevant terms. We constructed a linear model of all possible combinations of range, ship heading, and velocity. The model is written in a form as

$$Travel\ Time\ Pertrubation = \beta_1 Range + \beta_2 V + \beta_3 \cos(\theta)$$

$$+\beta_4 Range \cdot V + \beta_5 V \cos(\theta) + \beta_6 Range \cdot \cos(\theta) + \beta_7 Range \cdot \mathrm{V} \cdot \cos(\theta) \quad \textbf{(13)}$$

where β_i is linear coefficient.

When the penalty term grew larger, only "$Range$", "$V\cos(\theta)$", and "$Range \cdot \cos(\theta)$" terms remained. This confirmed the previous observations on the range dependence and the relative-velocity dependence (**Figure 30**). In terms of the ship relative-velocity dependence, it implies three possibilities of the root cause: firstly, errors in the POS MV positioning system due to POS MV internal processing; secondly, errors in arrival time measurements due to Doppler effect; and thirdly, time delays within the systems.

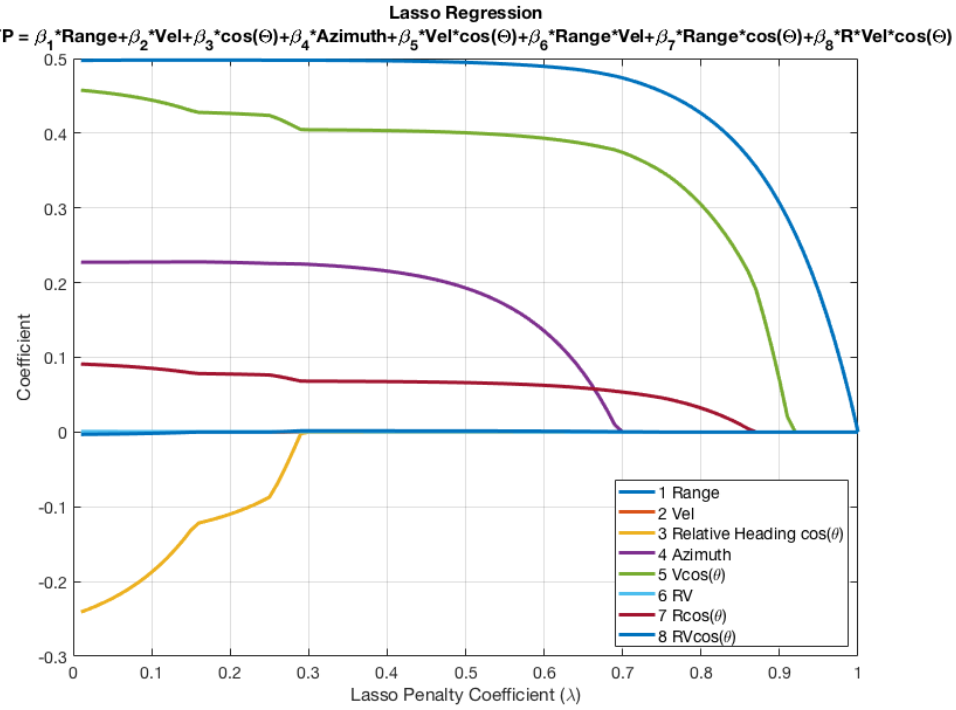

Figure 30. Lasso Regression on the HEM hydrophone's travel time perturbations.

The first possibility was rejected by the comparison results between the POS MV binary out and the RTX and the POS MV GGA NMEA sentence outputs which proved the adequacy of the POS MV binary output accuracy (**Chapter 5**). Next, an investigation of possible Doppler effect was conducted. The Doppler effect is a phenomenon in which the frequency of a transmitted wave is

shifted due to the source movement (given that the receiver was stationary in this case). The formula quantifying the magnitude of the frequency shift is

$$\frac{\Delta f}{f} = \frac{v}{c} \tag{14}$$

where Δf is Doppler shift frequency, f is the frequency of the transmitted signal, v is the source speed, and c is sound speed.

A simulation case was created to see how large the travel time errors incurred from the frequency shift. **Figure 31** shows an effect of the Doppler effect on the travel time measurement errors in a case when the ship moved at the maximum speed of 5 m/s. The plot was made by cross-correlating a signal with frequency-shifted LFM replicas. The y-axis indicates the quantity of LFM replica's frequency shift. When the ship was moving at the maximum speed, the Doppler shift was calculated to be 13.5 Hz, but the simulation extended the frequency shift range out to 50 Hz. If the frequency shift was present, the most considerable travel time error due to Doppler shift will be less than 0.5 ms, which was substantially smaller compared to the magnitude of travel time perturbation errors of concern. This case study suggested that the Doppler effect does not account for the errors of the travel time perturbation measurements.

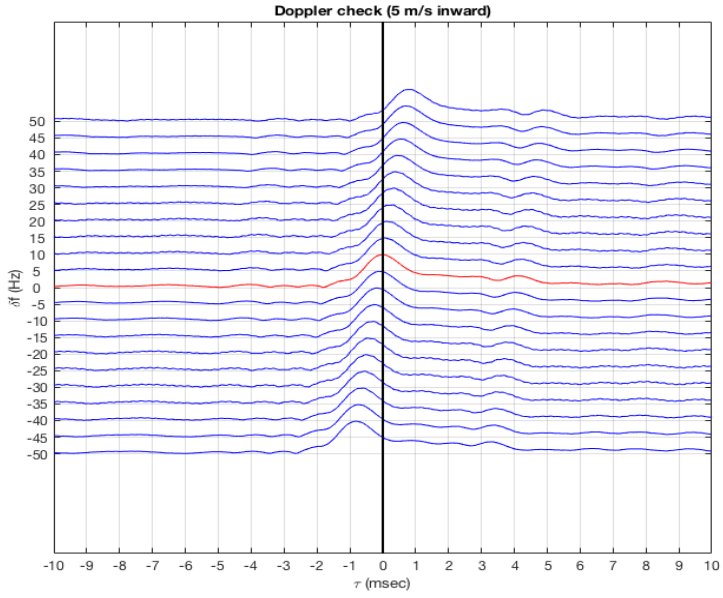

Figure 31. Doppler shift simulation. The red line represents the original complex envelope of a signal whose peak identifies the arrival time. The x-axis is the time delays of picked arrival times from the original signal.

Acoustic Transmission System Delay

Since, the velocity-related effect could not explain the travel time errors, consequently, other variables associated with velocity were brought into question. According to the results from the spin courses, when the ship did not move (linear velocity was zero), the travel time perturbation did not vary with the heading, implying that the transducer position errors were not present. This could be explained only by the variable "time". What appeared to be transducer position errors could be only an artifact of a time delay in the system. In the process of investigation of inherent delays in the acoustic transmission system, the system delay of 0.304 ms had not been included when computing for the estimated arrival time in the previous cruises (**Chapter 3**). When that time delay was incorporated, the ship heading dependence issue was resolved. **Figure 32** shows updated travel time perturbation plots in the polar coordinates. The colors of the scatters in the polar plots became symmetric. Yet, the travel time perturbation was still a function of range. **Figure 33** shows the travel time perturbation versus range with the color code representing the azimuthal angles of the transmission points with respect to the ACO. The icListen hydrophone's data gave the same result as the HEM hydrophone.

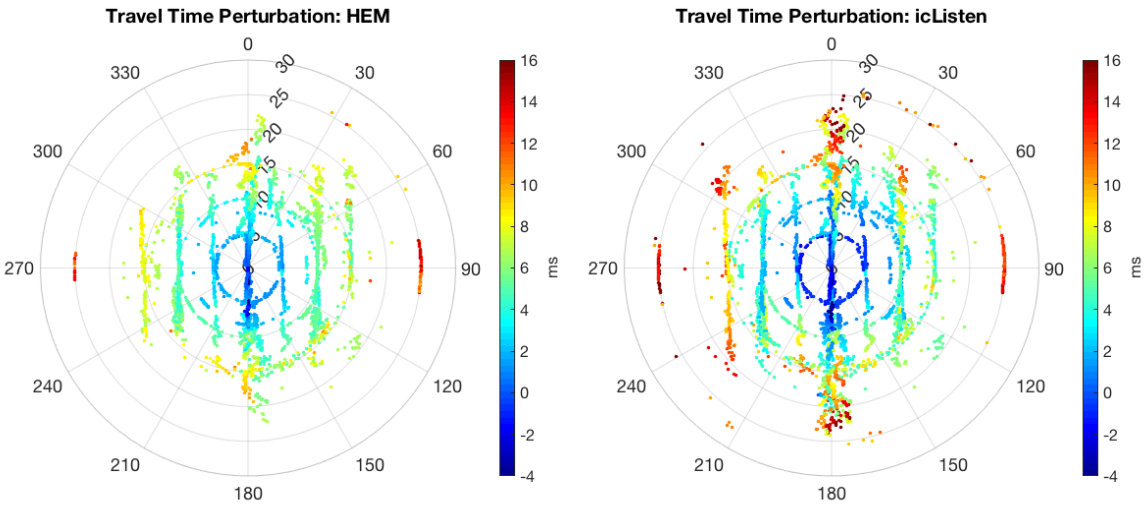

Figure 32. The travel time perturbation plot in the polar coordinates included time delay. Left, the HEM hydrophone data. Right, the icListen data. Each point on the map represents a range and a relative heading of a transmission, and the color represent the corresponding travel time perturbation.

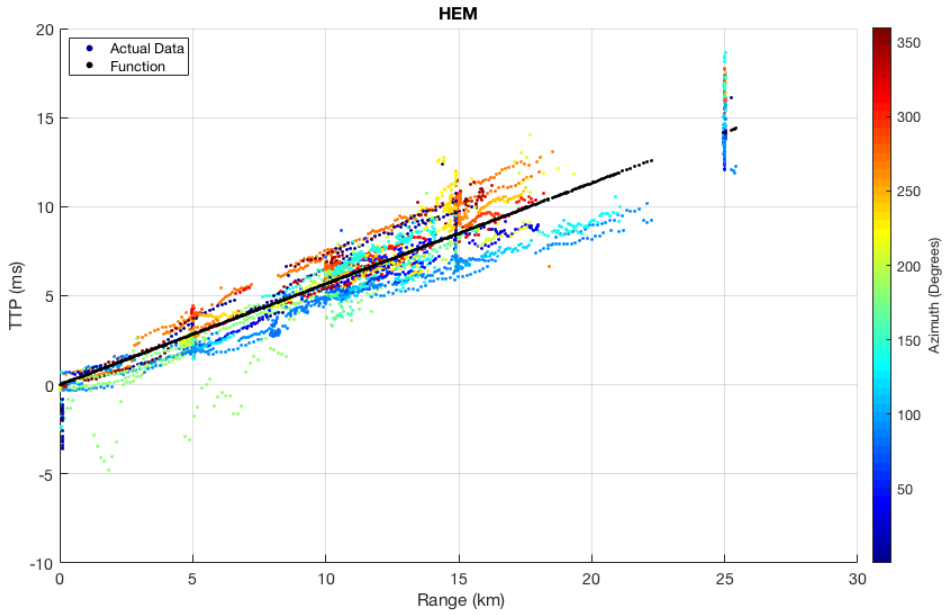

Figure 33. Travel time perturbation versus Range from the HEM hydrophone's data. The black dots represent a fitted function *f(Range) = 0.462 x Range(km)* resulted from Lasso regression.

For the range dependence, the increase in travel time perturbations with range could be a cumulative error caused by inaccuracy of the ray tracing model. To verify the accuracy of the layer-wise constant sound speed model, a constant sound speed gradient model was introduced to compare with the original model. In this model, sound speed varies linearly within a layer. The sound speed gradient causes the ray path to travel along a curved path which is an arc of a circle. A simulation of travel times computed using these two models was conducted. The same earth flattening transformation formula was applied to the depths and the sound speeds. The equations of the two ray tracing models are presented in **Appendix C**.

The outcome of the new model had no significant differences from the old model. Thus, this comparison convinced us that the layer-wise constant sound speed ray tracing model was adequately accurate for our purpose (**Figure 34**).

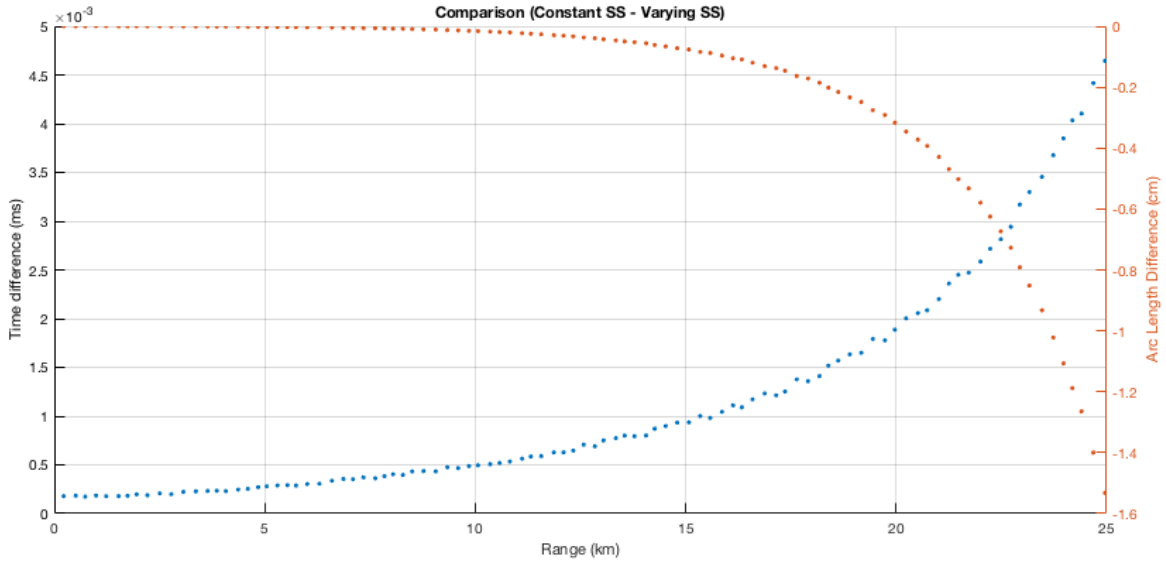

Figure 34. Comparisons between the old ray tracing and the new ray tracing methods. The left y-axis represents travel time differences and the right y-axis represents the ray path length differences of various surface ranges up to 25 km. The maximum travel time and ray path length differences are 0.0047 ms and 1.6 cm respectively at 25 km.

Ray Tracing

Modeling of sound propagation in the ocean works best in the earth frame of reference. For short-duration signals, the ray theory is practical to predict the propagation paths of sound. A representative geometry which best describes the shape of the Earth is a rotational ellipsoid. Solving ray propagation equations modeled in the ellipsoidal coordinate system can yield a result with accuracy to 1 microsecond for 10-20 km propagation range. The ellipsoid has its origin coincident with the center-of-mass of the earth and its surface defined by the semi-major axis and the semi-minor axis. The GPS reports the position above with respect to the ellipsoid, which is called geodesic position. The position is determined by three parameters; latitude, longitude, and ellipsoidal height. The 0-degree longitude is called the prime meridian which passes through Greenwich. In this context, the positive longitude is defined to be east of the prime meridian ranging from 0 degrees to 360 degrees; and the positive latitude is defined to be north of the equator. The ellipsoidal height is defined to be positive above the ellipsoid in the local vertical direction. There are various types of reference ellipsoids available, but the most common one is the WGS84 reference ellipsoid, which was used in this study.

In practice, the Earth's gravity and rotation, and ocean circulation deviate the true ocean surface from the ideal ellipsoidal surface. The geoid is a shape of the average ocean surface which is measured directly from the gravity of the Earth. Its surface is called an equipotential surface which reflects local bathymetry, topography, and gravity. Therefore, the height deviations of the geoid from the reference ellipsoid vary from place to place. The geoid height is the height of the geoid above the ellipsoid which is positive upward. The height that we are most familiar with is the orthometric height which is the height relative to the geoid (or local mean sea level).

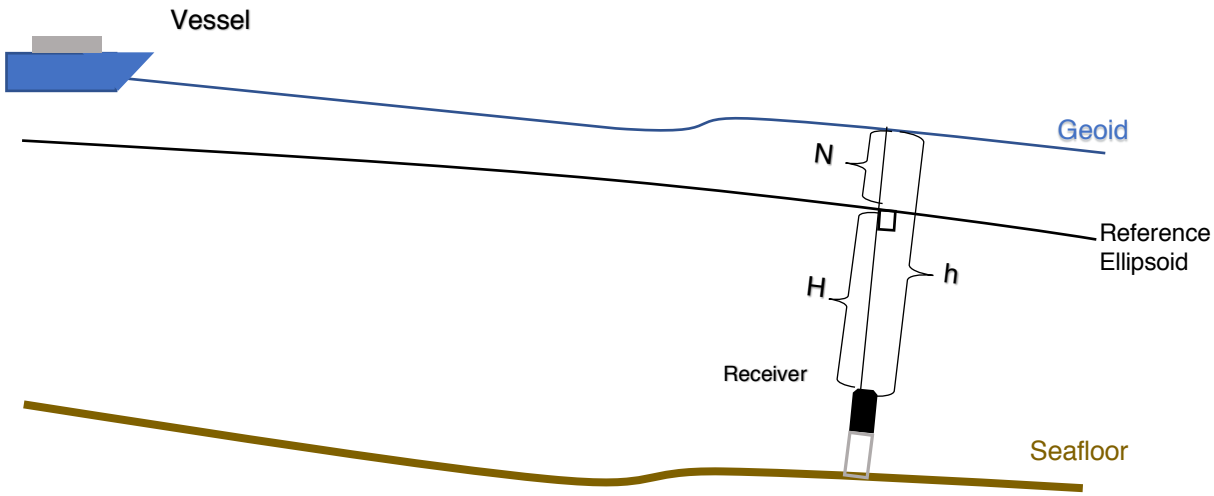

Figure 35. A diagram of the geodetic reference levels. *H* is the ellipsoidal height which is reported by GNSS position data, *h* is the orthometric height, and *N* is the geoid height.

Tracing ray paths requires the information of local sound speed profile. In this study, the propagation range was limited to 25 km, which was a small length scale compared to regional variability. Hence, it was safe to assume that lateral variation of the sound speed due to oceanographic features is negligible (for this purpose). However, there is a non-oceanographic source of lateral variations which needed to be addressed. Conventionally, the sound speed profile along the vertical axis is obtained by CTD casts. The CTD profiles report temperatures and salinities at corresponding pressures with respect to the local mean sea level. To perform ray tracing in the ellipsoidal coordinate system, we need to convert the sound speed profile from relative to the mean sea level (geoid) to the ellipsoidal surface. As the geoid height depends on locations, the sound speed profile would be a function of locations as well, which introduces lateral sound speed variations. For the area of the ACO, the geoid height changed by 1 m from

the northwest to southeast (**Figure 36**) while the CTD profile from the HOTS project has a depth resolution of only 2 m. Thus, to simplify the problem, the average geoid height of 2.31 m was applied to the sound speed profile which in turn eliminated the range dependence caused by changes of the geoid height (Chadwell et al, 2010).

Figure 36. The geoid height map of the area of interest. The color represents the geoid heights which range from 1.9 m to 2.9 m.

The most computationally-effective technique to implement a ray tracing algorithm which yielded sufficient accuracy for this study was a spherical earth approximation model with earth flattening transformation. The earth flattening transformation was used to project the source and receiver points, and the sound speed profile from the spherical earth coordinate system onto the planar earth. The flattened heights and sound speed profile are given by

$$h_f = R \ln\left(\frac{R}{R-h}\right) \tag{15}$$

$$c_f(h_f) = c(h)\frac{R}{R-h} \tag{16}$$

where R is a radius of the earth which best approximates the local ellipsoid. One of several definitions for R is the average radius along the azimuth from the source to the receiver. This definition approximates the curvature in the direction from the source to the receiver

$$R = \frac{1}{\cos^2(\alpha)/M_\lambda + \sin^2(\alpha)/N_\emptyset} \tag{17}$$

where $N_\emptyset$ is the radius of curvature of the prime vertical of the ellipsoid, and M_λ is the radius of curvature of the meridional of the ellipsoid. These radii are defined as

$$M_\lambda = \frac{a(1-e^2)}{(1-e^2\sin^2(\emptyset))^{3/2}} \tag{18}$$

$$N_\emptyset = \frac{a}{(1-e^2\sin^2(\emptyset))^{1/2}} \tag{19}$$

where a is the semi-major axis of the ellipsoid, and e is the eccentricity.

By using this approach, the spherical earth ray tracing can be implemented in the planar ray tracing scheme which is fast and convenient to implement as presented in **Appendix C**. The result from this approach agrees with the ellipsoidal earth ray tracing model to submillimeter (Chadwell et al, 2010). **Figure 37** shows the differences in depths and sound speeds between the old ray tracing model and the new one.

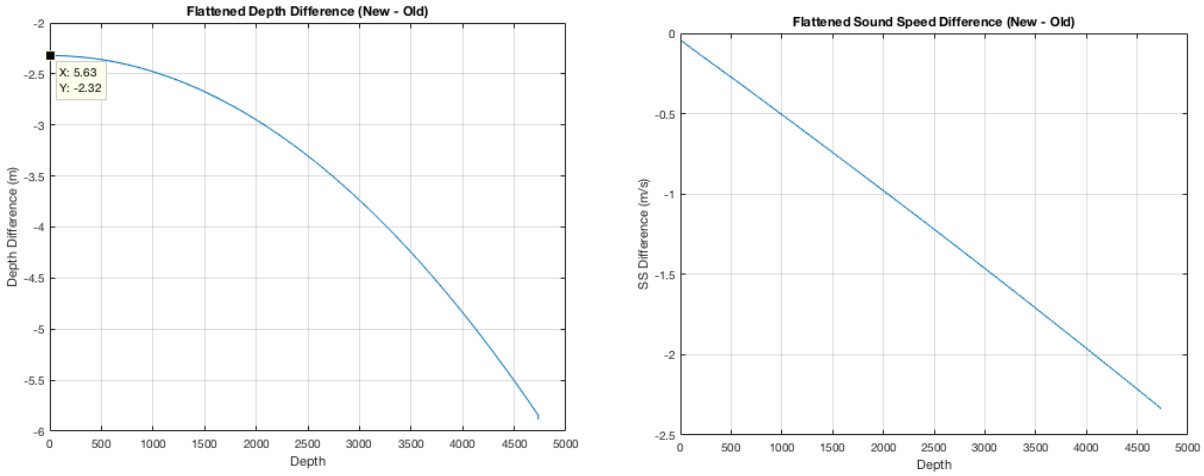

Figure 37. Differences between the old and new depths and sound speeds after stretched by the earth flattening transformation. The depths are deeper and sound speeds are slower.

With the new ray tracing model, the range dependence of the travel time perturbation was resolved. **Figure 38** and **39** show the final travel time perturbations of the HEM and the icListen.

The travel time perturbations became more realistic, with some biases due to hydrophone position offsets. These travel time perturbations will be used in the inversion procedure to solve for sound speed perturbation fields.

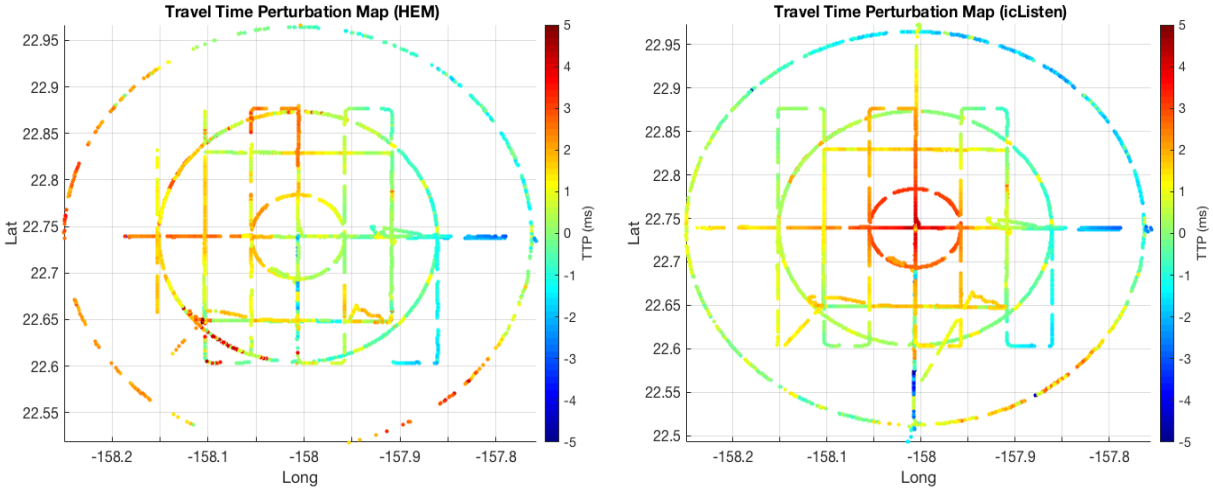

Figure 38. The updated maps of travel time perturbations after corrected for ray tracing. Left, the HEM hydrophone data. Right, the icListen hydrophone data. Each point on the map represents a transmission location, and the color represents the corresponding travel time perturbation.

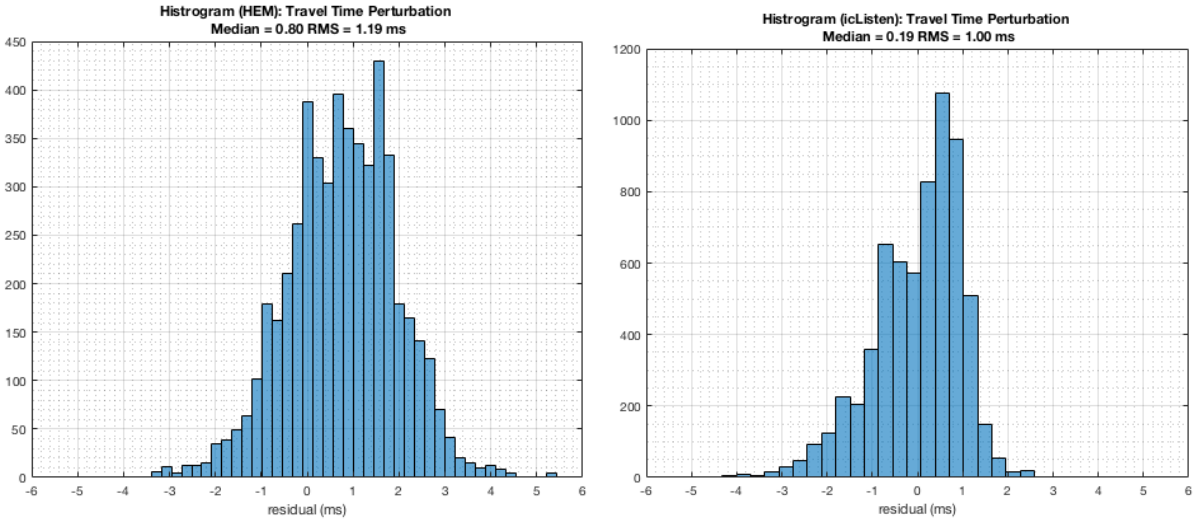

Figure 39. The histogram of the travel time perturbations. Left, the HEM hydrophone data. Right, the icListen hydrophone data. The HEM travel time perturbation has a median of 0.80 ms with 1.19 ms rms and the icListen travel time perturbation has a median of 0.19 ms with 1.00 ms rms.

8. Inversion Procedure

This chapter is divided into two parts. The first part will present the linear inversion technique including the choices of parameterization applied to a computational model and the performance metrics for assessing the model. The second part will present simulation cases to test the performance of the computational model.

Computational Model

From the previous chapters, we have obtained ray geometries of all transmissions made at various ranges and azimuths. Associated travel time perturbations of individual rays were also calculated. To solve for sound speed perturbation, we need to parameterize the sound speed perturbation in space. A general representation of sound speed perturbation can be expressed as

$$\mathrm{c}'(x,y,z) = \sum_i \sum_j \alpha_{ij} \mathrm{E}_i(x,y)\, v_j(z) \tag{20}$$

where $\boldsymbol{v}_j(z)$ and $E_{\mathbf{i}}(x,y)$ can be any basis functions which are left freedom for us to choose, and α_{ij} is the corresponding amplitude of the vertical basis functions j.

For simplicity, the horizontal basis functions and a vertical basis function j can be grouped together and represented by a 3-dimensional basis function $\mathrm{F}_j(x,y,z)$. **Equation 20** becomes

$$\mathrm{c}'(x,y,z) = \sum_j \mathrm{m}_j \mathrm{F}_j(x,y,z) \tag{21}$$

where m_j is the amplitude of the basis function F_j

By substituting **Equation 21** into **Equation 11**, and using d_i to represent travel time perturbation of ray i, **Equation 11** becomes

$$d_i = = -\int_{\Gamma_i} \frac{ds}{{c_o}^2(x,y,z)} \sum_j \mathrm{m}_j \mathrm{F}_j(x,y,z) \tag{22}$$

The ray path Γ_i and the arc length ds define the x, y, z coordinates of F_j which are included in the integral.

Generally, the lateral change of the reference sound speed profile is insignificant for short-range acoustic propagation. Therefore, $c_0(x, y, z)$ can be treated as a function of depth c0(z) only. By rearranging the terms in **Equation 22,** the travel time perturbation can be described as a linear sum of path-integral of all 3-dimensional basic functions

$$d_i = -\sum_j m_j \int_{\Gamma_i} \frac{F_j(x, y, z)ds}{{c_o}^2(z)} \tag{23}$$

where the integrand is called "ray weighting function" which represents the projection of the ray on a given basis function (Cornuelle and Howe, 1987).

The sensitivity of travel time perturbation of a ray *i* to vertical basis function *j* is defined as (Cornuelle and Howe, 1987)

$$G_{ij} = \left(\frac{\partial d_i}{\partial m_j}\right) = \int_{\Gamma_i} -\frac{F_j(x, y, z)ds}{{c_o}^2(z)} \tag{24}$$

where d_i is equivalent to t_k and m_j is equivalent to $c'(\underline{x})$ in **Chapter 2**

Based on **Equation 23**, a discrete computational model is constructed and expressed in a matrix form

$$\mathbf{d = Gm + n} \tag{25}$$

where **d** is the measurement vector, **m** is the model vector, **G** is the observation matrix or a sensitivity matrix. A noise term **n** is introduced to account for errors due to the sound speed perturbation field representation and inaccuracies in the measurements and other sources. In this study, the measurement vector contains travel time perturbations, the model vector contains sound speed perturbations and hydrophone position offsets, and the observation matrix is defined by **Equation 24**

Here, we chose empirical orthogonal functions (EOFs) to be the vertical basis representation $v_j(z)$ and a set of grids or pixels to be the horizontal basis $\mathrm{E}_i(x, y)$. In the physical sense, these representations reflect the structure of the sound speed perturbation variability in the vertical and the horizontal planes, and they are considered a priori information which is imposed on the computational model.

The vertical basis functions were derived statistically by calculating empirical orthogonal functions (EOFs) from sound speed variations among HOT 114 CTD casts relative to monthly averages at the ACO. The Singular Value Decomposition technique was used to calculate principal components of the spatial sound speed variation (Varamo, 2017). The result from the analysis showed that the first four modes (or principal components) amounted to 92.72 % of the total sound speed variation. As seasonal changes are subtracted, these model shapes are driven by ocean features propagating through the ocean. Since mode 1 has the highest loading, it implies that the majority of the ocean variability takes place in the upper ocean above 1,000 m, which is reasonable given that the thermocline usually extends to 1,000-m depth. Therefore, in the subsequent calculation, we included the first four EOF modes to represent the vertical sound speed variation structure.

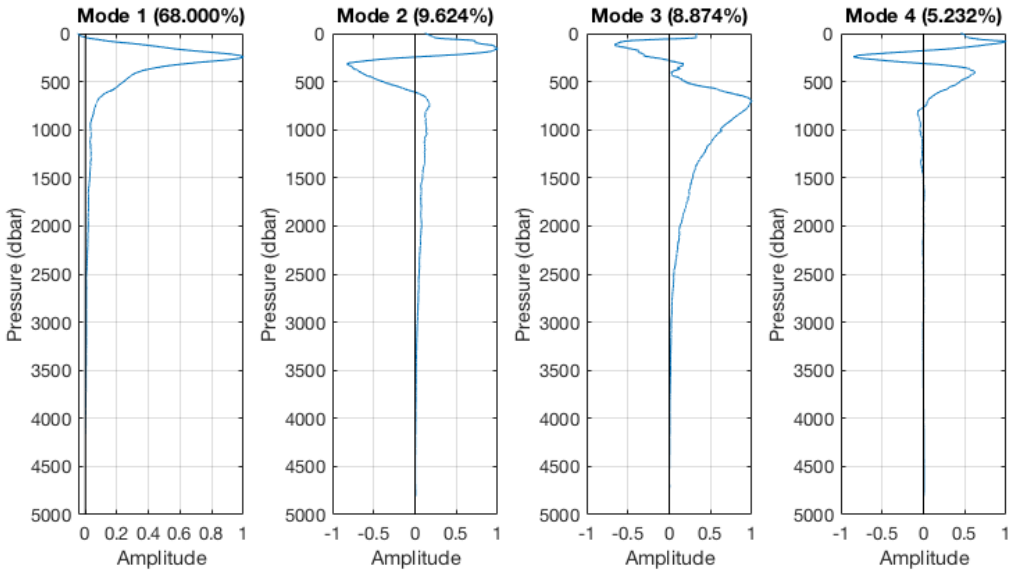

Figure 40. The first four EOF modes. They are normalized to have the amplitudes of 1. The singular values are scaled accordingly to represent the sound speed variance accounted by these modes. They together account for 92.72 % of the sound speed perturbation variance.

For the horizontal basis function, the ocean domain was divided into pixels by zonal and meridional lines of longitude and latitude. $\mathrm{E}_i(x, y)$ then has a unit value in pixel *i* defined by $x_{i-1} < x < x_i$ and $y_{i-1} < y < y_i$ and zero elsewhere. $\mathrm{E}_i(x, y)$ does not have an explicit functional form but was reflected in the model through the way the integration in **Equation 24** was implemented in the discrete computational model and how the model vector was structured.

As part of the process of determining the empirical orthogonal function representation for on the vertical sound speed perturbation structure (from the historical CTD data), we obtained the a priori uncertainties of each vertical mode. In the case of the horizontal uncertainty, we assume that the sound speed perturbation generation process has a Gaussian nature. To determine the spatial covariance among the values in the computational domain, a Gaussian covariance function was used to be a priori model uncertainty which is in the form of

$$P\left(\underline{\mathrm{X}}_k, \underline{\mathrm{X}}_l\right) = \Delta c^2 \exp\left(-\frac{||\underline{\mathrm{X}}_k - \underline{\mathrm{X}}_l||^2}{L^2}\right) \tag{26}$$

where $\underline{\mathrm{X}}_k$ is a position vector representing horizontal Cartesian coordinates of the middle point of pixel *k* in the domain, Δc^2 is the a priori sound speed variance computed from the EOF analysis (squared singular values), and *L* is the Gaussian covariance length in km. $||\underline{\mathrm{X}}_k - \underline{\mathrm{X}}_l||$ represents the ellipsoidal distance between pixel *k* and pixel *l* in km.

The a priori model uncertainty matrix or a priori model covariance matrix of the ocean sound speed can be formed as

$$\mathbf{P} = \langle \mathbf{m}\mathbf{m}^T \rangle = \begin{bmatrix} \Delta c^2 \exp\left(-\frac{||\underline{\mathrm{X}}_1 - \underline{\mathrm{X}}_1||^2}{L^2}\right) & \cdots & \Delta c^2 \exp\left(-\frac{||\underline{\mathrm{X}}_1 - \underline{\mathrm{X}}_N||^2}{L^2}\right) \\ \vdots & \ddots & \vdots \\ \Delta c^2 \exp\left(-\frac{||\underline{\mathrm{X}}_N - \underline{\mathrm{X}}_1||^2}{L^2}\right) & \cdots & \Delta c^2 \exp\left(-\frac{||\underline{\mathrm{X}}_N - \underline{\mathrm{X}}_N||^2}{L^2}\right) \end{bmatrix} \tag{27}$$

Since we introduced four EOF modes to the ocean model, each EOF mode had separate observation matrix, model vector, and a priori covariance matrix. From **Equation 23** and **Equation 25**, the observation matrix and the model vector of the ocean perturbation could be expressed in explicit matrix form as

$$\mathbf{G}_m = [\,\mathbf{G}_{\boldsymbol{mode1}}\,\mathbf{G}_{\boldsymbol{mode2}}\,\mathbf{G}_{\boldsymbol{mode3}}\,\mathbf{G}_{\boldsymbol{mode4}}\,] \tag{28}$$

$$\boldsymbol{m}_m = [\,\boldsymbol{m}_{\boldsymbol{mode1}}\,\boldsymbol{m}_{\boldsymbol{mode2}}\;\boldsymbol{m}_{\boldsymbol{mode3}}\;\boldsymbol{m}_{\boldsymbol{mode4}}]^{\boldsymbol{T}} \tag{29}$$

$$\mathbf{P}_{\boldsymbol{m}} = \begin{bmatrix} P_{mode1} & 0 & 0 & 0 \\ 0 & P_{mode2} & 0 & 0 \\ 0 & 0 & P_{mode3} & 0 \\ 0 & 0 & 0 & P_{mode4} \end{bmatrix} \tag{30}$$

Since the EOF modes are orthogonal to one another, there is no covariance between modes.

The observation matrix **G** for the hydrophone position offsets can be viewed as a mapping matrix which relates the position offsets to the travel time perturbation (in an unperturbed ocean). To eliminate ambiguity between the hydrophone position offsets and the shipboard transducer position offset, we assumed that the transducer position uncertainties are much less than the hydrophone. The sensitivity of the travel time perturbation to the hydrophone position offsets in 3 directions can be derived from geometric relationships of a ray path *i* connecting the source and the receiver (Cornuelle, 1985) (Uffelen et al., 2016).

$$G_{i\,x} = \frac{cos_i(\emptyset)sin_i(\theta_r)}{c_r} \tag{31}$$

$$G_{i\,y} = \frac{sin_i(\emptyset)sin_i(\theta_r)}{c_r} \tag{32}$$

$$G_{i\,z} = \frac{cos_i(\theta_r)}{c_r} \tag{33}$$

where $\emptyset$ is an azimuthal angle of the acoustic source to the receiver with respect to east, θ_r is a received ray angle at the receiver with respect to the vertical, and c_r is sound speed at the receiver depth. The observation matrix for the hydrophone position offsets then can be written as

$$\mathbf{G}_p = [\,\mathbf{G}_{\boldsymbol{x}}\,\mathbf{G}_{\boldsymbol{y}}\,\mathbf{G}_{\boldsymbol{z}}\,] \tag{34}$$

The uncertainties of the hydrophone position in three directions are independent from one another. Thus, the associated position uncertainties (variances) can be expressed as

$$\mathbf{P}_p = \begin{bmatrix} (\Delta x)^2 & 0 & 0 \\ 0 & (\Delta y)^2 & 0 \\ 0 & 0 & (\Delta z)^2 \end{bmatrix} \quad \textbf{(35)}$$

where $\Delta x\ \Delta y\ \Delta z$ are RMS position errors which can be arbitrarily chosen (on a meter scale)

With all this established, a complete computational from **Equation 25** model including both ocean perturbation and hydrophone position offsets can be detailed as

$$\mathbf{d} = \begin{bmatrix} \Delta\tau_1 \\ \vdots \\ \Delta\tau_M \end{bmatrix}_{M\times 1}$$

$$\mathbf{G} = [\,\boldsymbol{G}_m\ \boldsymbol{G}_p]_{M\times(4N+3)}$$

$$\mathbf{m} = \begin{bmatrix} \boldsymbol{m}_m \\ \boldsymbol{m}_p \end{bmatrix}_{(4N+3)\times 1}$$

$$\mathbf{m}_p = \begin{bmatrix} x\ offset \\ y\ offset \\ z\ offset \end{bmatrix}_{3\times 1}$$

and the a priori covariance matrix

$$\mathbf{P} = \begin{bmatrix} \boldsymbol{P}_m & 0 \\ 0 & \boldsymbol{P}_p \end{bmatrix}_{(4N+3)\times(4N+3)}$$

Hereby, we employed the Gauss-Markov estimation theory to find a best estimate of the model vector. The objective function of this technique is

$$\mathrm{E} = \langle(\hat{\mathbf{m}} - \mathbf{m})(\hat{\mathbf{m}} - \mathbf{m})^T\rangle \quad \textbf{(36)}$$

The goal is to minimize the diagonal element of the objective function. This leads to a solution

$$\hat{\mathbf{m}} = \mathbf{G}^{-g}\mathbf{d} \quad \textbf{(37)}$$

where $\mathbf{G}^{-g}$ is called generalized inverse and defined by

$$\mathbf{G}^{-g} = \mathbf{P}\mathbf{G}^{-T}(\mathbf{G}\mathbf{P}\mathbf{G}^{T} + \mathbf{C}_d)^{-1} \quad \textbf{(38)}$$

where $\mathbf{C}_d$ is a measurement uncertainty matrix $\langle \mathbf{n}\mathbf{n}^T \rangle$. Since the noise is uncorrelated, $\mathbf{C}_d$ is a diagonal matrix (Tarantola, 1987).

The measurement uncertainties are a summation of the observational errors and the model representation errors. Two sources of the uncertainties were errors due to determining the peak arrival times from the complex envelope peak in the signal detection process (matched-filtering) and the transducer position inaccuracies which depend on the performance of the POS MV positioning system at a given time. The signal detection error is given by **Equation 54** (**Appendix B**). For the transducer position uncertainties, we can map position errors into travel time perturbation variances using the same approach as forming the observational matrix for the hydrophone position offsets

$$B_i{}^2 = \left(\frac{cos_i(\emptyset)sin_i(\theta_r)}{c_r}\right)^2 \Delta x^2 + \left(\frac{sin_i(\emptyset)sin_i(\theta_r)}{c_r}\right)^2 \Delta y^2 + \left(\frac{cos_i(\theta_r)}{c_r}\right)^2 \Delta z^2 \quad \textbf{(39)}$$

where Δx, Δy, Δz are transducer position errors from the POS MV

The quality of the solutions given by the model can be quantified by the posteriori uncertainty and resolution. After fitting data using the least-square criteria, the solution $\widehat{\mathbf{m}}$ should have lower uncertainty, which can be derived from the posteriori covariance matrix denoted by $\mathbf{P}_{\text{posteriori}} = < \widehat{\mathbf{m}}\widehat{\mathbf{m}}^{\,T} >$. The posteriori covariance matrix can be estimated by

$$\mathbf{P}_{\text{posteriori}} = (1 - \mathbf{G}^{-g}\mathbf{G})\mathbf{P}_{\text{priori}} \quad \textbf{(40)}$$

whose diagonal elements indicate variances of the solution and off-diagonal elements indicate covariances among the parameters.

The model resolution matrix **R** is another quantity used to determine "accuracy" of the obtained solution. In principal, we cannot see the real world as it is due to errors and uncertainties of the computational model and measurement uncertainties mentioned above. The model resolution matrix can be interpreted as a filter applied to the real world to give the observed parameters

$$\hat{\mathbf{m}} = \mathbf{R}\,\mathbf{m} \qquad (41)$$

R is defined by (Tarantola,1987)

$$\mathbf{R} = \mathbf{I} - \mathbf{P}_{\text{posteriori}}\,\mathbf{P}_{\text{priori}}{}^{-1}$$

or

$$\mathbf{R} = \mathbf{G}^{-g}\mathbf{G}$$

The diagonal elements of **R** are often used to visualize how the parameters **m** in the real world are mapped by our model to give the estimate $\hat{\mathbf{m}}$**.** Row or column *i* of **R** represents how a parameter m_i spreads out in space and affects other parameters. A value of 1 on the diagonal indicates that m_i is perfectly resolved by the inverse model.

Another assumption to be made to complete the inverse model is the correlation length *L.* This variable dictates an expected length scale of the ocean variability in the area. In other words, variabilities with length scales shorter than the correlation length scale will not be detected. In the case of Hawaiian waters, ocean variability of length scales of 170-220 km (Matthews et al 2011) is dominant. These length scales are large compared to the size of the area in this study (~50 km). Determining an optimal correlation scale is impossible without a priori knowledge of the local ocean process at the scale of interest. Since the sampled area in this study has a length scale of 50 km, the model should be able to reveal ocean variabilities of the scale of 20 km, which is about half of the area diameter. Therefore, in this analysis, the correlation length scale was picked to be 20 km.

Simulations

Simulations were conducted to test the performance of the model. A computational domain was set up to have a size of 120 km by 120 km with 25 x 25 gridding, resulting in a pixel size of 4.8 km by 4.8 km. For the sampling, acoustic transmissions were set to be made on circumferences of five circles with radii of 26 km, 20 km, 15 km, 10 km, and 5km. The transmissions points were equally spaced by 500 m (circumferential distance). This way of setting up transmissions resulted in a total transmission number of 952 and a very dense ray path pattern. The measurement uncertainty $\mathbf{C}_{\boldsymbol{d}}$ was set to be 0.2 ms rms for all rays.

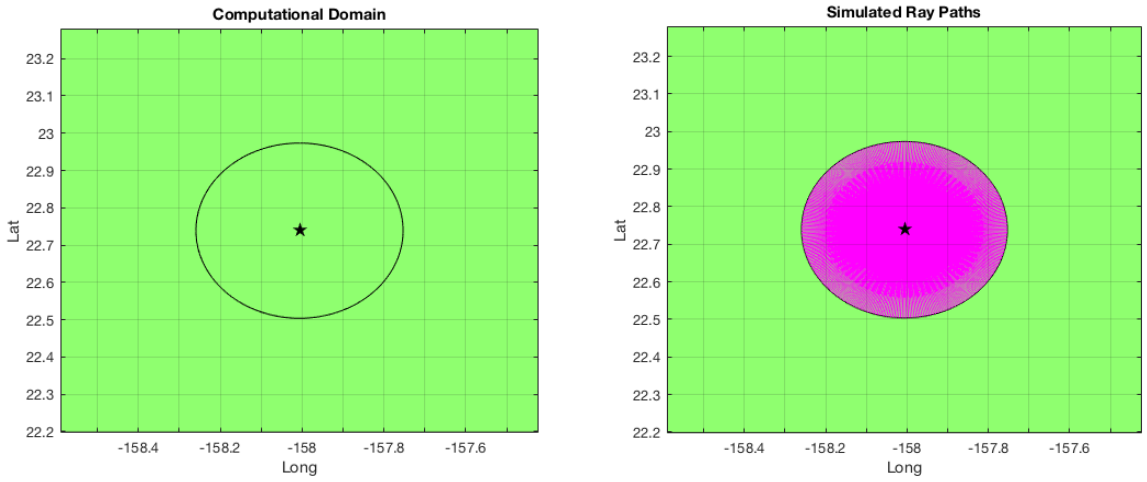

Figure 41. (a) 120 x 120 km computational domain with 25x25 gridding. The star marker indicates the ACO location (b) Simulated ray paths (magenta).

After setting up the sampling, the sensitivity of each ray path could be computed. **Figure 42** shows the sensitivity of the ray paths. The ray paths were categorized by the number of pixels the rays cross to reach the hydrophone from the transmission points (effectively radial distance here). The result showed that the ray travel time became more sensitive to sound speed perturbations when the ray path was longer, and it was most sensitive to mode 3, and second-most sensitive to mode 1. This is explained by the deepest vertical extension of the mode 3 which outweighs its negative values in shallow layers.

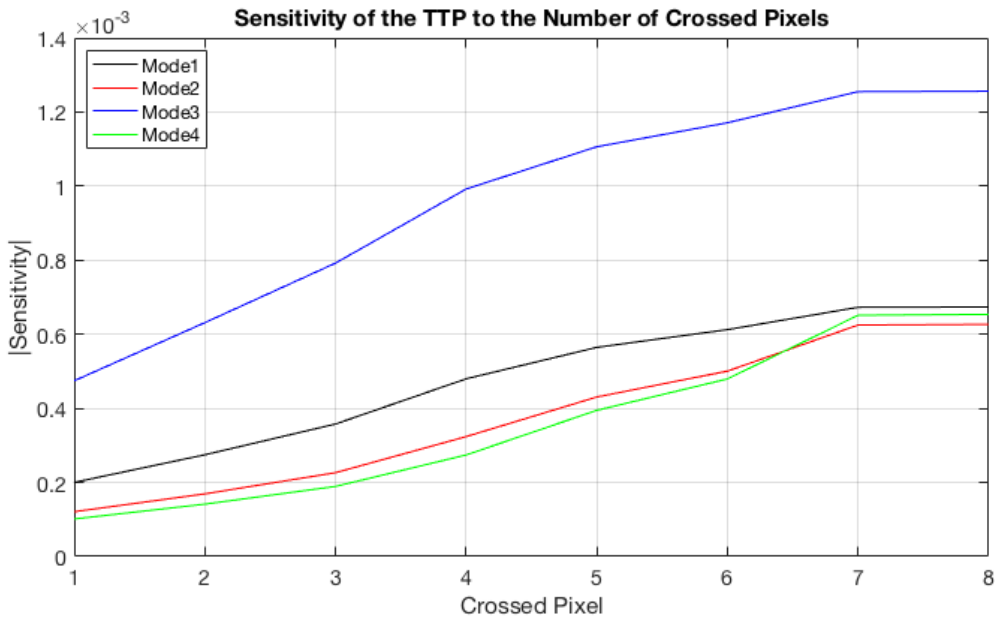

Figure 42. Sensitivity of the ray travel time perturbation versus the number of pixels the ray has to cross to reach the receiver.

In the first test case, the ideal ocean sound speed perturbation was set to be a Gaussian function with a correlation length of 20 km with the center located at the middle point of the radius angled 45 degrees east to the north (**Figure 43**). The maximum sound speed perturbations of the EOF modes were 4 m/s, 3m/s, 2m/s, and 1 m/s respectively. Using **Equation 37**, sound speed perturbation fields of the four EOF modes were recovered (**Figure 44**).

The differences between the ideal and the recovered are shown in **Figure 45. Figure 46** shows the percentage of the model uncertainty reduction given by

$$RMS\ Error\ Reduction = \frac{Posterior\ Standard\ Deviation}{Prior\ Standard\ Deviation} \times 100\% \qquad \textbf{(42)}$$

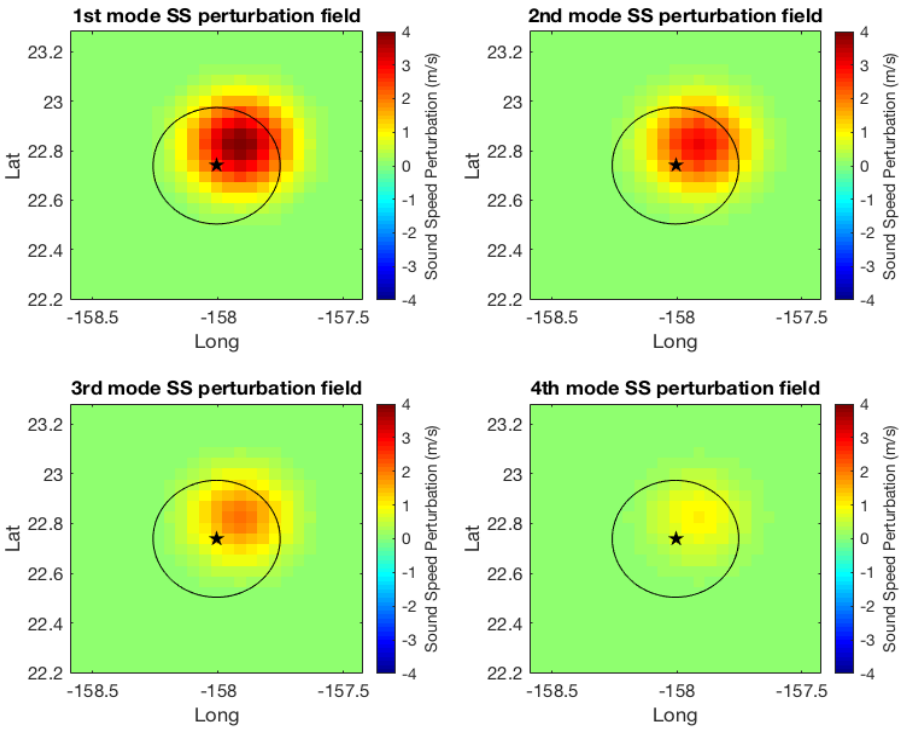

Figure 43. The ideal sound speed perturbation fields of the first test case. The perturbations are set to be at the middle point of the radius angled at 45 degrees east to the north of the and described by the Gaussian function with the correlation length of 20 km.

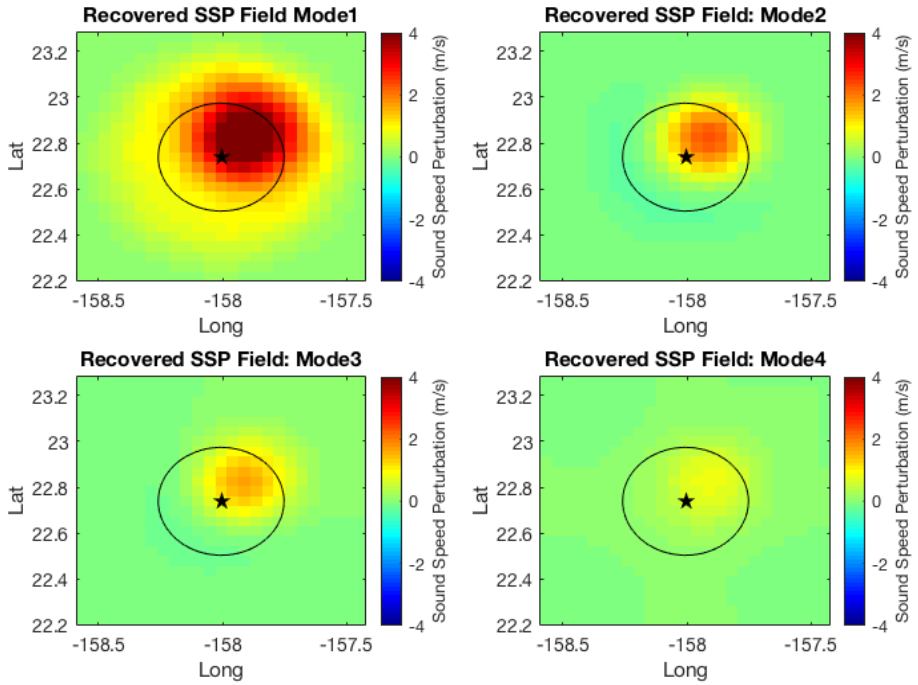

Figure 44. The recovered sound speed perturbation fields for the first test case.

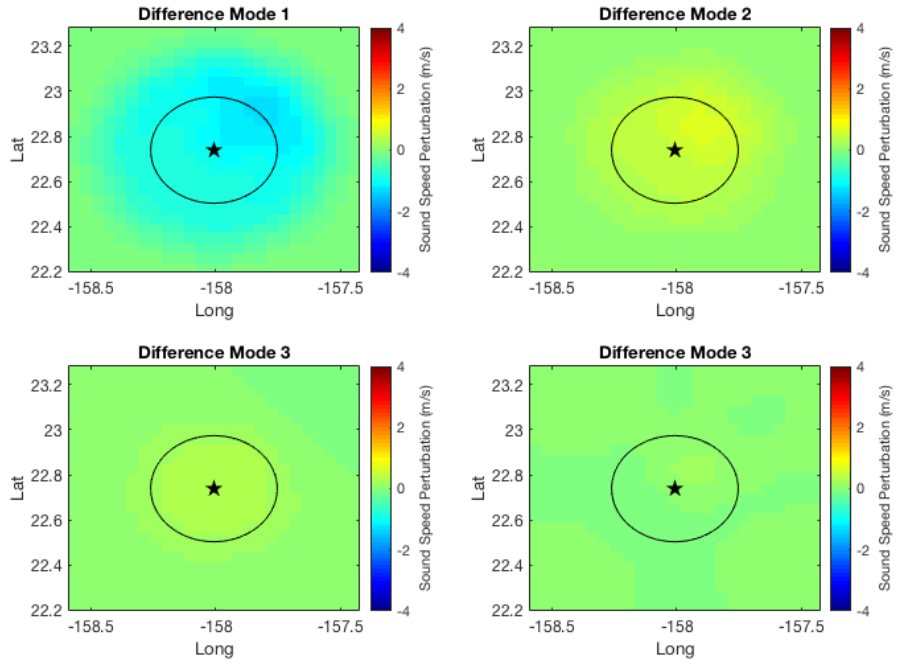

Figure 45. The differences between the ideal and the recovered sound speed perturbation fields for the first test case.

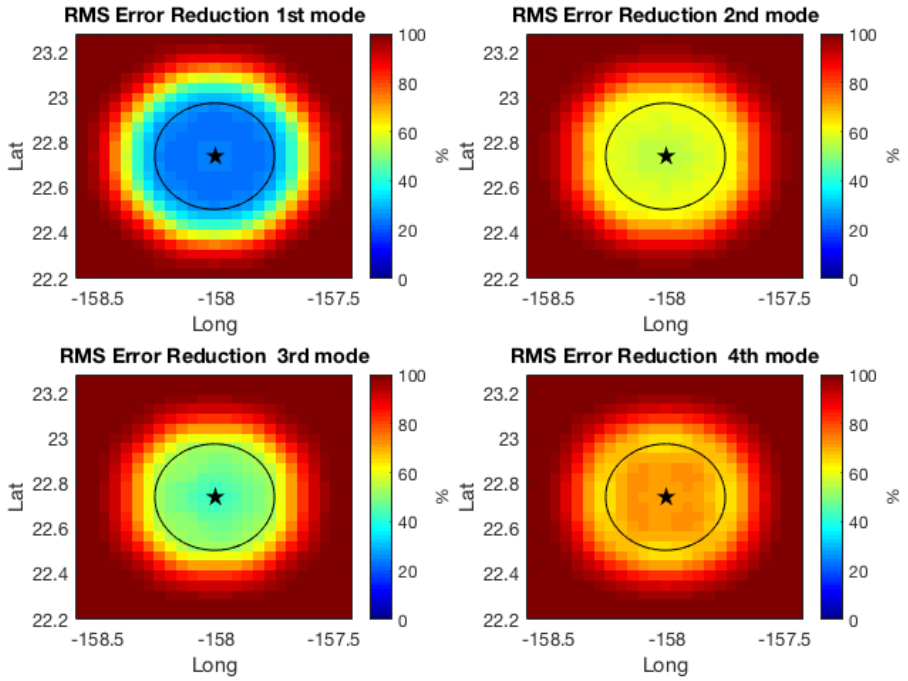

Figure 46. The RMS error reduction percentage of the solution in the first test case. Mode 1 has its uncertainty reduced down to 20% of the a priori uncertainty while mode 3 error reduces to 50%. Mode 2 and mode 4 have quite high errors larger than 50% of the a priori errors.

The model resolved the data and reduces uncertainties well inside the circle where data was present. Mode 1 and mode 3 were best and second-best resolved with minimum RMS error reduction of 30% and 45 % respectively. Mode 2 and mode 4 were poorly resolved. The diagonal elements of the model resolution are shown in **Figure 47**.

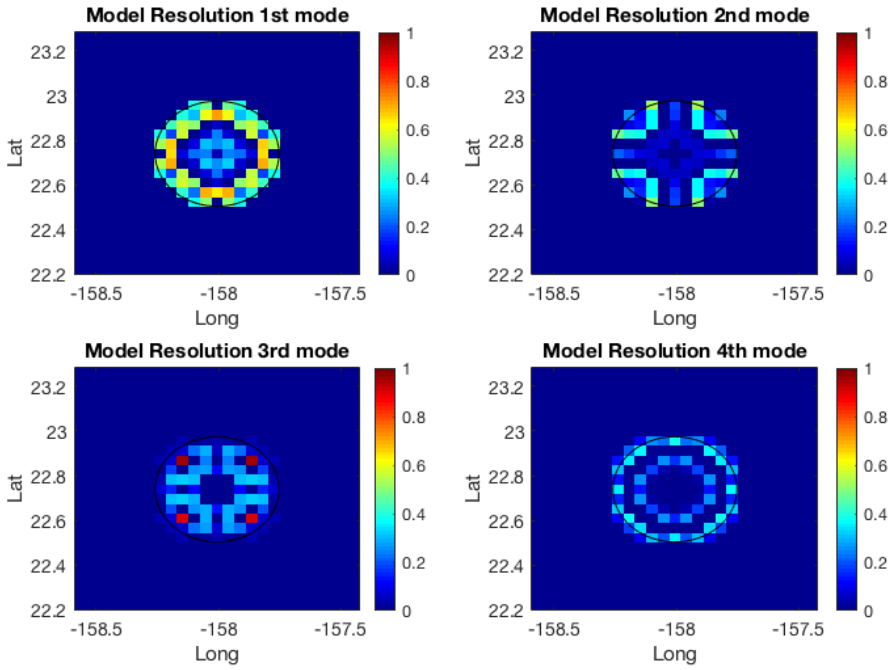

Figure 47. Model resolution for the first test case.

Due to the way the ray sampled the ocean, we did not obtain much vertical resolution from the modal structures with fluctuating profiles in shallow layers. Additionally, the fluctuating profiles of mode 2, mode 4 caused the integrand of **Equation 24** to cancel out when integrated along a ray path, resulting in near-zero sensitivities in some pixels (**Figure 48**). These two attributes caused ambiguity to the vertical resolution of the modal structure (need multiple crossing ray paths in the vertical to resolve).

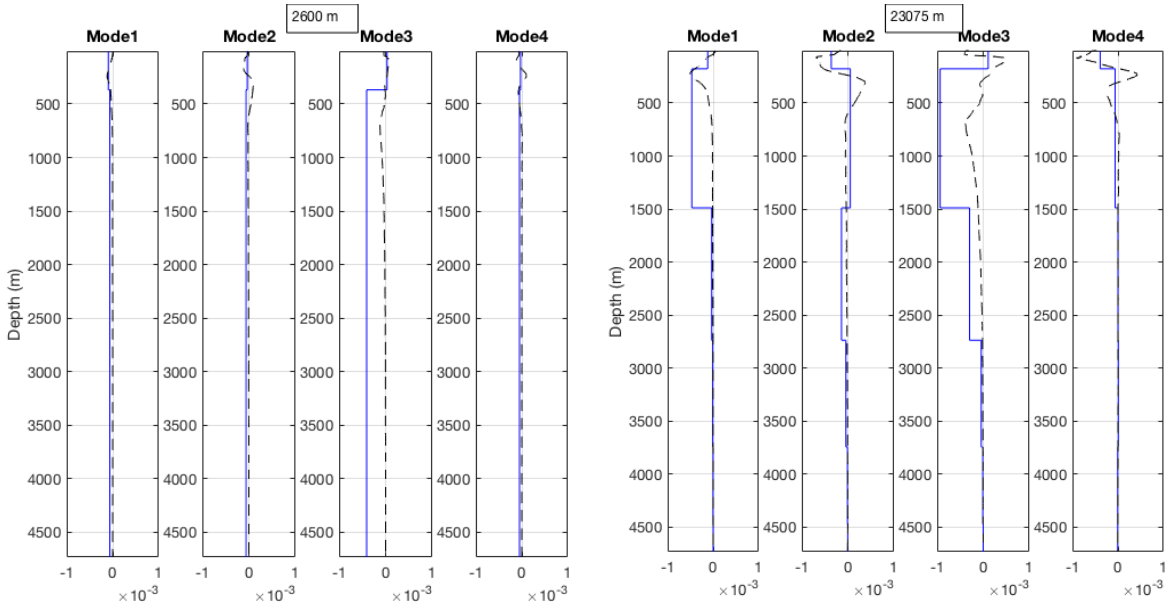

Figure 48. The sensitivity *G* of a ray path in each pixel at different ranges. Left, a ray is transmitted at a surface range of 2,600 m and crosses 2 pixels; the total ray sensitivities of mode 2 and mode 4 are near-zero. Right, a ray is transmitted at the RAP limiting range; modes 1 and 3 have significant sensitivities while the sensitivities of mode 2 and mode 4 are still near-zero.

To improve the overall solution's accuracy, integrating over the depth dependence of the sound speed would help reduce the ambiguity. Thus, instead of representing the solutions in separate EOF modes, combining the four modes together and representing depth-averaged sound speed perturbations would help improve the solution's accuracy. To proceed, an operator which combines and depth-averages the empirical modes needs to be defined. An alternative way to manipulate the sound speed perturbation representation in **Equation 21** was to represent the sound speed perturbation profile in pixel *i* as a sum of all vertical basis functions with corresponding amplitudes (Wunsch, 2006)

$$\mathbf{m}_i(z) = [\vec{v}_1(z) \quad \vec{v}_2(z) \quad \vec{v}_3(z) \quad \vec{v}_4(z)\,] \begin{bmatrix} m_{i1} \\ m_{i2} \\ m_{i3} \\ m_{i4} \end{bmatrix} \tag{43}$$

Equation 43 can be averaged along the vertical by integrating both sides of the equation

$$\bar{\mathbf{m}}_{\boldsymbol{i}} = [\bar{v}_1 \quad \bar{v}_2 \quad \bar{v}_3 \quad \bar{v}_4\,] \begin{bmatrix} m_{i1} \\ m_{i2} \\ m_{i3} \\ m_{i4} \end{bmatrix} \tag{44}$$

where

$$\bar{v}_j = \int_0^H \vec{v}_j(z)\, dz$$

From the separate-mode solution obtained previously, a linear system is created to calculate for the depth-averaged solution while preserving the dimensions of $\mathbf{m}_{\boldsymbol{m}}$.

$$\bar{\mathbf{m}} = \bar{\mathbf{V}}\mathbf{m}_{\boldsymbol{m}} \tag{45}$$

where $\bar{\mathbf{m}}$ is a M×1 matrix containing the depth-averaged sound speed perturbation of combined EOF modes, $\bar{\mathbf{V}}$ is a depth-averaging and mode-combining operator defined as

$$\bar{\mathbf{V}} = [\bar{v}_1\mathbf{I}_{\boldsymbol{M\times M}} \quad \bar{v}_2\mathbf{I}_{\boldsymbol{M\times M}} \quad \bar{v}_3\mathbf{I}_{\boldsymbol{M\times M}} \quad \bar{v}_4\mathbf{I}_{\boldsymbol{M\times M}}]_{M\times(4\cdot M)} \tag{46}$$

and the associated uncertainty can be computed by

$$\mathbf{P}_{posteriori} = <\bar{\mathbf{m}}\bar{\mathbf{m}}^{\boldsymbol{T}}> = \bar{\mathbf{V}} < \mathbf{m}_{\boldsymbol{m}}\mathbf{m}_{\boldsymbol{m}}{}^{\boldsymbol{T}} > \bar{\mathbf{V}}^{\mathbf{T}} \tag{47}$$

The depth-averaged values of the ocean sound speed perturbation and the solution in the first test case are shown in **Figure 49**, with the corresponding RMS error reduction percentage, and the model resolution matrix (**Figure 50 and 51**).

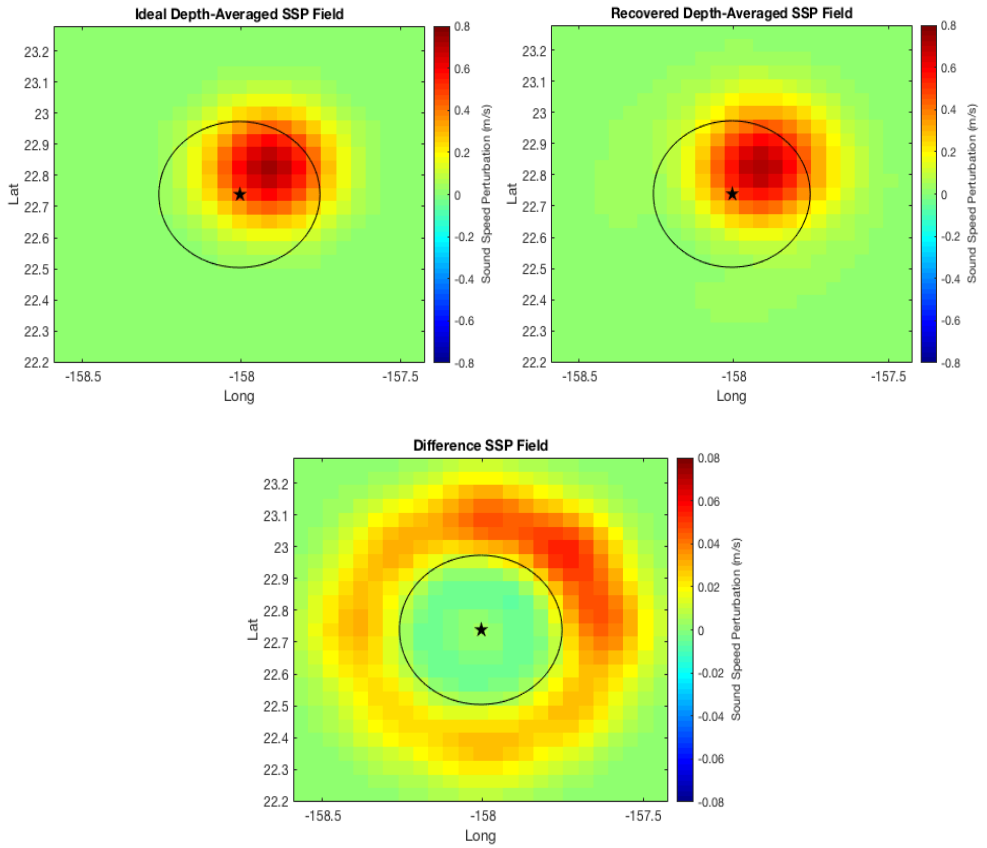

Figure 49. The result of depth-averaged model. Top-left, the depth-averaged ideal ocean sound speed perturbation field. Top- right, the recovered sound speed perturbation field. Bottom, the difference between the ideal and the recovered (the color scale is a tenth of the scales of the sound speed perturbation fields)

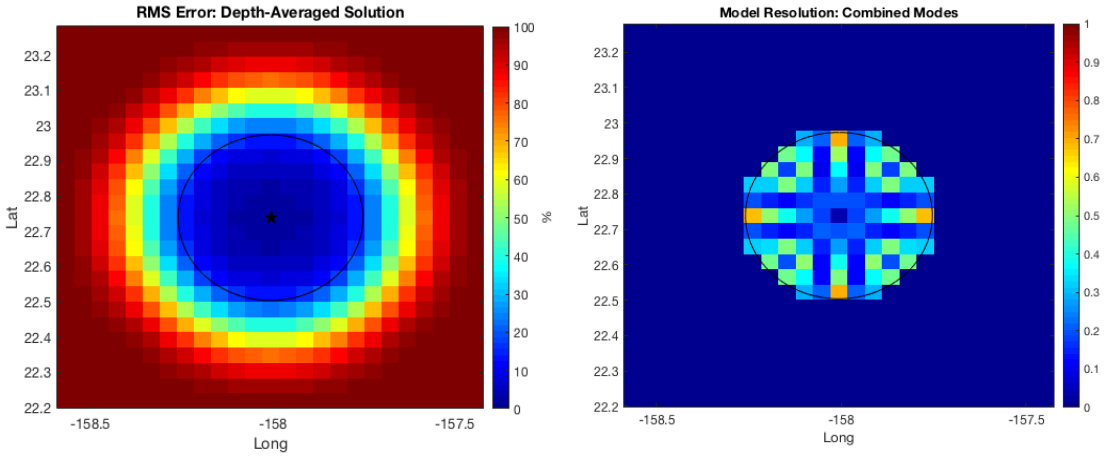

Figure 50. Left, Depth-averaged RMS error reduction. **Figure 51.** Right, The resolution of the depth-averaged solution.

When the sound speed perturbation was depth-averaged, the difference between the ideal and the recovered sound speed perturbation fields inside the circle reduced significantly. The difference plot seems to have large values outside the circle, but these values are small when compared to posterior model errors (**Figure 52**). The RMS error reduction of inner pixels went down to around 2%. Compared to **Figure 46**, the depth-averaged solution uncertainty was improved measurably. Considering the resolution pattern, it was a combination of the resolutions of the four modes. The depth-averaged solution resolution inherited an annular pattern from mode 1's resolution with a more-distinct N-S/E-W radial pattern from mode 2 and mode 4 resolutions. In summary, the depth-averaged, mode-combined representation of the sound speed perturbation yielded a better result, and it would be applied to the real data.

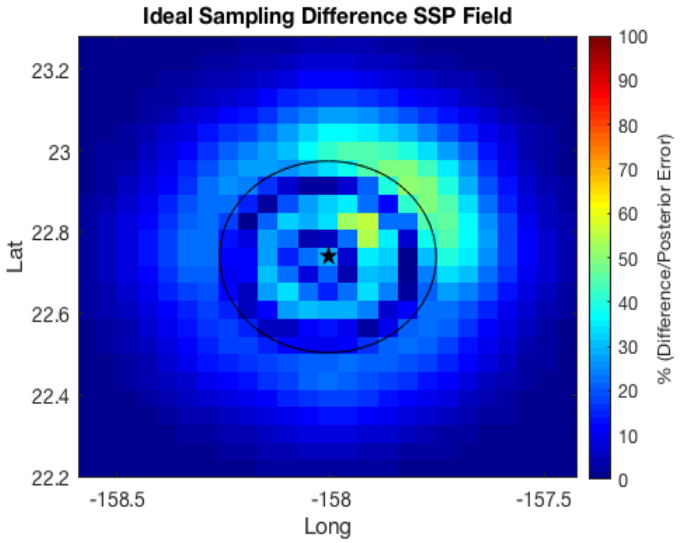

Figure 52. Percentage of the difference relative to the posterior error. The red zone outside the circle in **Figure 49** is considered only 50 percent of the posterior error, which is within one error bar.

The second test case had a delta function of the ocean perturbation at a random pixel. This was to test how the model with a Gaussian function as a priori covariance would respond to small scale features with extreme values compared to the surrounding. **Figure 53** shows the ideal sound speed perturbation field and the solution.

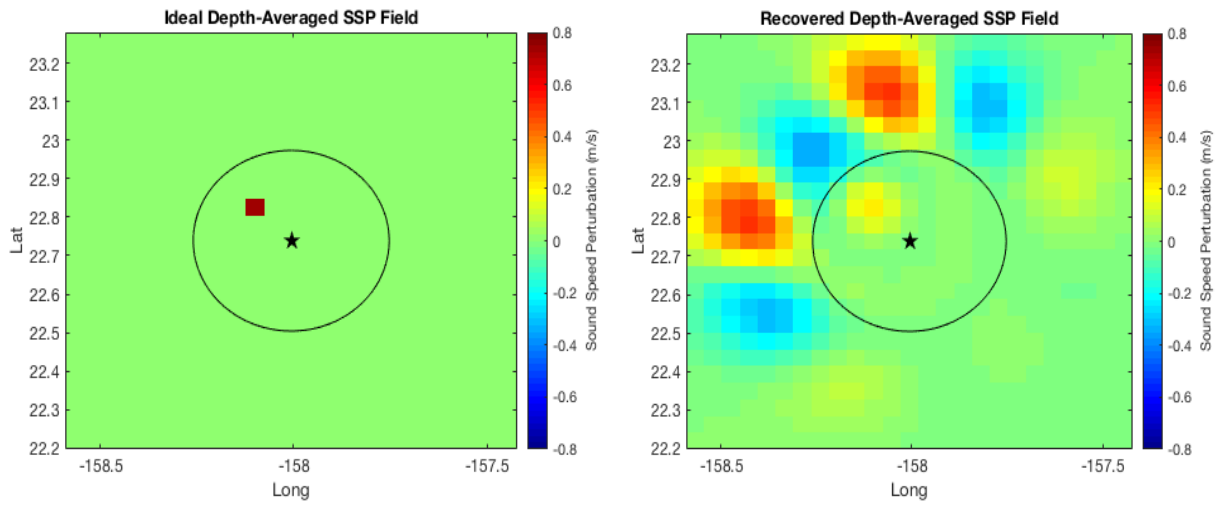

Figure 53. Impulse response test case. Left, the ideal ocean sound speed perturbation field. Right, the recovered sound speed perturbation field

The impulse response contained sidelobes outside the circle. Since the model tried to fit the data in a least-squares sense, and the rest of the pixels inside the circle were unperturbed, all the data forced the model to resolve the sharp peak by dissipating the energy of the excited pixel to the area outside the circle. This created artificial features of sidelobes outside the sampled area. As a result, if the measurements contain highly-contrast ocean variability with a length scale shorter than the a priori correlation length scale (which appears to be the case, according to **Figure 38**), the inverse will have artifacts of energy leaking outside the sampled area. To handle this issue, averaging the measurements to suppress large spatial swings was employed. A Gaussian function with 20-km correlation length was selected to be the spatial filter for this purpose in order to be consistent with the assumptions for the ocean model. **Equation 48** expresses mathematical implementation of this process

$$\tilde{d}_k = \frac{\sum_{i=1}^{M} w_i d_i}{\sum_{i=1}^{M} w_i} \tag{48}$$

where

$$w_k = \exp\left(-\frac{||\underline{X}_{d_i} - \underline{X}_{d_k}||^2}{20\ \text{km}}\right)$$

It can be written in a matrix form as

$$\tilde{\mathbf{d}} = (\mathbf{W}\mathbf{d}) \tag{49}$$

in which $\tilde{\mathbf{d}}$ is the averaged measurement vector, and **W** is the averaging matrix (filter)

The last simulation was conducted to test the inverse model with the correlation length of 20 km on a random sound speed perturbation field. A simulated perturbed ocean was constructed based on prescribed covariance with a correlation length of 20 km using Cholesky decomposition (Tarantola, 1987). **Figure 54** shows the ideal sound speed perturbation field of this simulation.

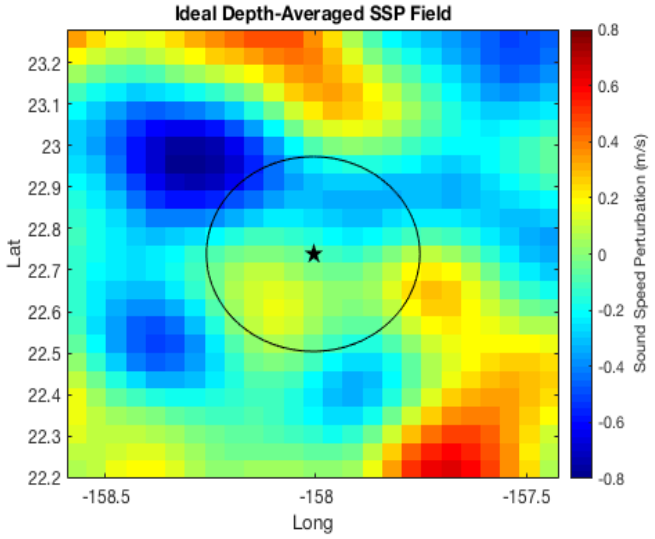

Figure 54. The ideal sound speed perturbation field with 20-km correlation length.

In this case, the actual HEM and the icListen sampling with associated measurement uncertainties were also used to construct the recovered sound speed perturbation fields in order to compare with the ideal sampling case. **Figure 55** shows the sampling ray paths of the HEM and the icListen.

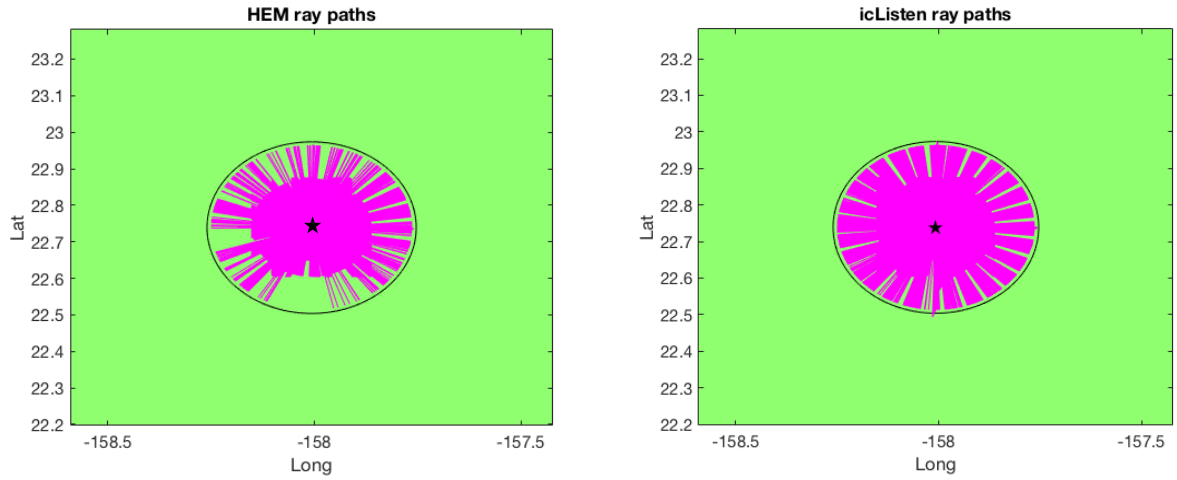

Figure 55. Actual samplings of both hydrophones. Left, the HEM. Right, the icListen

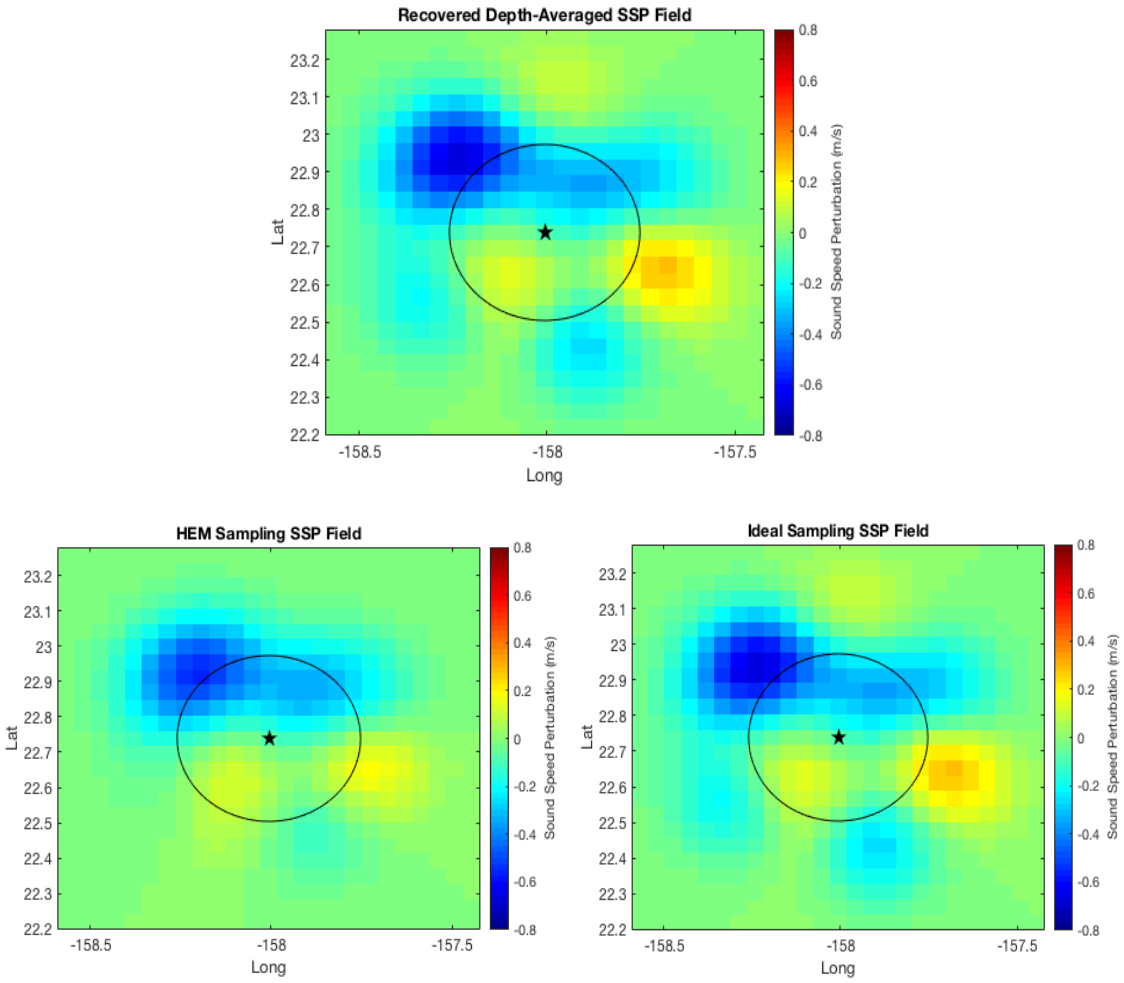

Figure 56. The sound speed perturbation field solution of three samplings. Top, the ideal sampling. Bottom-left, the HEM sampling. Bottom-right, the HEM sampling. (All plots with the same color scale)

As the icListen sampling was more complete than the HEM's, the icListen inverse solution was more similar to the ideal sampling's solution (**Figure 56**). In three cases, a cold eddy in the north and a warm eddy on the west were partially recovered by the model extrapolating the present data points near the limiting range of the circle using the a priori covariance function. The sound speed perturbations outside the circle die down after one correlation length scale. **Figure 5**7 shows the differences between the recovered sound speed perturbation fields and the ideal.

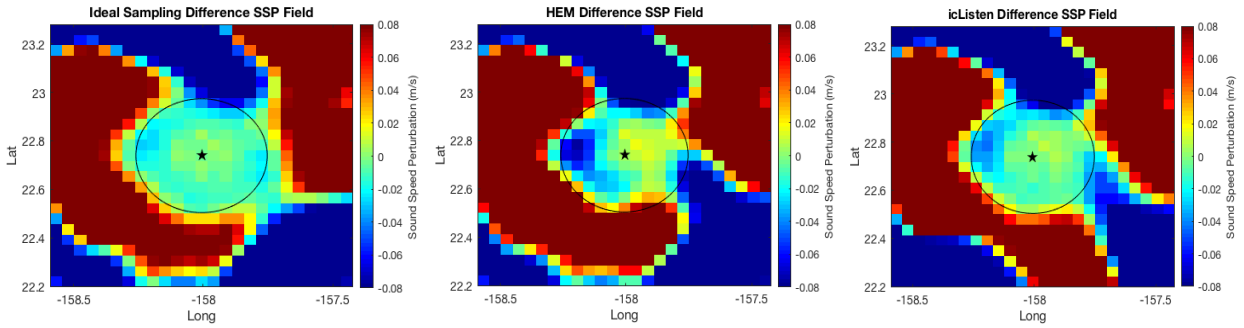

Figure 57. Sound speed perturbation differences (all color scales range from -0.08 to 0.08 m/s).

If ignoring values outside the circles, the results showed that the western sector of the sampled area had sound speed perturbation field discrepancies larger than other part. This was caused by the fluctuating pattern of ocean variability with large perturbation magnitudes which happened to be situated on the west. In overall, the icListen solution is more accurate than the HEM due to the larger number of data points and lower measurement uncertainty. The results in this chapter are a tool to interpret the credibility of the inverse solutions which will be derived from the real datasets from the field experiment in the next chapter.

9. Sound Speed Perturbation Inversion

In this chapter, the actual datasets collected in October 2018 will be used to solve for sound speed perturbation fields using the inverse methods presented in **Chapter 8**. The solutions and their performances will be discussed.

With the inverse model established, we can solve for the sound speed perturbation fields and the hydrophones position offsets simultaneously from the travel time perturbations shown in **Figure 39**. **Figures 58** and **Table 5** show the inverse sound speed perturbation fields and the hydrophone position offsets. The size of the ocean domain was 120 km by 120 km with 25 by 25 gridding. Each pixel has a size of 4.8 km by 4.8 km.

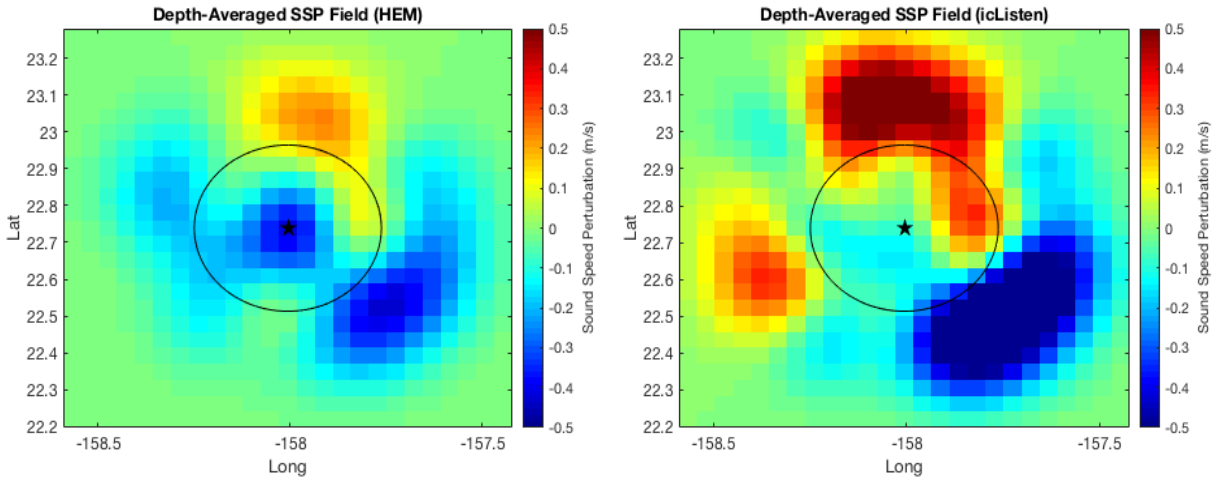

Figure 58. Inverse sound speed perturbation fields from the HEM hydrophone data (left) and the icListen data (right).

Hydrophone	Original Position	X offset (m)	Y offset (m)	Z offset (m)
HEM	Lon: 22.73877 Lat: -158.00619 Depth: -4733.911 m	1.21 ± 0.31	-0.78 ± 0.3	-1.06 ± 0.33
icListen	Lon: 22.73912 Lat: 158.00611 Depth: - 4727.60 m	-0.01 ± 0.23	-1.12 ± 0.24	4.92 ± 0.22

Table 5. Hydrophone position offsets

As discussed in the previous chapter, large perturbations outside the circles and small features of alternating sound speed fields were generated by the attempt of the inverse model trying to fit spatially-unsmooth measurements together. Considering the travel time perturbation fields constructed based on only ocean perturbations (hydrophone position offsets excluded) (**Figure 59**), on the circumferences of the 25-km circles of both hydrophones, the travel time perturbations change drastically when moving azimuthally. These small-scale spatial changes are the root cause of energy leakage outside the 25-km circles. To resolve this issue, filtering the measurements to eliminate these fluctuations would help improve the solutions. In principle, the filtering should be done on the original measurements which contain information about the ocean perturbation and the hydrophone position offsets. The filtered measurements then will be used to solve for the sound speed perturbations and the hydrophone position offsets will be treated as measurement uncertainties and incorporated into $\mathbf{C}_d$ matrix. However, as a demonstration of how the filtering would impact the solutions, the travel time perturbation constructed from ocean perturbations (hydrophone position offsets excluded) will be spatially averaged to obtain smoother measurements using **Equation 49**. The filtered (averaged) travel time perturbations are shown in **Figure 60**.

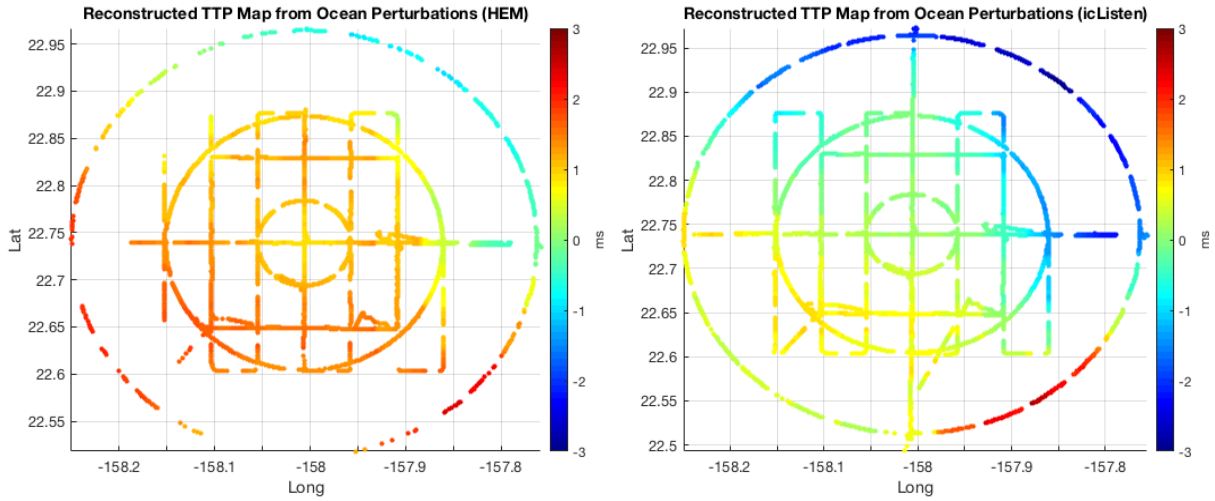

Figure 59. Reconstructed travel time perturbation maps. Left, the HEM hydrophone. Right, the icListen hydrophone.

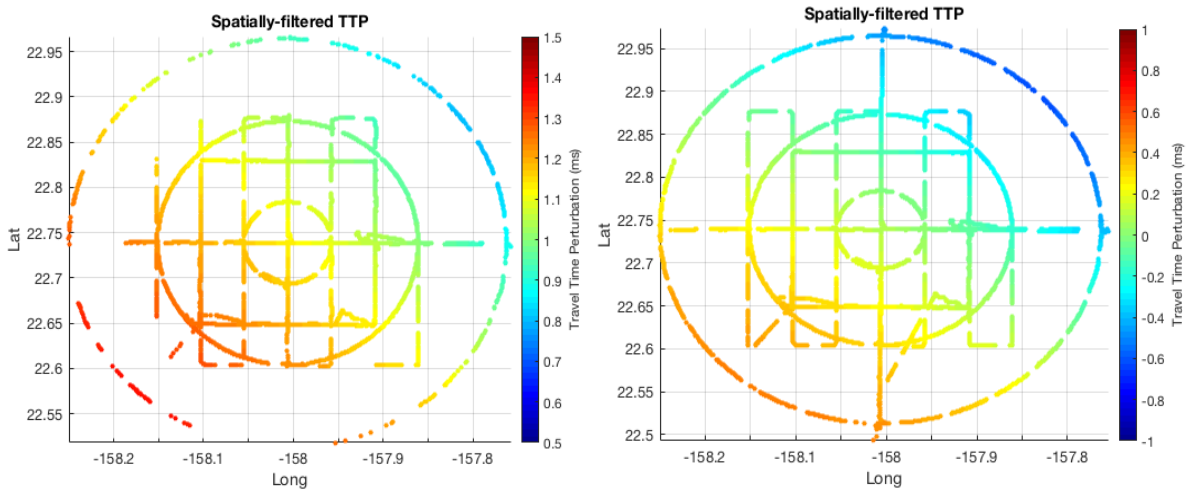

Figure 60. Spatially filtered travel time perturbation maps from **Figure 59**. Left, the HEM hydrophone. Right, the icListen hydrophone. The color scale of the HEM data ranges from 0.5 to 1.5 ms while that of the icListen ranges from -1 to 1 ms.

Overall, the HEM hydrophone' travel time perturbations were all positive with a peak-to-peak value of 0.5 ms while those of the icListen hydrophone were symmetric about 0 and had a peak-to-peak value of 1 ms. The patterns of the travel time perturbation maps from both hydrophones were closely related, having the magnitudes increasing toward the southwest. The inverse sound speed perturbation fields computed from this data are shown in **Figure 61**.

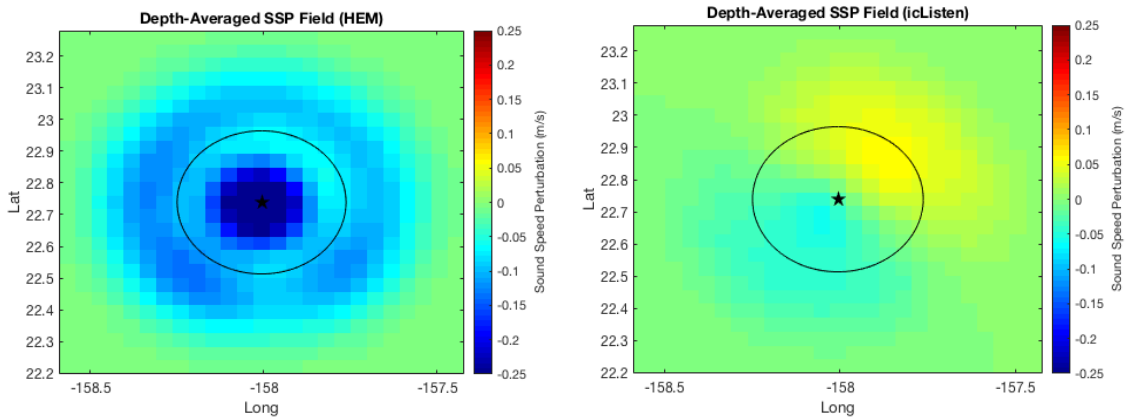

Figure 61. Sound speed perturbation fields from filtered measurements. Left, the HEM data. Right, the icListen data. Both plots are on the same color scale.

Unlike the inverse solutions in **Figure 58**, these solutions did not have small sidelobes outside the sampling area. The HEM solution suggested that there was colder water dominating while

the icListen had both cold water and warm water zones. Since small scale variabilities were filtered out, the length scale of the ocean features from the icListen solution agreed better with the a priori correlation length of 20 km.

Next, when the real data sets were used to form the observation matrices **G**, the RMS error reductions and resolutions of the inverse solutions become

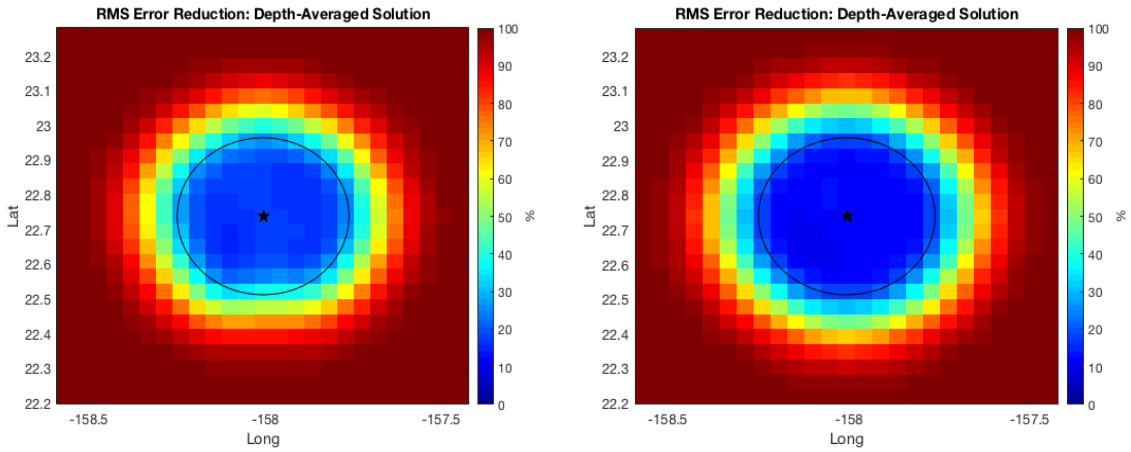

Figure 62. RMS error reduction percentage of the HEM hydrophone (left) and the icListen (right) inverse solutions.

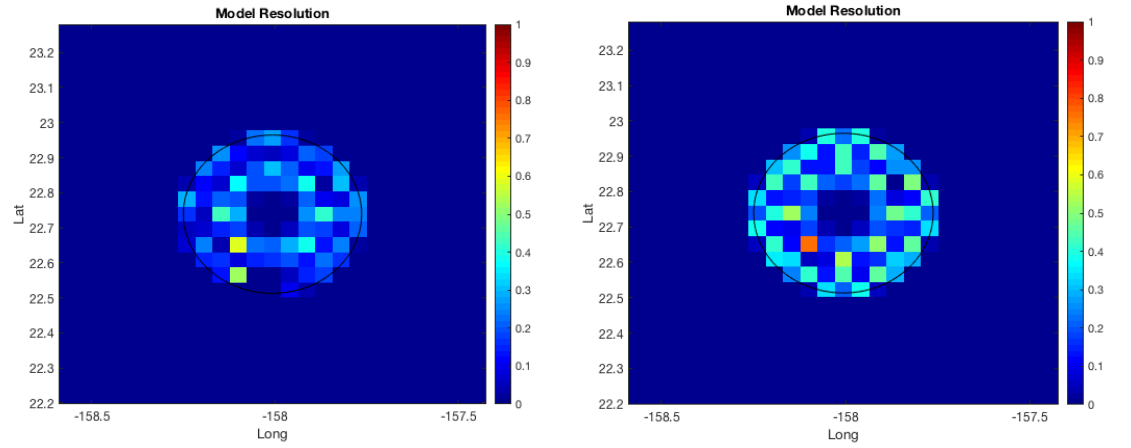

Figure 63. Model resolutions of the HEM hydrophone (left) and the icListen (right) inverse solutions.

As expected, the patterns of the RMS error reduction and the resolution of the icListen solution were better and more azimuthally symmetric because of more usable measurements of the icListen

data. The individual pixel was not expected to have high resolution since the a priori correlation length (20 km) was much larger than the length scale of the pixels (4.8 km).

Another metric to evaluate the solution quality is the normalized residual. It looks at how well the model can reduce the variation among the measurements. If the model can handle the data well, it should reduce the ratio of the misfit between the measurements and the estimated measurements constructed from the solution to the travel time perturbation uncertainties. Thus, ideally, this quantity should be close to 1.

$$normalized\ residual = \frac{\mathbf{d}\text{-}\mathbf{G}\widehat{\mathbf{m}}}{\sqrt{diag(\mathbf{C}_\mathrm{d})}} \tag{50}$$

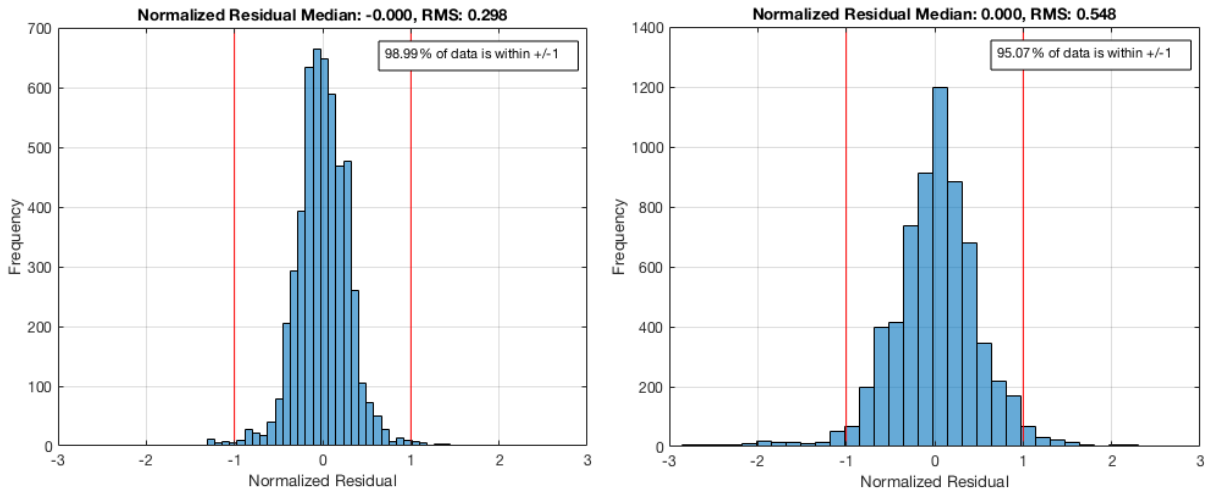

Figure 64. Histograms of normalized residuals. Left, 98.99% of the HEM hydrophone data residual lies within +/- 1 range. Right, 95.07 % of the icListen hydrophone data residual lies within +/- 1 range.

From these metrics, the computational model was verified to be sufficient to solve for the sound speed perturbation fields given a set of travel time perturbation measurements and ray paths. Another set of sound speed perturbation fields computed using a CTD cast on 16th November 2018 (the next month from the experiment date) was calculated to compare with the maps above. The ocean in November 2018 was warmer than October 2018 (**Figure 65**). The differences of the sound speed perturbation fields between two solutions (November minus October) are shown in **Figure 66**.

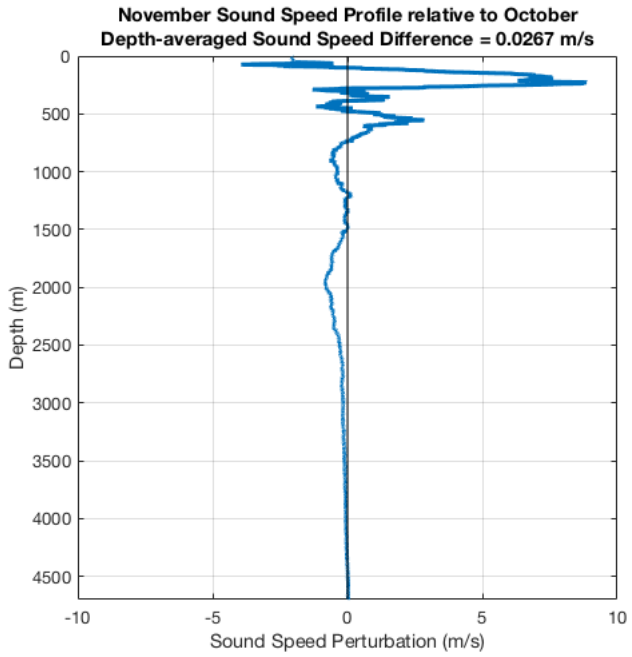

Figure 65. Sound Speed Profile from the November 2018 CTD cast relative to the October 2018 CTD cast.

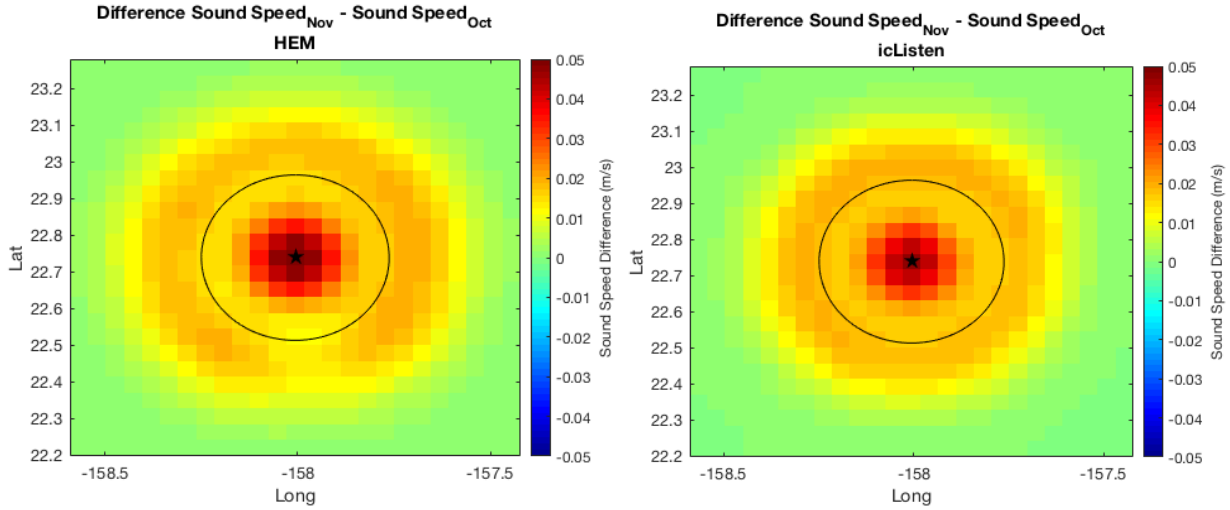

Figure 66. Depth-averaged sound speed difference between November and October retrieved from the inverse.

When the reference ocean state was changed, the inverse responded to that change. The sound speed in overall were higher, reflecting warmer ocean. This simulation gives another piece of evidence to support functionality of the inverse model.

The solutions of the hydrophone position offsets were in sensible ranges (**Table 5**). As this experiment was the first time with the icListen in the setup, its initial depth was set to the HEM hydrophone initial depth (4727.60 m). Consequently, the solution suggested a larger vertical offset for the icListen than the HEM. The a priori position variance were arbitrarily given to be 10, 10, and 5 m^2 in the x, y, and z direction respectively. The posteriori uncertainties went down to 10 % of the a priori uncertainties. The final mean depth of the HEM hydrophone was 4,735.17 $\pm$ 0.33 m and the final mean depth of the icListen was 4,734.85 $\pm$ 0.22 m. The icListen height is higher than the HEM by 0.33$\pm$ 0.55m. Assuming that the seabed where both hydrophones are situated is flat over approximately 46 m of their horizontal separation, one would expect to obtain the median height difference from the inversion close to the installation height difference of 1.8 m. Thus, the discrepancy of 1.1 m from the expected value makes the result of the hydrophone depths not so convincing. In terms of sound speed perturbation magnitudes, assuming a linear increase in the ocean temperature between October and November, at the time of experiment (26 – 30 October 2018), the ocean temperature inferred from the tomographic measurements should have been higher than what it was when the October CTD cast was taken (12th October 2018). The inverse sound speed perturbation field of the HEM, however, suggested an opposite trend, having a "colder" ocean. In the case of the icListen solution, it suggests that the ocean became partially "warmer" in the northwest sector. It is crucial to restate here that small scale variabilities or sub-mesoscale ocean features may play a role in regulating local variabilities to some level. To find out, more data need to be collected to verify this assumption.

10. Conclusions and Future Work

This study has improved the previous ocean tomography system and data processing, and revealed insights about the inverse model and properties of the ocean contained within the RAP volume. The acoustic transmission system was upgraded to allow for the higher transmitted sound level to increase the SNR. The GNSS positioning data was proved to be practical and adequately accurate for the RAP purpose. An analysis of acoustic receptions at the hydrophone end was conducted to assure functional acoustic receptions. A concern about timing reliability of the HEM and the icListen hydrophones was addressed in Chapter 5. Although the time offsets between these two hydrophones appeared to be integer seconds, a correction to acquire absolute timing without any time offsets is necessary from the perspective of the observatory's providing reliable time. An analysis of the non-physical range and ship dependences of the original travel time perturbation measurements implied the necessity of improvements to the ray tracing and data processing. The system delay at the transmission end was included (0.3 ms, significant compared to the ~1 ms signals), and that eliminated the apparent ship dependence from the travel time measurements. A review on ray tracing in the ellipsoidal coordinate system for short-range geodesy applications presented in Chapter 7 helped resolve the range dependence. Taking all these improvements together, we finally obtained reasonable travel time perturbation measurements and fed those into the inversion procedure. The travel time perturbation appeared to be more sensitive to the third empirical mode than expected. To reduce the ambiguity from the depth dependence of the empirical modes, depth-averaged sound speed perturbation was determined from the inverse solution which significantly improves the solution's accuracy. The travel time perturbation measurements contained small-scale variability which could not be resolved by the model correctly. Spatially averaging the reconstructed measurements (with the hydrophone offset portion of the travel time removed) and before inverting for the sound speed perturbations gave the results which agreed better with the a priori correlation length and eliminated energy leakage outside the sampled area. There was a discrepancy between the recovered sound speed perturbation fields of the HEM and the icListen. The colder ocean suggested by the HEM data contradicted an increasing trend of the ocean temperature inferred from the CTD casts collected in October and November 2018. The icListen had lower magnitudes of sound speed perturbations which appeared to be more physically sensible. For the

hydrophone positions, the depth difference of 0.33 m between the HEM and the icListen is still questionable considering the installation height difference of 1.8 m.

This study focused on the dataset collected in October 2018. The next immediate step is to perform the same analysis on the datasets from June 2017 and June 2018 and compare the results. The datasets could be treated together at the same time or separately. Assimilating all available data would help reduce the uncertainties of the hydrophone position solutions and provide a single best estimate of the hydrophone positions. Treating datasets individually would help to check consistency of the measurements taken at different times. Another possible improvement to the current data processing is to rework the vertical representation of the model. In this study, the EOF modes were used to represent the vertical sound speed perturbation structure, and the sound speed profile which was closest to the experiment date in time was used as a reference ocean state. Finding a more appropriate reference sound speed profile to be used in the EOF analysis and travel time calculation will allow for detecting changes in the ocean relative to a single reference state which will be more sensible for long-term monitoring. In addition, dynamical modes could be computed and used in the inversion procedure to compare with the results using the EOF modes.

For further steps, the results from the experiment indicated small-scale spatial fluctuations in the measurements which could be caused by biases in the ocean tomography system or sub-mesoscale variability. Analyzing the datasets from June 2017 and June 2018 will help clarify this question. If the small-scale fluctuations in the measurements are contributed by the ocean variability, improving the inverse model to be more capable of handling small scale variabilities will yield more reliable solutions. One possible way is to reduce representation errors by using the most suitable correlation length for the local ocean horizontal structure. Field measurements could be used to estimate the correlation length empirically. The experiment could be taken by having a ship traversing along a radial transect and measuring travel time perturbations of the points along the line (or the existing data can be used as well). Then, using the measurements to calculate spatial covariance among the data points and determine the correlation length. Alternatively, the experiment ship course could be designed to cover the entire area of interest to obtain an azimuthally-averaged correlation length. Ultimately, independent measurements such as XBTs are required to verify the tomographic results. The XBT readings could be taken along the same radial line when doing the correlation length measurement. The XBT data can be used

to obtain the best sound speed profile and we could assimilate the XBT data into the ocean model framework by projecting the sound speed deviation relative to the reference state onto the empirical modes and use the amplitudes of these modes to represent sound speed variability. Eventually, after solving the issue regarding discrepancies between the HEM and the icListen, combining HEM and icListen data points into a single dataset and using that in the inversion would benefit the accuracy of the inverse solutions.

The project has demonstrated the practicality and utility of the RAP tomography at the ACO and by extension general applicability for other ocean observatories. More data still needs to be collected to improve the tomography system and the understanding of the local ocean. The findings in this study suggest future opportunities to extend the RAP tomography to study sub-mesoscale ocean variability. Besides, the coverage of the area of interest, the level of solution's accuracy and promising insights in local sound speed fluctuations would be applicable for improving seafloor geodesy; this can be a source of further cooperation and exchange of expertise in the future.

Appendix A. Signal Parameters

The linear-frequency modulated signal is given by

$$x(t) = A\ sin\ (\omega(t) \cdot t + \emptyset) \tag{51}$$

in which A is the amplitude and $\omega(t)$ is angular frequency which is linearly-increasing with time, and $\emptyset$ is the initial phase. $\omega(t)$ can be expressed in this formula

$$\omega(t) = 2\pi \left(f_c + BW \frac{(t - T/2)}{T} \right) \tag{52}$$

where f_c is the center frequency, BW is the bandwidth, and T is the signal duration.

Parameters for the LFM signal used in this study are:

Source Level	199.5 dB
Center Frequency (f_c)	4134.375 Hz
Bandwidth (BW)	1378.125 Hz
RMS Bandwidth	795.661 Hz
Signal Duration	22.5 ms

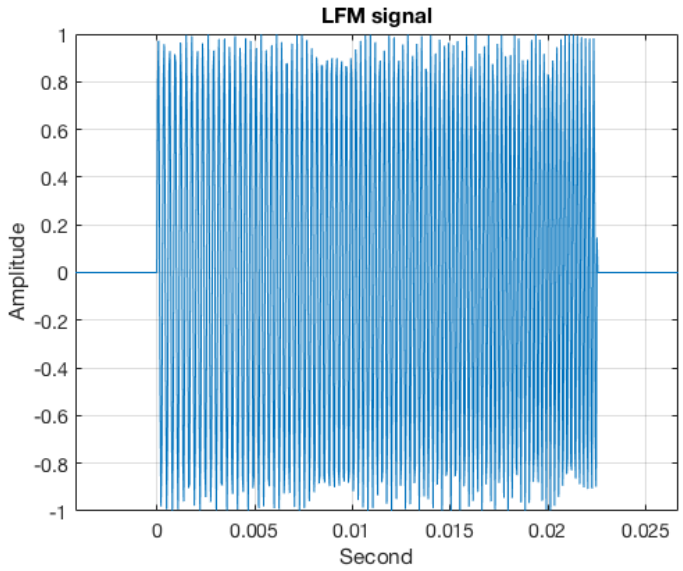

Figure 67. Computer-generated LFM signal

Appendix B. Acoustic Calculation

This section will present the calculation process of the expected Signal-to-Noise Ratio of the acoustic reception.

To ensure sufficient accuracy of travel time measurements in the experiment, predicting the Signal-to-Noise Ratio is necessary for designing the acoustic transmission system to answer to the desired accuracy level. The SNR is defined by

$$SNR = \frac{x}{median(\mathrm{x})} \tag{53}$$

in which x is a signal

In this case, the time-series x is a cross-correlation function between an audio signal and a signal replica. We use a pulse compression technique to increase the SNR by using a frequency modulated signal as the transmitted signal. Complex demodulation technique is used to extract the complex envelope of the cross-correlation function whose peaks determine the times of acoustic arrivals. For LFM signals, the peak width of the complex envelope is approximately determine by a reciprocal of the bandwidth of the LFM signal (Munk, Worcester & Wunsch, 1982). Consequently, the RMS travel time error (σ_t) associated with an acoustic reception with a specific SNR level is defined as

$$\sigma_t = \left(\Delta\omega_{rms}\sqrt{SNR}\right)^{-1} \tag{54}$$

where $\Delta\omega_{rms}$ is the RMS bandwidth of the frequency-modulated signal (Munk, Worcester & Wunsch, 1982). $\Delta\omega_{rms}$ is given by

$$(\Delta\omega_{rms})^2 = \frac{\int \omega^2 |P(\omega)|^2 d\omega - \int \omega |P(\omega)|^2 d\omega}{\int |P(\omega)|^2 d\omega} \tag{55}$$

where $P(\omega)$ is the frequency spectrum of the transmitted signal (Fourier-transform pair), which can be treated as a constant (given a relatively flat Transmitting Voltage Response **Appendix E**). By limiting the integral range to the range of the signal's bandwidth, **Equation 55** becomes (Munk, Worcester and Wunsch, 1982).

$$(\Delta\omega_{rms})^2 = \frac{\int_{f_o-BW/2}^{f_o+BW/2} \omega^2|P(\omega)|^2 d\omega - \int_{f_o-BW/2}^{f_o+BW/2} \omega|P(\omega)|^2 d\omega}{\int_{f_o-BW/2}^{f_o+BW/2} |P(\omega)|^2 d\omega} = \frac{BW^2}{3} \quad \textbf{(56)}$$

Since the signal has the bandwidth of 1378.125 Hz, the RMS signal is calculated to be 795.661 Hz. If the desired accuracy of the travel time is 0.25 ms, the required SNR will be 25. In other words, the range of the SNR between 10 and 25 will result in the RMS travel time error range between 0.4 and 0.25 msec.

From the specification of the RMS travel time error, the sonar equation of the acoustic reception is used to design the acoustic transmission system to achieve the desired SNR level. The equation is given by

$$\text{SNR} = \text{SL-TL-NL+PG} \quad \textbf{(57)}$$

where SL is the source level, TL is the transmission loss, NL is the total noise level, and PG is the processing gain obtained from pulse compression.

The transmission loss is comprised of spreading loss and attenuation. For a slant range of 30 km, the transmission loss is approximated to be 94 dB.

The noise level is given by

$$\text{NL} = \text{NL}_{ambient} + 10\log(\text{BW}) \quad \textbf{(58)}$$

The $\text{NL}_{ambient}$ is an average ambient noise level. Here, we choose a conventional averaged number of the ambient noise level in a frequency range between 3000 to 6000 Hz, which is equal to 60 dB (Urick, 1983). This number is multiplied by the bandwidth of interest 1378.125 Hz. The total noise level is calculated to be 91.4 dB.

The processing gain is an additional gain obtained from the pulse compression. It is given by

$$\text{PG} = 10\log(BW \times T) \quad \textbf{(59)}$$

where T is the signal duration

The LFM signal duration is chosen to compromise between the processing gain and the effect of Doppler shift caused by vessel movement (maximum at 12 knots). The processing gain of the LFM signal with the signal duration of 22.5 msec is calculated to be 14.9 dB.

The source level can be expressed as

$$SL = 170.8 + 10\log(P) + DI \quad \textbf{(60)}$$

where P is the resultant acoustic power converted from the electrical power received by the transducer, and DI is the directivity index from Massa Sonic 2016 specification (**Appendix E**). On the October 2018 cruise, the acoustic power output was designed to reach 376 W. That results in and estimated source level of 199.5 dB. With all terms calculated, the expected SNR is calculated to be 29.0 dB. Therefore, by using the source level of 199.5 dB, we will obtain the travel time accuracy down to 0.23 ms, which is sufficient for this purpose. See **Table 6** for the summary.

Source Level	199.5 dB re 1μPa at 1m
Spreading Loss	89.5 dB
Attenuation	4.5 dB
Ambient Noise Level	60.0 dB re 1 μPa/$\sqrt{\text{Hz}}$
Total Noise Level	91.4 dB
Processing Gain	14.9 dB
SNR	29.0 dB

Table 6. Summary of the expected SNR for the LFM signal at a range of 30 km

Appendix C. Ray Tracing

This section presents the ray tracing model used by Varamo (2017) and a constant sound speed gradient introduced in **Chapter 7** to compare to the previous model. Both models were implemented in a planar coordinate system. For the first model, rays traveling through constant sound speed layers in a planar coordinate system can be traced as follows

A ray parameter is defined as

$$a = \frac{\sin(\theta_1)}{c_1} = \frac{\sin(\theta_2)}{c_2} \tag{61}$$

where θ_1 is an incident angle of the ray at the interface between layer 1 and layer 2 in the layer 1, and c_1 is a sound speed in layer 1. This equation is called Snell's law in in the rectangular coordinate system. The incident angle of each layer *n* can be traced by

$$\sin(\theta_n) = a\, c_n \tag{61}$$

Since the sound speed in each layer is constant, the ray path in each layer is a straight line. Basic trigonometry is used to derive relationships of horizontal range, ray arc length and vertical distance traveled by the ray in each layer. Given that a horizontal range and the depth between the source and the receiver are known, the total horizontal range, total and total travel time can be calculated by

$$r_{tot} = \sum_{n=1}^{N} (z_{n+1} - z_n) \tan(\theta_n) \tag{62}$$

$$t_{tot} = \sum_{n=1}^{N} \frac{(z_{n+1} - z_n)}{c_n \cos(\theta_n)} \tag{63}$$

where *r* is horizontal range, and *t* is travel time, n is the number of layers where the source layer is 1 and the receiver layer is N.

For rays traveling through ocean layers with constant sound speed gradients in a planar coordinate system, the ray in each layer travels along a circular arc. The closed-form solutions of the total ray arc length, the total horizontal range, and the total travel time are given by

$$s_{tot} = \sum_{n=1}^{N} \frac{(\theta_{n+1} - \theta_n)}{|ab_n|} \tag{64}$$

$$r_{tot} = \sum_{n=1}^{N} \frac{\sqrt{1 - a^2 c_n^2} - \sqrt{1 - a^2 c_{n+1}^2}}{ab_n} \tag{65}$$

$$t = \sum_{n=1}^{N} \frac{\log\left(\frac{c_{n+1}}{c_n}\right) - \log\left(\frac{\sqrt{1 - a^2 c_{n+1}^2}}{\sqrt{1 - a^2 c_n^2}}\right)}{b_n} \tag{66}$$

where $b_n = \frac{c_{n+1} - c_n}{z_{n+1} - z_n}$

For the integral forms of these equations, refer to Medwin (2005).

A sound speed profile was obtained by using CTD data which reported pressure, salinity, and depth. The sound speed was calculated based on the Thermodynamic Equation Of State -2010 (TEOS-10) for seawater (McDougall & Barker, 2011). Before doing ray tracing, to take the effect of Earth's curvature into account, the Earth flattening transformation must be applied to the equations above to project end points in the spherical Earth coordinate system onto the Cartesian coordinate system (For ray tracing in the spherical coordinate system, see Chadwell et al, 2010). The equation is given by Dushaw and Colosi (1998)

$$\varepsilon = \frac{z}{R_e} \tag{67}$$

$$z_{fl} = z\left(1 + \frac{\varepsilon}{2} + \frac{\varepsilon^2}{3}\right) \tag{68}$$

$$c_{fl} = c(1 + \varepsilon + \varepsilon^2) \tag{69}$$

Then, the ray tracing can be done and yields a good result relative to working out ray tracing in the spherical coordinate system. To find an eigen ray connecting between the source and the receiver, iterative calculations were required to find a launch angle which yielded the horizontal and vertical distances which were close to the pre-determined horizontal and vertical ranges between the source and the receiver (from the position data). The convergence criterion was1 mm.

Comparisons between the total travel times and the ray arc lengths of the two approaches were made (**Figure 34**). The differences were small compared with other sources of errors. Thus, in this study, a constant sound speed layer model was used for ray tracing due to its simplicity.

Appendix D. GNSS systems comparison analysis

Here, a detailed comparison result will be presented to assure the readers that the POS MV binary output provides us with the position data of the transducer with sufficient accuracy for our study.

Three ship position datasets, the Trimble RTX (RTX), the POS MV GGA NMEA Sentence (POS MV GGA), and the POS MV Binary output are the subjects of the analysis. To make one-to-one comparison, the transducer and the granite block position data from the POS MV binary file have to be transformed to represent the primary antenna as the RTX and the POS MV GGA. After that, the four antenna position datasets in the UTM coordinate frame have to be transformed into the locally-level ship frame for easier interpretation. **Figure 68** provides an overview of the data flow chart for coordinate transformations.

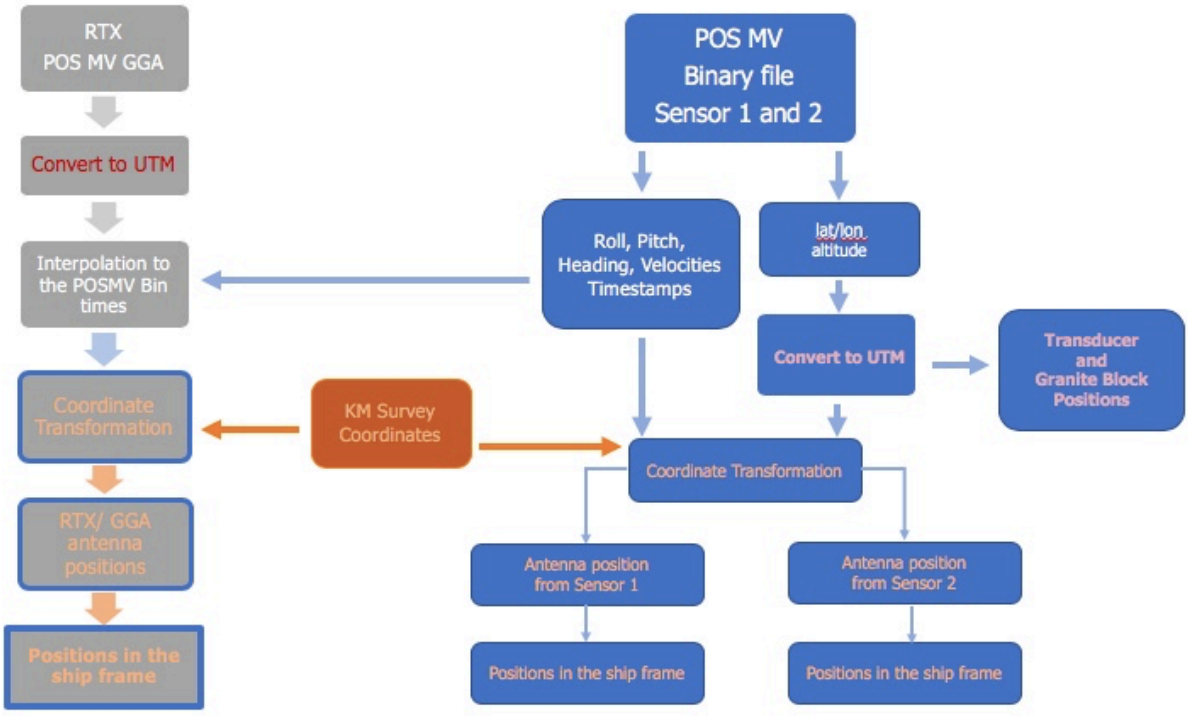

Figure 68. Data flow chart for transforming the four datasets to represent the primary antenna in the locally-level ship frame.

Component	X (m)	Y (m)	Z (m)	Distance (m)
Granite Block	0	0	0	0
Primary Antenna	6.44	6.51	-27.76	29.231
Transducer No.5	0.568	19.60	0.715	19.621

Table 7. Surveyed coordinates of the shipboard devices

To transform the transducer and granite block geographic positions from the POS MV binary file to represent the primary antenna, we need the lever arms of the primary antenna and the transducer, and the ship attitude. The transformation works in the Cartesian coordinate systems. The first step is to convert the geographic position. The ship attitude reported by the POS MV binary follows the Tate-Bryant sequence of rotation which starts with a rotation of the heading about the z-axis, then a rotation of the pitch angle around the y-axis, and finally a rotation of the roll angle about the x-axis (Applanix. 2016. POS MV V5 User Interface and Control Document). The transformation equation is

$$\vec{A}_{UTM} = \vec{T}_{UTM} + R_{UTM}^{sff}(R_{ssf}^{llf}(\vec{r}_{ant} - \vec{r}_{td})) \quad \textbf{(70)}$$

Where $\vec{A}_{UTM}$ is the resultant antenna position vector in the UTM coordinates, $\vec{T}_{UTM}$ is the transducer position vector in the UTM coordinates, $\vec{r}_{ant}$ and $\vec{r}_{td}$ are the lever arm vectors of the antenna and the transducer with respect to the granite block, R_{UTM}^{sff} and R_{ssf}^{llf} are rotation matrices. R_{UTM}^{sff} is a rotation matrix which rotates the UTM coordinate frame to align with the ship fixed frame (the original unrotated ship frame with its x-axis aligns with the north) which is defined by

$$R_{UTM}^{sff} = \begin{bmatrix} 0 & 1 & 0 \\ 1 & 0 & 0 \\ 0 & 0 & -1 \end{bmatrix} \quad \textbf{(71)}$$

R_{ssf}^{llf} is a rotation matrix which rotates the ship fixed frame to the locally level ship frame using the Tate-Bryant sequence of rotation. This matrix is constructed using ship heading, roll angle, and pitch angle respectively.

$$R_{UTM}^{sff} = R_\gamma R_\beta R_\alpha \tag{72}$$

where

$$R_\gamma = \begin{bmatrix} \cos(\gamma) & -\sin(\gamma) & 0 \\ sin(\gamma) & \cos(\gamma) & 0 \\ 0 & 0 & 1 \end{bmatrix}$$

$$R_\beta = \begin{bmatrix} \cos(\gamma) & 0 & \sin(\beta) \\ 0 & 1 & 0 \\ -\sin(\beta) & 0 & \cos(\beta) \end{bmatrix}$$

$$R_\alpha = \begin{bmatrix} 0 & 0 & 1 \\ 0 & \cos(\alpha) & -\sin(\alpha) \\ 0 & \sin(\alpha) & \cos(\alpha) \end{bmatrix}$$

where α is roll angle, β is pitch angle, and γ is heading

In this comparison, it is more convenient and intuitive to interpret the primary antenna positions in the locally-level ship frame rather than the global ellipsoidal coordinate system. To transform the primary antenna geographic positions to the ship coordinates, first the antenna geographic positions need to be converted to the UTM coordinates. The easting and northing of the UTM coordinates will be the x and y coordinates respectively. The z coordinate can be derived from the altitude data reported by the positioning system (ellipsoidal height). The equation to map the antenna position from the UTM coordinates to the ship locally-level ship frame is

$$\vec{r}_{ant} = \vec{r}_{td} + \left(R_{sff}^{llf}\right)^{-1}\left(R_{UTM}^{sff}\right)^{-1}((\vec{A}_{UTM} - \vec{T}_{UTM})) \tag{73}$$

where $\left(R_{sff}^{llf}\right)^{-1}$ and $\left(R_{UTM}^{sff}\right)^{-1}$ are inverse matrices of R_{sff}^{llf} and R_{UTM}^{sff}, which in this case are just transposes of the original matrices (Mark W. and M. Vidyasagar 1989).

There were three test cases, before-cruise, at-sea, and after-cruise. In the at-dock cases, the tidal signal was used to primarily verify the functionality of the GNSS data. **Figure 69** shows the

recorded tidal signal from PACCIOS. Ignoring outliers of the RTX data, the vertical displacement of three GNSS datasets agree well with the recorded tidal signal.

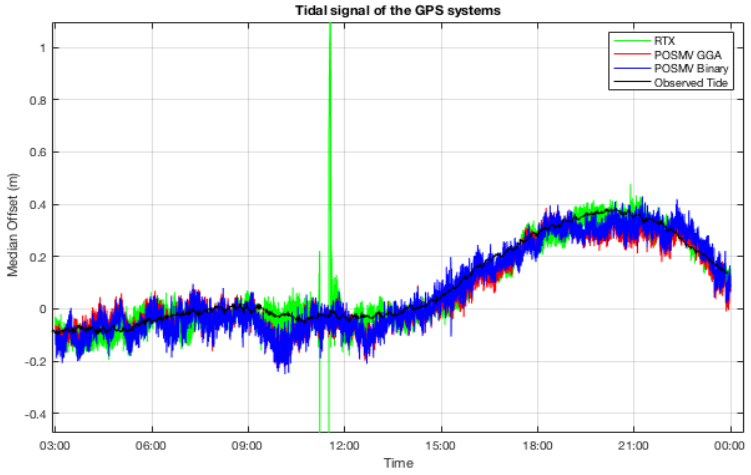

Figure 69. Comparison between the recorded tidal signal from PACCIOS (black), the RTX position (light green), the POS MV GGA position (red), and the POS MV binary's transducer position. All time-series are plotted their offsets from their corresponding medians.

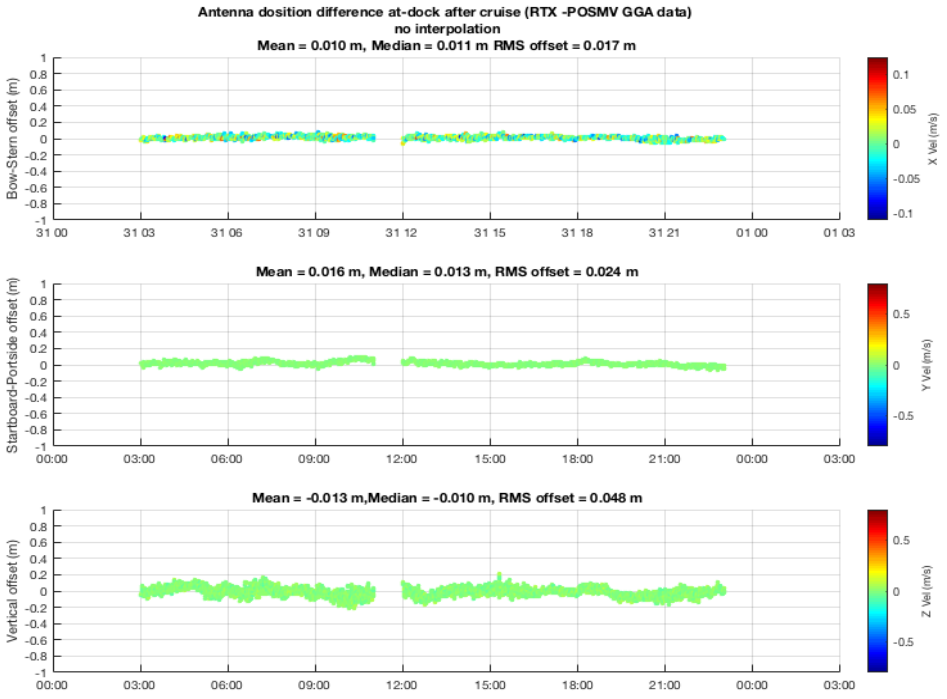

Figure 70. The position differences between the RTX and the POS MV GGA antenna position data collected after the cruise when the ship was at-dock.

For the at-dock data, comparison between the RTX and the POS MV GGA antenna positions is shown in **Figure 70** . The medians of position differences in three axes are smaller than 1.6 cm with the largest RMS error of 4.8 cm in the vertical. This reveals strong agreement of these two datasets.

Comparisons between the RTX data and the antenna positions data calculated from the POS MV binary's granite block and the transducer position data have high level of agreement accurate to the decimeter level. The largest discrepency comes from the antenna position based on the transducer position. The antenna of ther transducer position data is 11.8 cm closer to the bow than the RTX antenna (**Figure 71**). The bow-stern offset of the decimeter level is present in a comparison betwwen the POSMV GGA antenna position and the antenna position from the POS MV binary transducer position as well (12.8 m toward the bow).

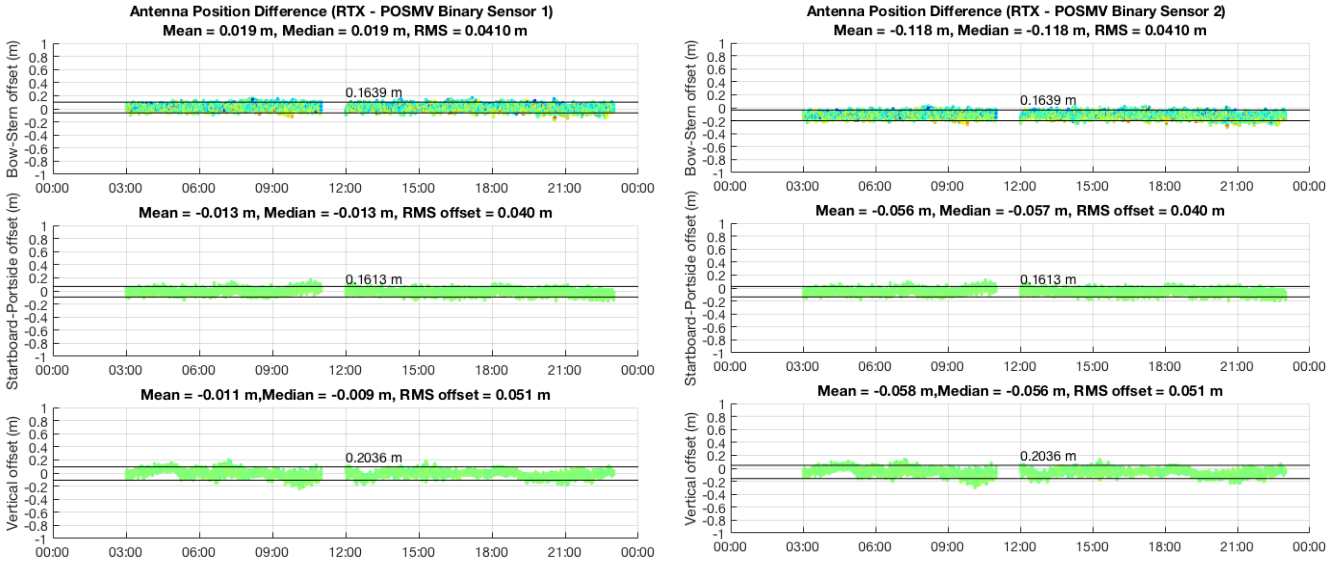

Figure 71. The position differences between the RTX antenna position and the POS MV binary. Left, sensor 1 granite block, Right, sensor 2 transducer antenna.

For the at-sea data, the same fashion of comparisons was conducted. **Figure 23** comparison between the RTX and the POS MV GGA antenna positions. Their horizontal positions agree well down to a centimerter level with 2-4 cm of RMS errors. The vertical RMS error of 7 cm is larger than the horizontal RMS erros but still smaller than 10 cm. The result confirms the high agreement between the RTX and the POS MV GGA when the ship was under motions.

Comparisons between the RTX and the POS MV binary transducer positions, and between the POS MV GGA and the POS MV binary transducer positions are shown in **Figure 24** and **72,** and. Like the at-dock test, the decimeter-level bow-stern position offsets of the transducer position data reappear in these comparisons. The median of bow-stern position difference is 16.2 cm when compared with the RTX and becomes 9.2 cm when compared with the POS MV GGA. When comparing the RTX and the POS MV binary transducer positions, ones can see larger bands of variations than the comparison between the POS MV GGA and the POS MV binary transducer positions. This can be explained by the elimination of inherent signal processing artifacts of the POS MV when differencing two POS MV datasets. Those artifacts amount to discrepancies when differencing a POS MV dataset with another non-POS MV dataset. The medians of y-axis and z-axis position differences are within 10 cm with associated RMS errors smaller than 10 cm.

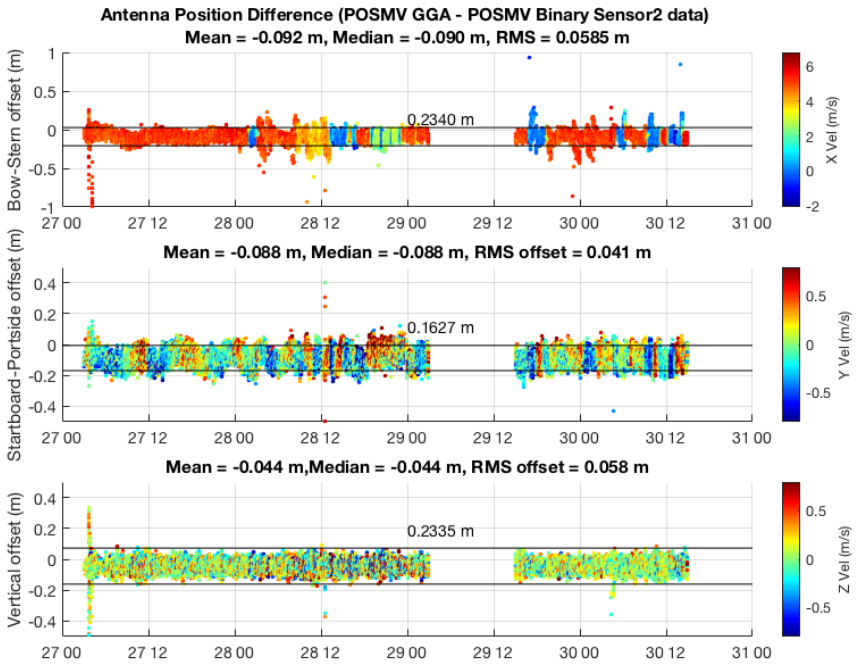

Figure 72. The position differences between the POS MV GGA and the antenna position based on the POS MV binary's transducer position.

Lastly, a comparison between the granite block's coordinates and the transducer coordinates is shown in **Figure 73**. The transducer position relative to the granite block is off by 13 cm in the

bow-stern direction, 4.2 cm in the starboard-portside direction, and 5.2 cm in the vertical direction.

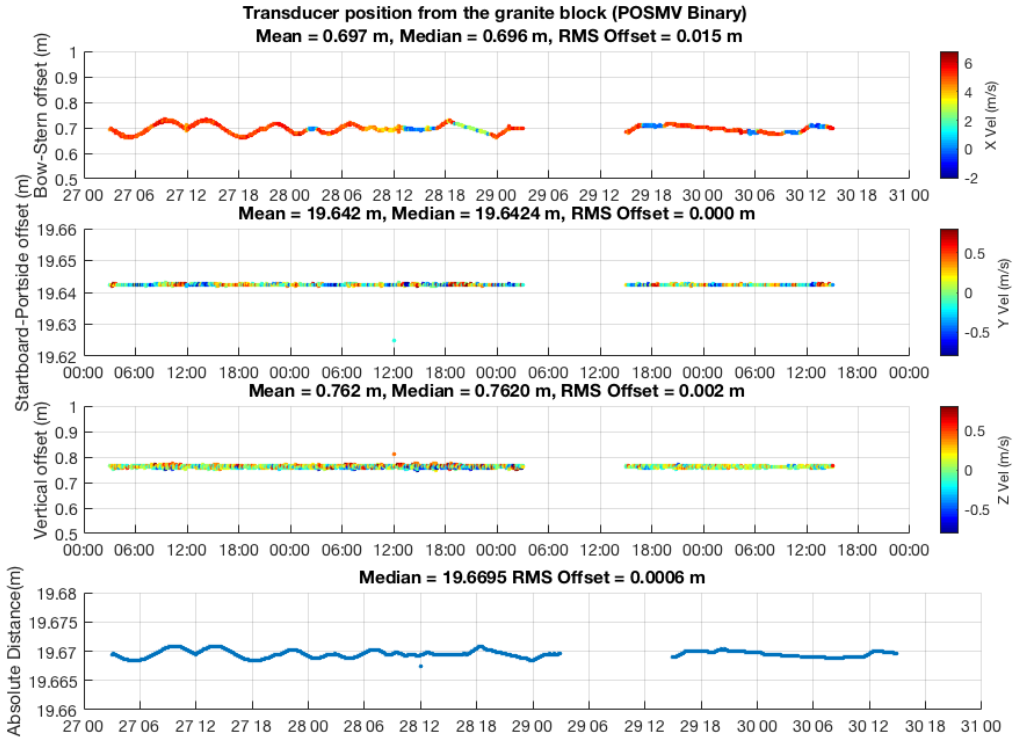

Figure 73. The transducer position relative to the granite block recorded when the ship was at-sea in the locally-level ship frame. The x position seems to vary most while the other two positions are fairly constant throughout the cruise. The absolute distance between the transducer and the granite block varies less than 5 mm.

This analysis reassures that the POS MV binary output is adequately accurate and reliable. The position differences found between the position datasets are small when converted into equivalent travel time errors (less than 0.2 ms at 30 km). This conclusion is based on the fact that the Trimble RTX and the POS MV GGA data are unaffected by the POS MV internal processing and sufficiently accuracy.

Appendix E. Massa TR-1075a Specifications

Circular piston radiating source with 1/2 wavelength diameter at 4 kHz and 80˚ conical beam angle. Terminated with C1F2 underwater connector and mates to C1M2 underwater connector (Massa Sonic, 2016).

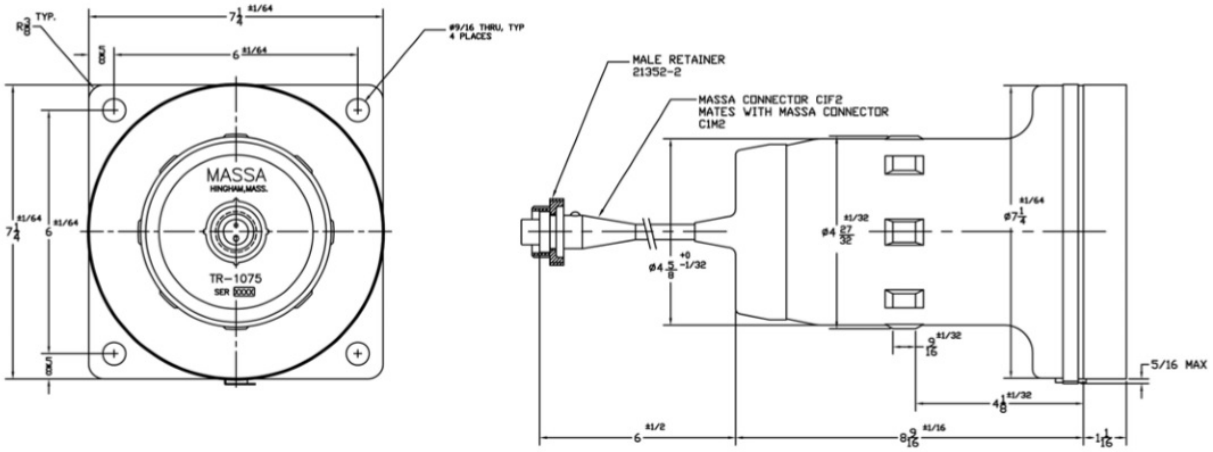

Frequency range: 2.5 - 10 kHz

Duty cycles: 600 W at 30% OR 200 W at 100%

Frequency tuned for 0˚ phase (nominal): 4 kHz

Impedance Magnitude (nominal): 100 Ω at 4 kHz

Tuning circuit: Parallel

Weight: 25 lbs

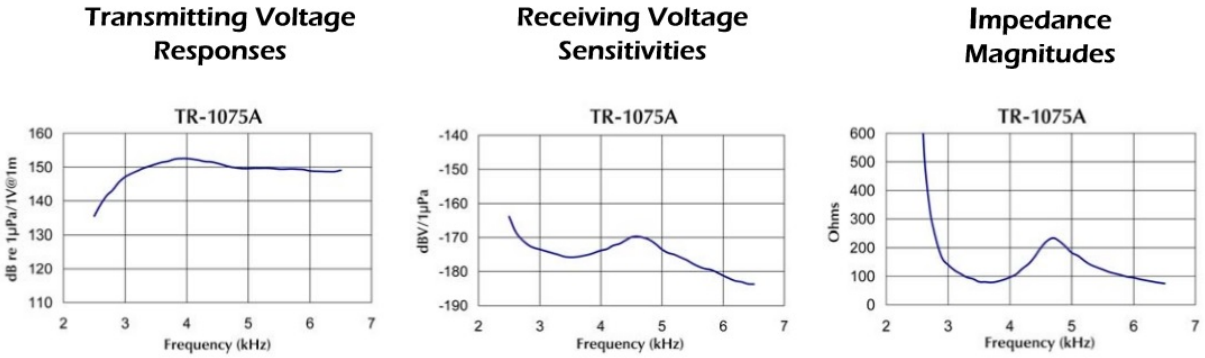

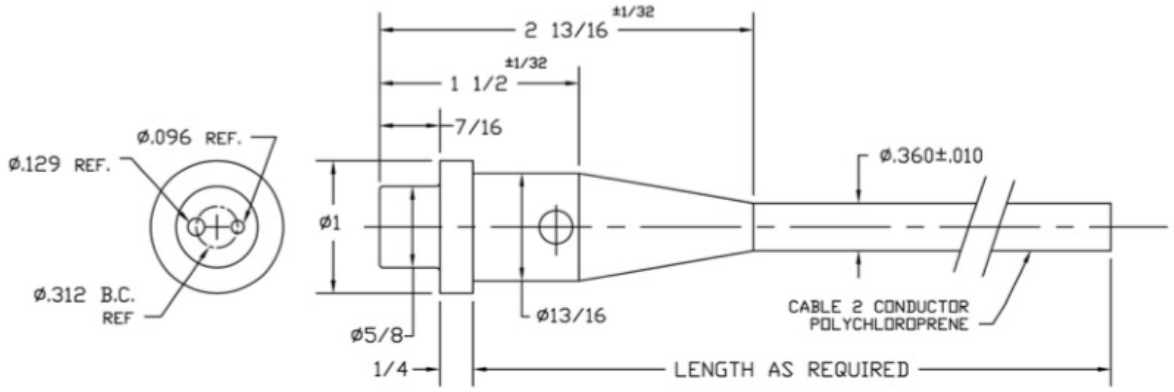

Outline Drawing of a C1M2 Male Connector for Mating to Massa Underwater Transducers

(without retaining ring)

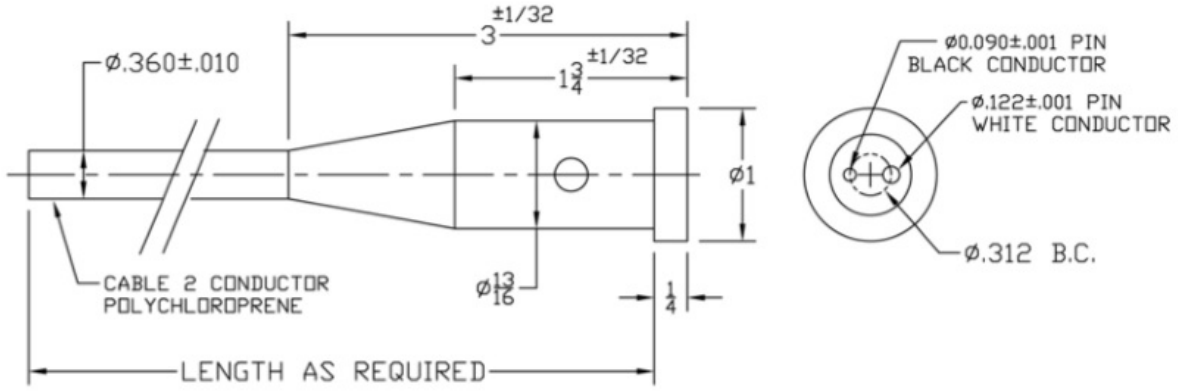

Outline Drawing of a C1F2 Female Connector Supplied on Massa Underwater Transducers

(without retaining ring)

Appendix F. Scarlett 6i6 Second Generation Specifications

The Scarlett 6i6 (second generation) is an audio interface device manufactured by Focusrite, Inc., England, 2016. It is designed for recording signals from multiple sources. It is easy to control using a computer via a USB connector. The table below presents the device's specifications.

Supported Sample Rates	44.1 kHz, 48 kHz, 88.2 kHz, 96 kHz, 176.4 kHz
Frequency Response	20 Hz – 20 kHz
Dynamic Range (Input)	110 dB
Maximum Level (Input)	+16 dBu (Input2 1-2). +22 dBu (Inputs 3-4)
Impedance (Input)	52kΩ
Dynamic Range (Output)	108 dB
Maximum Level (Output)	+16 dB
Impedance (Output)	94Ω

Appendix G. V/I Measurement Unit Specifications

A Schematic diagram for the interface module that allows for voltage and current measurements along the cable is shown below. The interface module outputs the voltage at a 1:100 ratio (100 V in - 1 V out) and the current is output at a 1:1 ratio (1 A in - 1 V out).

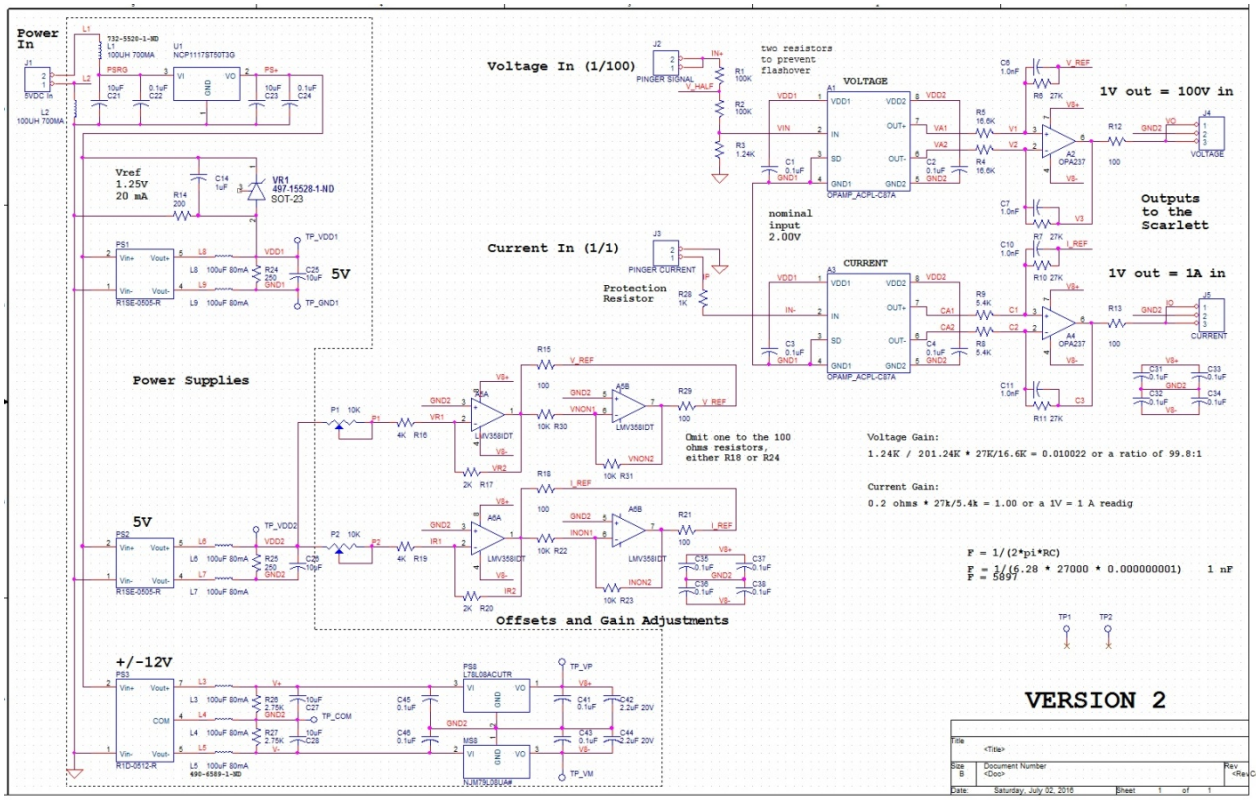

Appendix H. Proel HPX2800 Specifications

Proel HPX2800 is an audio amplifier manufactured by Proel, Inc., Italy, 2017. The device's specifications are presented below.

Power 8 ohm	600 W
Power 4 ohm	1000 W
Power 2 ohm	1400 W
Power BRIDGE 8 ohm	2000 W
Power BRIDGE 4 ohm	2800 W
Frequency Response	20 Hz – 20 kHz
Input Sensitivity (nominal)	0 dBu / 0.775 Vrms
Input Sensitivity (fixed gain)	+ 7.0 dBu / 1.73 Vrms
Gain	39 dB
Dimension (W x H x D)	19" x 3.5" x 15.6"
Weight	9.2 kg

References

Applanix Corporation. (2016). POS MV V5 Installation and Operation Guide.

Applanix Corporation. (2016). POS MV V5 User Interface and Control Document.

Burgmann, R. & D. Chadwell. (2014). Seafloor Geodesy. *Annual Review of Earth and Planetary Sciences.* 42. 509-534.

Chadwell, C. D., & Sweeny, A. D. (2010). Acoustic Ray-trace Equations for Seafloor Geodesy, *Marine Geodesy*. 33.164-185.

Chiswell, S. M. (1994). Using an Army of Inverted Echo Sounders to Measure Dynamic Height and Geostrophic Current in the North Pacific Subtropical Gyre. *Journal of Atmospheric and Oceanic Technology*, 11,1420–1424.

Cornuelle, B. (1985). Simulations of Acoustic Tomography Array Performance With Untracked or Drifting Sources and Receivers. *Journal of Geophysical Research*, 90**,** 9079-9088.

Cornuelle, B. & Howe, B. (1987). High Spatial Resolution in Vertical Slice Ocean Acoustic Tomography. *Journal of Geophysical Research*, 92. 11680-11692.

Dushaw, B. & Colosi, J. (1998). Ray Tracing for Ocean Acoustic Tomography. Technical Memorandum, Seattle: Applied Physics Laboratory - University of Washington.

Dushaw, B. Worcester, P. Munk, W. Spindel, R. Mercer, J. Howe, B. Metzger Jr, K. Birdsal, T, Andrew, R. Dzieciuch, M. Cornuelle, B. Menemelis, D. (2009). A decade of of acoustic thermometry in the North Pacific Ocean. *Journal of Geophysical Reseach*. 114 (C7).

Massa Sonic. (2016). "Massa TR-1075 Sub-Bottom Profiling Transducer." Hingham, MA: Massa Production Corporation.

Matthews, D. Powell, B. & Milliff, R. (2011). Dominant spatial variability scales from observations. *Deep-Sea Research I,* 58. 979-987.

McDougall, T.J., & Barker, P.M. (2011). Getting started with TEOS-10 and the Gibbs Seawater (GSW) Oceanographic Toolbox. SCOR/IAPSO WG127.

Medwin, H. (2005). *Sounds in the Sea: from ocean acoustics to acoustical oceanography* (pp. 7-84), New York: Cambridge University Press.

Medwin, H. & Spindel, R. (2005). *Sounds in the sea: from ocean acoustics to acoustical oceanography* (pp. 461-480), New York: Cambridge University Press.

Munk, W. & Wunsch, C. (1979). Ocean Acoustic Tomography: A scheme for large scale monitoring. *Deep-Sea Research,* 26, 123-161.

Munk, W. Worcester, P. & Wunsch, C. (1995). *Ocean Acoustic Tomography*. New York: Cambridge University Press.

Proel. *HPX2800*. 2017. http://www.proel.com/index.php?route=product/product&product_id=5936.

Rihaczek, A. (1985). *Principles of High-Resolution Radar*. Los Altos. Peninsula Publishing.

Spong, M. W. & Vidyasagar, M. (1989). *Robot Dynamics and Control* (pp. 32-41): John Wiley & Sons.

Tarantola, A. (1987). *Inverse Problem Theory*. New York: Elsevier Science Publishing Company.

Uffelen, V. L. Howe, B. Nosal, E. & Carter, G. (2015). Localization and Subsurface Positioning Error Estimation of Gliders Using Broadbrand Acoustic Signals at Long Range. *IEEE Journal of Oceanic Engineering*. 41(3). 501-508.

Urick, J. (1983). *Principle of Underwater Sound*. Los Altos. Peninsula Publishing.

Varamo, V. (2017). *Reliable Acoustic Path at the ALOHA Cabled Observatory.* Master's thesis. University of Hawai'i at Mānoa, Honolulu, HI, USA.

Wunsch, C. (2006). *Discrete Inverse and State Estimation Problems* (pp.132). New York: Cambridge University Press.